UNIVERSITÀ DEGLI STUDI DI MILANO

Doctorate School of Chemical Sciences and Technologies
Department of Physical Chemistry and Electrochemistry
Doctorate Course in Industrial Chemistry, XXIII Cycle

Ph.D. Thesis

PREPARATION AND PERFORMANCE EVALUATION OF MATERIALS FOR ELECTROCATALYTIC APPLICATIONS

CHIM/02

ALESSANDRA COLOMBO

Supervisor: Prof. Sergio Trasatti
Co-supervisor: Dott.Edoardo Guerrini

Co-ordinator: Prof. Dominique Roberto

A.A. 2009/2010

TABLE OF CONTENTS

ABSTRACT

One of the main issues of hydrogen economy is the electrolytic production of H_2 from aqueous solutions and its utilization in fuel cells to generate energy. In this scheme, hydrogen acts as an energy carrier. This scenario is gaining increasing attention together with other energy-generating technologies, such as solar and nuclear technologies. Electrolysis is in principle a clean technology, but it requires a great consumption of electrical energy.

The present thesis concerns selection, production and optimization of electrocatalytic materials to improve the efficiency of hydrogen electrolytic production, by reducing operational costs.

From a catalytical point of view, H_2 evolution is a facile reaction. It is possible to further reduce energy losses by maximizing the surface area of electrodes or by activating cathodes. In the mean time, scrutiny of efficient electrode materials for O_2 anodic evolution is needed. In fact, the reaction of O_2 evolution is more energy demanding and affects the global energy balance severely. Therefore, development and optimization of the technology of electrolytic hydrogen production implies the evaluation of both cathodic and anodic reactions.

During the three years of my Ph.D., materials for both H_2 and O_2 evolution were prepared and characterized.

Materials for hydrogen evolution

As a matter of fact, the behavior of electrocatalysts depends on the nature of the electrode material as well as on the surface morphology, the latter being determined by the method of preparation. As a consequence, the method of preparation affects the behaviour of the catalyst. Several mixed oxides of transition metals were thus synthesized. Both classical thermal decomposition method and innovative synthetic strategies were applied. All the materials produced were characterized with electrochemical techniques (cyclic voltammetry and cathodic polarization). Selected samples were investigated with non electrochemical techniques (scanning electron microscopy, powder diffraction) to check morphology and composition.

Ir-Co mixed oxides. Iridium and Cobalt mixed oxides were synthesized by thermal decomposition of suitable precursors and tested for cathodic hydrogen evolution from alkaline solutions. SEM analysis of the samples shows that the introduction of IrO_2 produces

increasing roughness and porosity. Electrochemical experiments highlighted that electrodes with more than 5% of Ir content behaves as pure IrO_2. Both electrochemical and non electrochemical data suggest that the surface morphology of these electrodes is dominated by IrO_2. Thus a phenomenon of surface segregation can be inferred.

Ru-Ni mixed oxides (thermal decomposition). RuO_2 is among the most active materials for cathodic hydrogen evolution from acidic solutions. Its electrocatalytic activity can be further enhanced by modifying number and kind of surface active sites. Reducing the size of crystallites, doping and chemical mixing of RuO_2 with other elements are suitable strategies to maximize surface area while changing the nature of surface active sites.

Mixed oxides of Ruthenium and Nickel were synthesized in various compositions. Electrodes were prepared by direct thermal decomposition of suitable precursors on Titanium and Nickel platelets. The activity towards hydrogen evolution was checked by cathodic polarization. Electrodes need a pre-activation treatment, after which hydrogen evolution mechanism results modified. This is likely due to the dissolution of NiO_x, with new active sites exposed to the electrolytic solution.

Ru-Ni mixed oxides (Sol-gel synthesis). Reducing the size of crystallites – ideally up to single nanoparticles – is a way to greatly enhance surface area of electrode materials. RuO_2-based materials were thus synthesized by a new sol-gel route in non aqueous media. NiO_x was introduced to distort the RuO_2 crystal structure.

Catalyst powders (with various NiO_x content) were synthesized by a co-precipitation method, followed by annealing and milling, deposited on Titanium platelets and then tested for hydrogen evolution in acidic solutions. Morphology and composition were monitored by SEM and XRD. Although Nickel stability in acidic solution cannot be assessed, evidences for RuO_2 modifications are clearly seen.

Materials for oxygen evolution

As hydrogen evolution, oxygen production preferentially occurs at surface active sites. Therefore modification of the number and the nature of the active sites would enhance also electrocatalytic activity for anodic reactions. Besides reducing the size of crystallites, the formation of new active sites can be promoted by treatments, such as ion implantation and atom bombardment, which deeply modify the surface.

In the present thesis, such strategy was applied to RuO_2 prepared by thermal decomposition on Ti. Modification of the surface induced by these physical treatments can be exemplified as follows: i) laser intensely heats the surface, causing local fusion or crack

formation; ii) Kr bombardment mechanically damages the surface, simulating the formation of very small particles.

Eventual modifications induced by the surface treatments were investigated by cyclic voltammetry. The electrocatalytic activity towards anodic O_2 evolution was determined by anodic polarization. Experimental data have shown an increase in surface area for both treatments and a corresponding enhancement in O_2 production. The electrocatalytic activity resulted much higher for Kr bombarded samples. True electrocatalytic effects seem to prevail over geometric effects.

Synthesis of nanoparticles by non-aqueous microwave assisted method

Non-aqueous synthetic routes are a promising approach to produce metal oxide nanoparticles. The initial reaction mixture just consists of an organic solvent and the metal precursor. The reaction temperature is usually in the range of 50-200 °C. In most cases the solvent, like benzyl alcohol, works at the same time as solvent and as oxygen supplier for the formation of the oxidic compound.

In this thesis the feasibility of this method for the synthesis of nanoparticles of transition metal oxide was assessed. Powders of RuO_2, IrO_2, Co_3O_4, $CuO_x(OH)_y$ were produced. When different precursors of the same cation are used, the morphology of nanoparticles varies.

Chapter 1. Introduction

1.1 The energy problem

Energy is essential for life. As a consequence, a competitive, reliable and sustainable energy system is essential for world economy. Current average global energy consumption sits at approximately 14 terawatt (TW, 14 x 10^{12} Joules s^{-1}). The energy demand is expected to increase, because of the increase in world population and claims for higher standards of living. Furthermore the rapid industrialization of emerging economies, like China and India, implies a great increase in the energy consumption and the global energy demand is expected to double to about 25–30 TW by 2050 [1]. The world energy consumption grows as technical progress spreads globally.

More than 80% of this energy actually comes from oil, coal, and natural gas and less than 1% comes from renewable power sources such as geothermal, wind, solar power, and biofuels. Oil and gas are preferentially used because of the ease of transport and storage, but their combustion is responsible for emissions of greenhouse gases and other air pollutant compounds (CO_2, CO, SO_2, CH_4, volatile organic compounds) and they are subjected to exhaustion. Furthermore, in recent years, variability in oil prices, interruptions to energy supply, blackouts, together with evidences of climate changes contributed to bring the energy issue to the attention of world politics and public awareness. So the heavy dependence on fossil fuels originates a number of socio-economical, geopolitical and environmental problems. The development of enhanced oil recovery techniques plays a significant role in the estimation of recoverable quantities, which now include very heavy types of oil. Each year they are re-evaluated as being higher than in previous years. However, the recoverable reserves depend also on the involved cost of exploitation. Furthermore coal, oil and gas are considered the main contributors to the anthropogenic production of carbon dioxide CO_2 and emissions of methane CH_4. Wood and other products from biomass also produce CO_2 through their combustion. Since CO_2 and CH_4 are the two major contributors to greenhouse effect, the impact of these energy sources on the environment cannot be neglected.

The Intergovernmental Panel on Climate Change stated that from the beginning of the XX century there has been an increase both in the average surface temperature and in the

average concentration of CO_2 in the atmosphere [2]. A reduction of the emission rate of CO_2 is urgently required. In order to meet this goal, new energy conversion systems of higher efficiency are needed and renewable energy sources have to be exploited more intensively.

Today, developing sustainable and renewable energy sources is seen as a priority in all highly developed countries. Furthermore, the cost of imported fuels heavily affects the economies of many countries, causing political and economic unrest. The issues of national security, independence from imports, the prospects for economies and possible social implications provide the main reason for extensive funded researches on new renewable as well as conventional energy sources, conversion and storage technologies.

Problems, motivations, public attitudes, priorities and official policies are very different in different parts of the world. According to the European Commissioner for Research, hydrogen is the answer to the energy question. Others think that wind, solar, tidal, nuclear, etc., can satisfy all energy needs. However, experts now agree that the solution does not rely on one single energy source or technology, but that all possibilities need to be pursued and explored. The 2007 Report on Energy and Climate Change by the World Energy Council emphasizes that no single energy source can meet the energy needs of the world and its emission goals at the same time, nor can any single policy or measure provide the full solution [3]. The challenge is to supply more abundant and clean energy, consuming fewer natural resources and find the appropriate solution for each region of the world.

Each country should develop its own strategy to fulfill energy needs. Possible technological options and policy decision should be assessed on the basis of the following criteria: i) accessibility to affordable energy, ii) environmental acceptability of the energy sources, and iii) reliable and safe availability.

In view of the rising costs of fossil fuels and growing environmental pollution, the "hydrogen economy" is seen as a practical solution to the above problems. The key features of an ideal fuel are cleanliness, inexhaustibility, convenience and independence from foreign control. Hydrogen meets all these properties.

1.2 Hydrogen economy

Today the expressions "hydrogen energy", "hydrogen economy", "hydrogen energy system" have entered the scientific literature, newspapers and appear in everyday vocabulary.

During the Second World War, investigations on hydrogen lead to the use of liquid hydrogen in the US space program. In the 1950s, a fuel cell that combined hydrogen and

oxygen to produce electricity and water was developed for space applications. In the 1960s, several scientists proposed the use of solar energy to split water into oxygen and hydrogen, and to later recombine them in a fuel cell.

Scientific interest in hydrogen was given a boost by the 1973 oil crisis. In 1974, during the first conference on Hydrogen Energy, the International Association for Hydrogen Energy was founded [4]. The dream was that of building an energy infrastructure that uses hydrogen as an energy carrier (Figure 1.1). The result would be a clean natural hydrogen cycle, with renewable energy used to split water into oxygen and hydrogen, with the latter used in fuel cells to produce electricity and water.

In the following two decades, oil prices dropped back to historical lows, and the interest in hydrogen and related researches slowed down. But at the same time, other issues became important: fuel cell technology breakthrough, debate over the future of oil, concern over the environmental impacts of the energy system. Thus, the idea of a hydrogen economy started to spread.

In this context, it should be stresses that a real hydrogen economy can be established if enough hydrogen is produced from renewable energy sources to fulfill a great part of the world's needs (Figure 1.2). Technological, industrial and political breakthroughs are still needed before such an economy can be established.

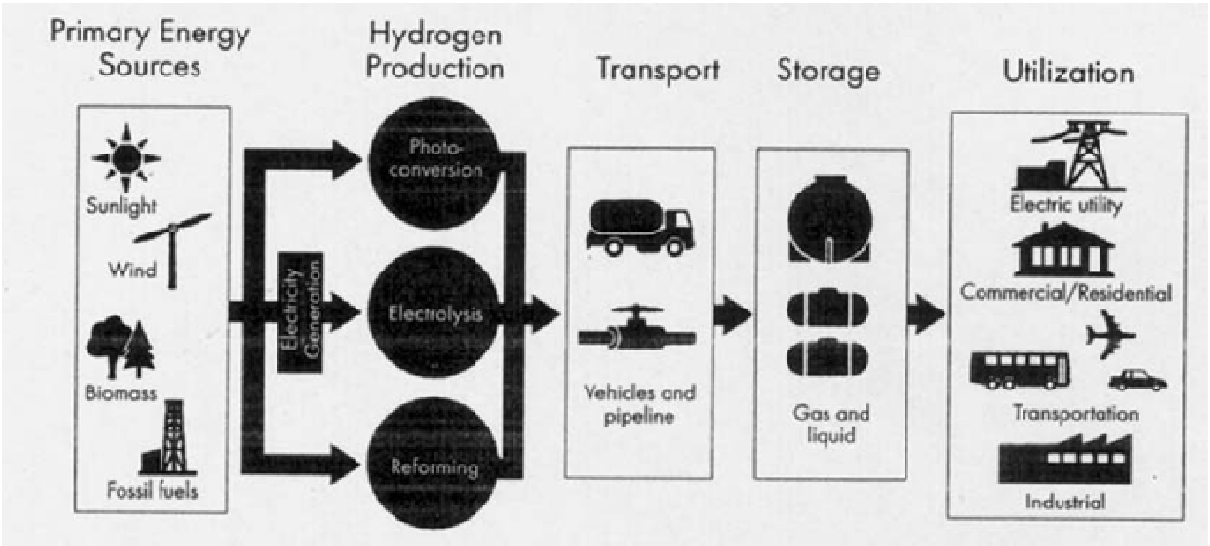

Figure 1.1 A schematic diagram of the hydrogen energy system [5]**.**

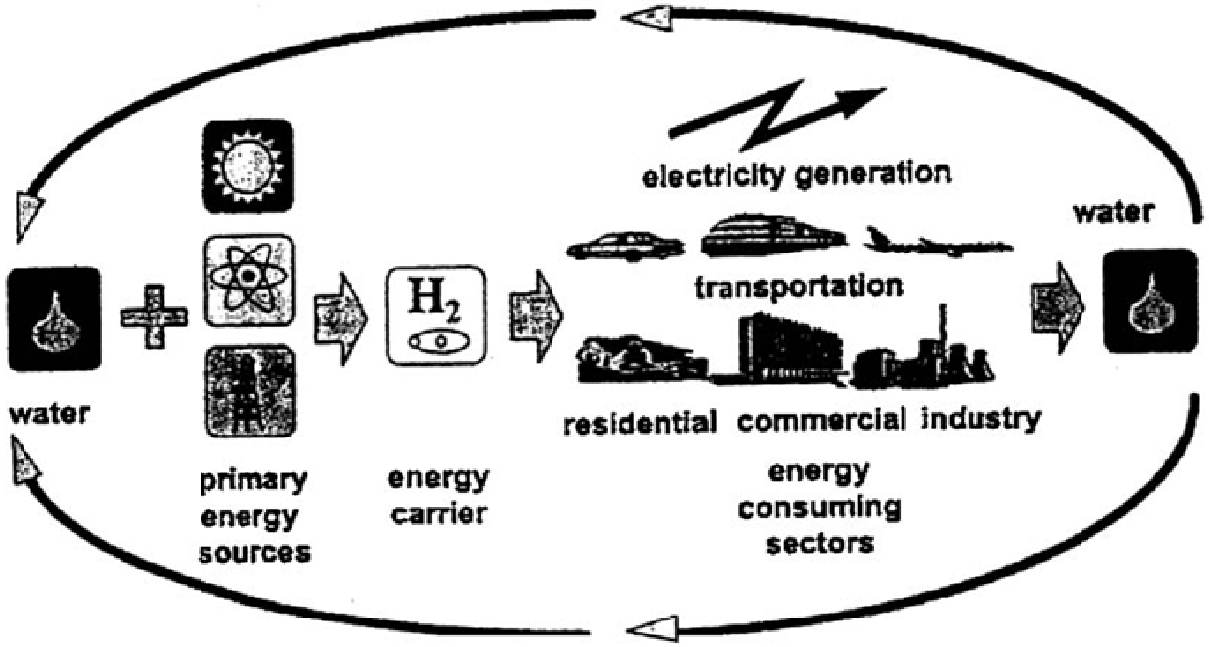

Figure 1.2 A hydrogen economy for sustainability [5]**.**

The need of continuously and instantly meeting the energy demand and of making energy available in places different from the source implies storage and transportation. Unlike fossil fuels, hydrogen is not naturally available as a primary energy source. It is instead a carrier of energy produced from primary sources, including fossil fuels and solar, geothermal, and nuclear [6]. As an energy vector, hydrogen offers the advantage of clean and complete conversion to water. The main disadvantage of molecular hydrogen is the need for large storage volumes. Therefore, the start of the hydrogen economy depends also on scientific and technological advances in storage and distribution of hydrogen.

1.2.1 Infrastructures

A viable, affordable and safe energy system is fundamental to the creation of the hydrogen economy. The final applications include stationary, transportation and portable devices, but a number of problems have to be overcome in order to build sustainable energy infrastructures.

The design of a hydrogen energy system and the choice of the production method will be driven by the demand, the local energy price and the availability of primary energy resources [7]. The cost of electricity, burden by various degrees of taxation, heavily affects the start up of the hydrogen economy and suitable infrastructures to efficiently and safely transport hydrogen have to be developed. In fact, the acceptation of hydrogen relies not only

on its commercial and practical appeal, but also on the development of safety standards and codes.

The system constituted by renewable energy sources, hydrogen and fuel cells requires high investments to reach the level of fossil fuel energy system. A number of crossover issues will influence production, storage, delivery, conversion and applications of hydrogen [8]. The most relevant are the following:

- National and international legislation, codes, and standards for the use of hydrogen
- Policies to lower the additional costs of energy
- Safety standards and environmental regulation
- Collaborative research and development by research centers
- Public education
- Government-industry partnerships
- Feasibility studies

Policy support for hydrogen varies among industrial nations. Governments and industries in the United States, Japan, and Europe are heavily supporting research and development to a sustainable future energy infrastructure based on hydrogen. Some countries, with Germany, Australia and Brazil and the European Union on a larger scale being notable examples, have already made strong commitments to rapid and large-scale conversion to renewable energy and lead in the global investment.

1.2.2 European policies

The European Commission had introduced in 2003 a "European Hydrogen and Fuel Cell Technology Partnership", referred as "Technology Platform", to contribute to an integrated strategy for a sustainable hydrogen economy in Europe [9]. The objectives were to spread awareness of hydrogen and fuel cells, their concepts and structures, to align ongoing and new research project and to formulate recommendations. Three fields of interest were highlighted: i) hydrogen infrastructure, ii) transport applications and iii) stationary applications.

In January 2007 the European Commission adopted a communication proposing an energy policy for Europe [10]. The goal was to combat climate change and boost the EU's energy security and competitiveness. This set out the need for the EU to draw up a new energy path towards a more secure, sustainable and low-carbon economy, for the benefit of all users. One aim is to give energy users greater choice, and another is to encourage investment

in energy infrastructure. Based on the European Commission's proposal, the following targets were asserted:

- reducing greenhouse gas emissions by at least 20% (compared with 1990 levels) by 2020;
- improving energy efficiency by 20% by 2020;
- raising the share of renewable energy to 20% by 2020;
- increasing the level of biofuels in transport fuel to 10% by 2020.

The use of renewable energy sources is seen as a key element in energy policy, reducing the dependence on fuel from nonmember countries, reducing emissions from carbon sources, and decoupling energy costs from oil prices.

The EU Competitiveness Council on May 25, 2010 indicated in its conclusions on the EU Clean and Energy Efficient Vehicles Strategy [11] that "hydrogen vehicles remain a valid ultra-low-carbon mobility option in the medium term perspective, as affordability of the car and of the fuel is achieved; also notes that hydrogen vehicles and electric vehicles are mutually complementary". It also referred to hydrogen vehicles, together with electric battery vehicles, as highly promising ultra-low-carbon technologies. According to the Council, they have the ability to cut local air pollution and noise from transport and contribute to improve the air quality in cities and can promote renewable energy sources and offer a possibility of energy storage. The Council also highlighted the need to focus on research excellence to ensure that alternative automotive receive targeted research financing. Innovative energy storage and conversion technologies, like batteries, fuel cells and the necessary respective infrastructure are included.

A number of hydrogen-fuelled passenger cars and buses are already in circulation. Their number can be increase to a commercial scale, if the price will be lowered through technological development and mass market production processes. Commercialization depends also largely on the development of infrastructure for the production, storage, and distribution of hydrogen and refueling stations. Currently, only a small number of hydrogen refueling stations exist worldwide, and refueling station costs need to be reduced to make them commercially viable.

1.2.3 Hydrogen production

Hydrogen is the most abundant element in the universe, but it does not occur naturally as a gas on the Earth. It is always combined with other elements: with oxygen in water, with

carbon in many organic compounds as hydrocarbons fuels. It can be produced from different starting materials through many different processes.

Hydrogen is already produced and used on large scale by industry. Today it is largely used in the synthesis of ammonia and methanol and in petroleum refinement. The most of hydrogen produced worldwide derives from reforming of fossil fuels (especially natural gas), partial oxidation of heavier oil fractions or gasification of coal. Only a few percent is electrolitically generated where electricity is available at low prices. Electrolytic hydrogen is generally used in special applications like space shuttles and portable fuel cell devices, where higher purity is fundamental. It is also used in food processing and in electronics industry. Small quantities are consumed in pharmaceutical plants.

Steam methane reforming is the most common and less expensive way to produce hydrogen. Coal can also be reformed to produce hydrogen, through gasification. Hydrogen can be extracted from oil, gasoline and methanol though reforming. Unfortunately, all these processes imply environmental pollution and consumption of non-renewable fuels. Furthermore, carbon sequestration technologies are needed to lower CO_2 emissions. Purity of such hydrogen is normally 60 to 70% and at best 98%. However, in order to use hydrogen as fuel for fuel cells, it is necessary to raise its purity up to a value higher than 99.99% and additional energy is required for purification of hydrogen.

In this context, water electrolysis acquires a strategic role. In principle, water electrolysis can be entirely nonpolluting and renewable. Hydrogen of high purity is obtained, but the process is energy consuming. It requires the input of large amounts of electrical energy to split water into oxygen and hydrogen. Consequently, the environmental impact of thus produced hydrogen is largely dependent on the energy source. From this point of view, it cannot be considered a really clean fuel unless the process is energy effective and the eventually produced CO_2 is separated and finally sequestered. For massive use of hydrogen as fuel, production processes must be cost effective too.

Electricity should be supplied by inexpensive renewable energy sources; otherwise no improvement is made in the emitting rate of CO_2 as compared with the conventional fossil-fuel electricity generation. Electrolysis from renewable energy would result in a very clean hydrogen cycle. The use of nuclear energy for this purpose is another option, since additional CO_2 is not emitted in running a nuclear power plant.

Other methods of hydrogen production are thermo-chemical water decomposition, photolysis, photo-biological processes, production from biomass, and various chemical industrial processes where H_2 is a by-product. Some algae and bacteria, using sunlight as their

energy source, even give off hydrogen under certain conditions. Another promising option is photo-electrochemical water splitting, which offers long-term potential for sustainable hydrogen production with low environmental impact.

Hydrogen can be produced on a large scale at dedicated hydrogen production plants or on a small scale at local production facilities. Large-scale production benefits from economies of scale and plants located near power and water, but claims for suitable storage and delivery technologies. Some methods of hydrogen production, like from coal or biomass, can only be undertaken on a large scale [12]. In the case of small-scale production, the problems related to transportation are avoided by using energy that is easily brought to the facility, such as electricity, natural gas, or solar. On the other hand, the amount of equipment required is significantly high if compared to large-scale facilities. At the extreme small scale, fossil fuels could be reformed to hydrogen on board a fuel cell vehicle, but the systems are complex and costly.

1.3 Water electrolysis

Although the production of hydrogen by water electrolysis is not currently cost-competitive if compared with reforming, it represents a process where hydrogen can be produced by true renewable and fully environmentally friendly energy sources (solar, wind, and hydro), without co-production of CO_2.

The schematic diagram of a typical water electrolysis system for hydrogen production is shown in Figure 1.3. The system mainly consists of an electrolysis cell, a separator, and two heat exchangers.

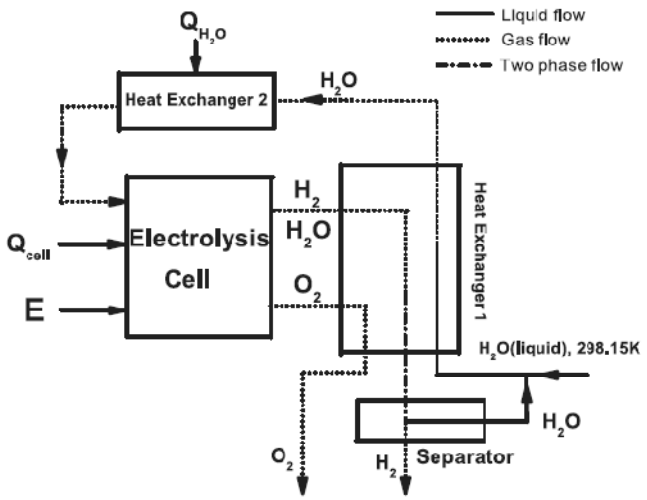

Figure 1.3 The schematic diagram of a typical water electrolysis system for hydrogen production [13]**.**

In the electrolysis process, water is electrochemically splitted into gaseous oxygen and hydrogen. Equation (1.1) clearly shows that the splitting of water by the action of electricity:

$$H_2O + 2F \rightarrow H_2 + \tfrac{1}{2}O_2 \quad (1.1)$$

where F is the Faraday constant (96485 C mol^{-1}), is a clean process since no polluting by-products are formed.

The production of hydrogen by water electrolysis on an industrial scale dates back on the beginning of the 1900s, with the increasing need for large amounts of hydrogen for ammonia synthesis. At that time, water electrolysis was the most economic among the chemical processes able to produce hydrogen with high purity, because of the low cost of hydroelectric. In 1939, the first large water electrolysis plant of 10000 Nm^3 H_2/h capacity started to operate and, in 1948, Zdansky/Lonza built the first pressurized industrial electrolyzer [14].

The electrolytic method was largely applied until the mid-1900s, when the rising costs of electric power and the abundant availability of hydrogen from natural hydrocarbons confined the use of electrolytic hydrogen to cases where the purity of hydrogen is strictly needed, such as in the pharmaceutical industry, hydrogenation in the food industry and so on.

In the 1970s, the first energy crisis led to a renewed interest in water electrolysis. The interest was focused on hydrogen as an energy vector that could possibly replace fossil fuels in the world economy. When the cost of fossil fuels decreased to the levels before the 1970s, the research in improving water electrolysis slowed down.

Although energy requirements for electrolytic process are very high, (about 4.5-5 kWh/Nm^3 H_2 in most industrial electrolyzers) electrolytic process of water decomposition has gained importance in recent years because of the expectation of production with low environmental impact.

One of the most important ideas for water electrolysis development is the possibility of using the same technology for fuel cells, but with the reverse reaction. The reverse of the splitting reaction:

$$H_2 + \tfrac{1}{2}O_2 \rightarrow H_2O + 2F \quad (1.2)$$

occurs in an H_2-O_2 fuel cell. In fact, the same technology can be used for both processes, that is, the same cell can work as an electrolyzer or as a fuel cell, depending on the operating conditions [15]. This is not the case with other competing reactions for the production of H_2.

1.3.1 State of the art

For water electrolysis to become a more efficient process energy loss has to be minimized and the equipment cost has to be lowered. In order to meet the demand of this growing issue, the economics and technology concerning electrolytic process of hydrogen production are rapidly changing.

Industrial water electrolysis has traditionally being carried out in liquid alkaline electrolyte [16-18]. The operation principle of alkaline water electrolysis is reported in Figure 1.4(a) [19]. In particular, about 30% KOH is used at about 80 °C. KOH is more expensive than NaOH, but its use is justified by two reasons: (1) KOH is more conductive (about 1.3 times) than NaOH and (2) KOH is chemically less aggressive than NaOH. Traditionally, the electrode materials for the alkaline electrolysis have been iron or mild steel for cathodes and nickel or nickel-covered iron for anodes [20]. These materials exhibit excellent chemical resistance to KOH and satisfactory electrochemical activity. The drawbacks of the conventional alkaline technology are mainly related to low specific production rates, high energy consumption, low efficiency, voluminous systems, and safety issues related to use of caustic electrolytes.

Starting from the 1970s, several advances have been achieved in the technology, leading to a decrease in the cost of the electrical energy consumption. Briefly, advances have involved (1) activation of electrodes, (2) cell design, (3) proton exchange membrane (PEM) technology and (4) steam electrolysis.

PEM water electrolysis systems offer several advantages over the traditional alkaline technologies, including greater safety and reliability, higher operating current densities and production rates, greater energy efficiency, construction simplicity and more compact design [21-23]. A basic schematic of a PEM water electrolysis cell is shown in Figure 1.4(b). The PEM water electrolysis cell consists primarily of a PEM on which the anode and cathode are bonded. These electrodes are normally a composite of electrocatalytic particles and electrolyte polymer. Normally, different electrocatalysts are adopted as anode (e.g. IrO_2) and cathode (e.g. Pt). When the electrode layers are bonded to membrane, it is known as the membrane electrode assembly (MEA). As a rule in these systems, the anode has the largest overpotential at typical operating current densities (around 10 kAm^{-2}).

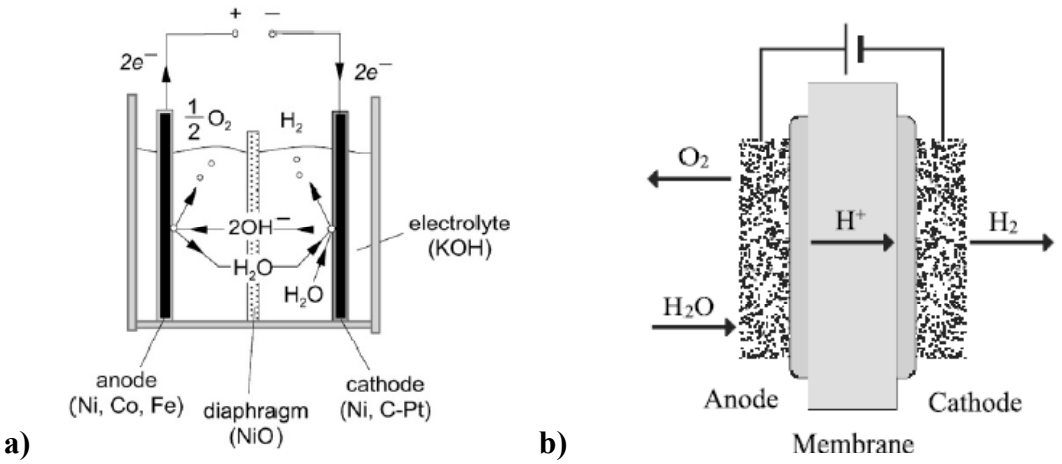

Figure 1.4 Schematic representation of alkaline (a) and PEM water electrolyzer (b).

The concept of PEM technology (a zero-gap cell using a proton-conducting solid polymer electrolyte) was proposed half a century ago, at the dawn of the US space program, when new energy management devices operating in a zero-gravity environment were needed. Nowadays, the European Commission (EC) is actively supporting different projects within the 6th and 7th Framework Programmes [24].

Nowadays, there is no large scale use of PEM water electrolysis systems, with only a very few commercial systems available. The restricting aspects of these systems is the high cost of the materials such as the electrolyte membrane and noble metal-based electrocatalysts, as well as the complex system components to ensure safe and reliable operation. This is mainly due to the use of noble metals (Pt, Ir, and Ru) as electroactive catalyst materials.

There are many attempts to make the electrolytic production more efficient. Besides the reduction of electricity cost, also the reduction of the energy required for the process can be attempted. Different approaches are suitable, like zero-gap cell geometry and development of new electrocatalytic materials for the electrodes.

There is a great need to develop more active, efficient, stable, and cheap electrocatalysts for water splitting in the PEM electrolyzer, that would offer low overpotentials for the hydrogen evolution reaction (HER) at rather high current densities (1-2 A cm^{-2}), lowering the cost of hydrogen production.

1.4 Aim of the thesis

The present thesis is not intended to cover the entire spectrum of hydrogen economy. Rather, it focuses on selection, production and optimization of electrocatalytic materials to improve the efficiency of hydrogen electrolytic production. This is an important factor with

outstanding potential to reduce operational costs of hydrogen production. The present thesis concerns the preparation of several electrode materials and the evaluation of their electrocatalytic properties towards the reactions of H_2 evolution and O_2 evolution.

From a catalytical point of view, H_2 evolution is a "facile" reaction. HER has been studied on several electrode materials, looking for more efficient conditions (lower overpotential and higher electrocatalytic activity). Furthermore, this reaction has been used in the attempt to build a theory of electrocatalysis [25].

In general, the research on the HER catalysis has been focused on several important parameters, like the nature of the reaction, electrode composition, surface morphology, structural, chemical and electronic properties and physical, chemical, and electrochemical activation treatments. Three properties play an important role in selecting catalytically active materials for the HER: (i) an intrinsic electrocatalytic effect of the material, (ii) a large active surface area per unit volume ratio and (iii) catalyst stability. Consequently, the approach used in the design of good HER electrocatalysts should be based on the increase of the active surface area of the electrode material as well as on the design of a catalyst with a high intrinsic catalytic activity.

At the same time, scrutiny of efficient electrode materials for O_2 anodic evolution is needed. The reaction of O_2 evolution (OER) is indeed more energy demanding and affects the global energy balance severely. Therefore, development and optimization of the technology of electrolytic hydrogen production implies the evaluation of both cathodic and anodic processes.

Selection and development of materials to optimize electrode performance is a field of restless research work. In the large amount of work available in the literature, it is difficult to find a unifying idea guiding design and optimization of catalysts. Since the method of electrode preparation severely affects the electrocatalytic activity, synthetic methods and electrode assembly have to be carefully scrutinized for each material.

During the three years of my Ph.D., materials for both hydrogen and oxygen evolution from aqueous solution were prepared, characterized, and tested for performance. A list of materials and experimental conditions is shown in Table 1. Characterization was carried out by electrochemical (cyclic voltammetry and cathodic polarization), as well as non electrochemical techniques (scanning electron microscopy SEM, X-ray diffraction XRD) to check morphology and composition.

In the field of cathode activation, there are two convenient ways to reduce costs and energy consumption: i) replacing active materials with less expensive ones; ii) enhancing the

activity of cheaper materials so as to approach the performance of more expensive catalysts. (IrO_2+Co_3O_4) and (RuO_2+NiO_x) mixed oxides were thus synthesized. Mixed oxides allow to modulate the electrode properties through synergetic effects, which arise from the intimate electronic interaction of the components. As a matter of fact, the behavior of electrocatalysts depends on the nature of the electrode material as well as on its surface morphology, the latter depending on the method of preparation. Both standard thermal decomposition as well as innovative synthetic strategies were applied in this thesis.

As in the case of hydrogen, oxygen evolution preferentially occurs at surface active sites. Therefore modification of number and nature of the active sites would also enhance the electrocatalytic activity for anodic reactions. Besides reducing the size of crystallites, the formation of new active sites can be promoted by such treatments, as laser beams and atom bombardment, which deeply modify the surface. In the present thesis, such a strategy was applied to RuO_2, because it is one of the most active materials for O_2 evolution and its standard behaviour was been extensively investigated.

Catalyst	**Synthesis**	**Support**	**Reaction**
IrO_2-Co_3O_4	*Thermal decomposition*	*Titanium*	H_2 evolution
RuO_2-NiO	*Thermal decomposition*	Titanium	H_2 evolution
RuO_2-NiO	*Thermal decomposition*	Nickel	H_2 evolution
RuO_2-NiO powders	Non-aqueous sol gel	Titanium	H_2 evolution
RuO_2	*Thermal decomposition + laser irradiation*	Titanium	O_2 evolution
RuO_2	*Thermal decomposition + Kr bombardment*	Titanium	O_2 evolution
RuO_2 nanoparticles	*Non-aqueous microwave assisted*	Titanium	H_2 evolution
IrO_2, PtO_x, Re_2O_3, Co_3O_4, $CuO_x(OH)_y$	*Non-aqueous microwave assisted*		

Tab. 1 Investigated materials

The determination of the electrochemical properties of supported oxide nanoparticles is of great interest in both fundamental and applied research. In fact, they can exhibit different and sometimes novel properties compared with that of bulk materials. This consideration is the basis of recent researches on the electrochemical properties of nanoparticles of IrO_2 and RuO_2. Through the combination of non-aqueous synthetic routes with microwave irradiation, several metal oxide nanoparticles can be prepared with good yields in a reasonably short time range (30 sec to 20 min). The reduction of reaction time is considerable if compared to heating in oil bath or in autoclave (typical of sol-gel processes). The initial reaction mixture just consists of the organic solvent and the metal precursor. In most cases an organic polar

solvent, like benzyl alcohol, works at the same time as solvent and as oxygen supplier for the formation of the oxidic compound. The non-aqueous microwave-assisted synthesis approach is in principle less complicate than the aqueous sol-gel route. Regarding size and shape of nanoparticles, it offers better control than thermal decomposition. In this thesis the feasibility of this method for the synthesis of nanoparticles of transition metal oxide was assessed. Powders of RuO_2, IrO_2, Co_3O_4, $CuO_x(OH)_y$ were produced.

1.4.1 Thesis organization

The topics presented in this Thesis have been the object of scientific communications presented at national and international meetings, and gave rise to one paper published in the international literature. A brief overview of each chapter is given in the following.

Chapter 2 provides an overview on electrocatalysis. The focus is on HER and OER.

Since several electrode materials were produced and evaluated, they are separately discussed in chapter from 3 to 7. Each chapter is self-consistent, with experimental part, method and discussion of results. Very general conclusion will be provided in Chapter 8.

In Chapter 3, the behaviour of (IrO_2+Co_3O_4) electrodes prepared by thermal decomposition is investigated in alkaline solution towards the reaction of H_2 evolution.

In Chapter 4, the electrocatalytic performances of (RuO_2+NiO_x) mixed oxides towards HER are illustrated. When (RuO_2+NiO_x) electrodes were prepared by thermal decomposition, different behaviour is observed depending on the nature of the support (Ni or Ti).

In Chapter 5, a new synthetic route for (RuO_2+NiO_x) mixed oxides is presented. RuO_2-based materials were synthesized by a sol-gel route in non-aqueous media and NiO_x was used to distort the RuO_2 crystal structure.

In Chapter 6, the effects of surface modification induced by laser irradiation and atom bombardment on RuO_2 are shown.

In Chapter 7, preliminary results on the synthesis and characterization of metal oxide nanoparticles by a non-aqueous microwave assisted method are introduced.

In Chapter 8, some general conclusions are provided.

1.5 References

[1] J. Baxter, Z. Bian, G. Chen, D. Danielson, M.S. Dresselhaus, A.G. Fedorov, T.S. Fisher, C.W. Jones, E. Maginn, U. Kortshagen, A. Manthiram, A. Nozik, D.R. Rolison, T. Sands, L. Shi, D. Sholl, Y. Wu, Energy & Environmental Science 2 (2009) 559-588.

[2] Intergovernmental Panel on Climate Change (IPCC), Climate Change 2001: The Scientific Basis, Summary for Policymakers, Working Group I Contribution To the Third Assessment Report Of the IPCC, Geneve, 2001.

[3] World Energy Council, Energy and Climate Change Study, London, 2007.

[4] T.N. Veziroglu, International Journal of Hydrogen Energy 25 (2000) 1143-1150.

[5] M. Momirlana, T.N. Veziroglu, International Journal of Hydrogen Energy 30 (2005) 795-802.

[6] F. Orecchini, International Journal of Hydrogen Energy 31 (2006) 1951-1954.

[7] G. Marbán, T. Valdés-Solís, International Journal of Hydrogen Energy 32 (2007) 1625-1637.

[8] S. Dunn, International Journal of Hydrogen Energy 27 (2002) 235-264.

[9] EUR 20719 EN – Hydrogen Energy and Fuel Cells. A Vision of Our Future, European Communities, Luxembourg, 2003.

[10] EU Commission Communication COM(2007) 1 Final, 2007.

[11] EU Commission Communication COM(2010)186 Final, 2010.

[12] J.R. Rostrup-Nielsen, T. Rostrup-Nielsen, Cattech 6 (2002) 150-159.

[13] H. Zhang, G. Lin, J. Chen, International Journal of Hydrogen Energy 35 (2010) 10851-10858.

[14] W. Kreuter, H. Hofmann, International Journal of Hydrogen Energy 23 (1998) 661-666.

[15] E. Guerrini, S. Trasatti, in: P. Barbaro, C. Bianchini (Eds.), Catalysis for Sustainable Energy Production, Wiley-VCH, Weinheim, 2009, p. 235.

[16] D. Pletcher, F.C. Walsh, Industrial Electrochemistry, Chapman and Hall, London, 1990.

[17] M.H. Miles, Electroanalytical Chemistry and Interfacial Electrochemistry 60 (1975) 89-96.

[18] H. Wendt, V. Plzak, Electrochimica Acta 28 (1983) 27-34.

[19] O. Ulleberg, International Journal of Hydrogen Energy 28 (2003) 21-33.

[20] D.E. Hall, Journal of The Electrochemical Society 128 (1981) 740-746.

[21] A. Marshall, B. Børresen, G. Hagen, M. Tsypkin, R. Tunold, Energy 32 (2007) 431-436.

[22] F. Barbir, Solar Energy 78 (2005) 661-669.

[23] S. Grigoriev, V. Porembsky, V. Fateev, International Journal of Hydrogen Energy 31 (2006) 171-175.

[24] P. Millet, D. Dragoe, S. Grigoriev, V. Fateev, C. Etievant, International Journal of Hydrogen Energy 34 (2009) 4974-4982.

[25] M.M. Jaksic, Journal of Molecular Catalysis 38 (1986) 161.

Chapter 2. Electrocatalysis: an overview

Electrocatalysis is the field of electrochemistry where theoretical aspects have a most direct impact on technology and applications [1].

The origin of the term *electrocatalysis* is still controversial. The first authors to introduce the term ‘‘catalytic electrode reactions’’ were Bowden and Rideal in 1928, who observed that different electrode surfaces exhibit different currents for a certain reaction under the same electrode potentials. It seems from the literature that Russian scientists were the pioneers in the field of electrocatalysis since 1934 [2]. According to Bockris and Khan [3], the term was introduced by T. Grubb in 1936, in his work on fuel cells.

All these controversies aside, the definition of electrocatalysis is now widely accepted. It is the branch of electrochemistry that deals with the effect of the electrode material on the rate and the mechanism of electrode reactions. The change in the rate and selectivity of electrochemical reactions is achieved by the catalytic action of electrodes, upon whose surfaces these reactions occur. Since electrocatalysis occurs on active surface sites and these sites involve an electron transfer, in principle all electrodes that are the sites of reaction involving adsorbed intermediates can be regarded as electrocatalysts. In practice, only electrodes on which electrochemical rates are faster than the rates for the same reaction on other electrodes are addressed as electrocatalysts.

In the present chapter, after a brief overview on general aspects of electrode kinetics, the main factors governing electrocatalysis will be illustrated. Particular attention will be paid to the reactions of hydrogen and oxygen evolution, which are involved in water electrolysis.

2.1 Electrode kinetics

At equilibrium, an electrochemical reaction is characterized by an electrode potential, E_{rev}, determined by Nernst equation. Experience demonstrates that the electrode potential strongly affects the kinetics of reactions occurring on its surface. As an example, hydrogen evolves rapidly at some potentials, but not at others. This is true for all faradaic processes, which involve electron transfer occurring across the electrode/electrolyte interface and lead to reduction or oxidation of species present at the interface. The kinetics of a reaction is also

influenced, among the others, by the nature and the structure of the reacting species, the solvent, the electrode material and adsorbed layers on the electrode.

At E_{rev}, the common value of the rate of electrochemical events across an interface in opposite directions is called "exchange current density", j_0. It measures the degree of reversibility on an electrode reaction and can be obtained from experimental data.

If E is moved away from E_{rev}, the system will be no more in equilibrium and a current will flow across the electrochemical cell and in the external circuit. Thus, in order to drive electrochemical reactions at a practical rate, a potential difference must be applied to the system. The applied potential includes a thermodynamic contribution (E_{rev}) and a kinetic contribution, determined by energy dissipation. The amount of electrical energy dissipated to overcome reaction resistances is called overpotential.

$$\eta = E - E_{rev} \tag{2.1}$$

As previously said, the potential of an electrode strongly affects the kinetics of all faradaic processes occurring on its surface. The rate of the electron transfer reaction at the electrode surface can be varied by changing the applied electrode potential, η. The phenomenological model of Butler-Volmer is able to relate the reaction rate (current density) with η:

$$j = j_0 \left[e^{(1-\alpha)nF\eta/RT} - e^{-(\alpha nF\eta)/RT} \right] \tag{2.2}$$

This must be regarded as the fundamental equation of electrode kinetics. It shows the way in which current density, j, varies with exchange current density, j_0, overpotential, η, and transfer coefficient, α. Plots of j *vs*. η result in the so-called polarization curves.

Energy dissipations in an electrochemical system are mainly due to activation energies, composition gradients across the interface and ohmic resistances.

Activation overpotential, η_{act}. If mass transfer effects are negligible, it is possible to determine the effect of overpotential on the current. In such case, the overpotential is a measure of the energy spent to overcome the activation energy. When j_0 is large, a small change in η results in a large variation of the current. Essentially there is little or no activation barrier to the reaction. When j_0 is very small, then a large value of η is needed to alter the current. In this case there is a high barrier to activation and so the rates of the electrode processes become slow.

Depending on the overpotential value, two cases can be distinguished.

For small values of the overpotential ($|\eta| \leq 5$ mV), equation (2.2) approaches a linear form:

$$j = \frac{j_0 nF}{RT}\eta \tag{2.3}$$

Equation (2.3) shows that the current density is linearly related to the overpotential within a narrow potential range near equilibrium. The slope of this equation represents the charge transfer resistance.

For large values of the overpotential, ($|\eta| \geq 50$ mV), the following equations are obtained from equation (2.2):

$$\overleftarrow{j} = j_0 \mathrm{e}^{(1-\alpha)nF\eta/RT} \tag{2.4}$$

$$\vec{j} = j_0 \mathrm{e}^{-(\alpha nF\eta)/RT} \tag{2.5}$$

Equations (2.4) and (2.5) are usually plotted in semi-logarithmic form. The plot $\log j$ *vs*. η is universally known as Tafel line and it is a useful device for evaluating kinetic parameters.

Tafel lines are generally represented by two branches, one with a positive (anodic) and one with a negative (cathodic) slope. The plot deviates from linear behaviour as η approaches zero, because the back reaction can no longer be neglected.

The relationship between η and $\log j$ is usually simply written as:

$$\eta = a + b \log j \tag{2.6}$$

with:

$$a = \frac{2.303RT}{\alpha nF}\log j_0 \tag{2.7}$$

$$b = \frac{2.303RT}{\alpha nF} \tag{2.8}$$

a and b are the Tafel intercept and the Tafel slope. They can help in determining reaction mechanism, because the Tafel slope has a well-defined value for a well-defined mechanism. Furthermore, if the linear section of Tafel lines is extrapolated to zero overpotential, the intercept gives the exchange current density, j_0. The method of extrapolation of a linear section of the Tafel line to η=0 is a simple method to determine j_0. The extrapolation is realized in the high overpotential range. However, the methods introduces a degree of uncertainty, because relies upon the assumption that the Tafel slope is constant and independent of the overpotential.

Concentration overpotential, η_{conc}. As an electrode reaction proceeds, reactants are consumed and products are accumulated near the electrode surface. Thus, concentration profiles are formed and sustain diffusion fluxes of species towards or away from the electrode. Because mass transfer steps are usually slower than interfacial charge transfer

steps, the global rate of the electrode reaction will be limited by diffusion. Under similar circumstances, the concentration of the reactants at the reaction site will be lower than that in the bulk of the solution, c_i. Thus, to obtain a reaction rate commensurate to c_i, it is necessary to take the potential to a higher value.

Ohmic resistances. If ohmic resistances are present in the cell, ohmic drops, *IR*, contribute to the overpotential. Ohmic resistances include contributions from electrolyte, electrodes and electrical connections. They can be a consequence of poor conductivity of the electrode material and/or finite distance between the electrode surface and the point where the reference electrode senses the electrode potential. In principle, *IR* is not an overpotential because it does not affect directly the reaction rate. However, ohmic drops dissipate electrical energy.

Concentration overpotentials and ohmic drops affect the shape of the polarization curve [4]. They can be minimized but not totally eliminated. However, they can be mathematically corrected to extract the Tafel line from experimental data. If η_{conc} and/or *IR* are operative, experimental Tafel lines are non linear. In particular, if ohmic drops distort the Tafel line, corrections can be attempted by two graphical approaches [5]. They will be introduced in following chapters.

2.1.1 Tafel slope and reaction order

Kinetic parameters depend only on the details of the mechanism and not on the chemical nature of the species involved. The current, *I*, is an extensive quantity, since it depends on the size of the electrode. The current density is an extensive quantity too, because it is linked to the geometric surface area of electrodes. However, electrodes are usually rough and the real surface area differs from the geometric surface. On the other hand, the Tafel slope, *b*, is an intensive quantity. It depends only on the reaction mechanism and not on the size of the electrode. For this reason *b* is the most important kinetic parameter. The way the Tafel slope depends on the Tafel slope can be derived by analyzing reaction mechanisms.

Reaction mechanism for electrode reactions can be described through a sequence of steps, either electrochemical (denoted by E) or chemical (denoted by C). Each mechanism for a given rate determining step (rds) gives a well defined Tafel slope, which is determined by the nature of the steps up to the rds only. The following steps are fast and their nature does not affect the kinetic parameters. The equation of Tafel lines can be obtained by writing down the expression of the reaction rate of the rds and calculating the concentration of the intermediates from the equilibrium Nernst equation applied to the sum of the steps preceding the rds. If it

can be assumed that all steps preceding the rds are at equilibrium and that the coverage of electrode surface with adsorbed intermediates (θ_i) is close to 0, it is possible to write:

$$b = \frac{2.303RT}{f(\alpha)F} \tag{2.9}$$

where α is assumed to be 0.5. Let's consider the following mechanism: ECEC. If the first E is the rds, b=(2.303RT/αF) and results 120 mV. If the mechanism is EC*EC (with * indicating the rds), b=(2.303RT/F)=60mV. With ECE*C, b=[2.303RT/(1+α)F]=40mV. If the mechanism is ECEC*, b=(2.303RT/2F)=30mV.

In case $\theta \approx 1$, steps preceding the rds can no longer be considered at equilibrium and the kinetic analysis should be performed case by case. As an example, for an EC* mechanism, b evolves from 60 mV to infinity, because as the surface is saturated with intermediates, the reaction rate is governed by the rate of chemical reaction. In the same way, for an EE* mechanism b evolves from 40 mV to 120 mV, as θ_i turns from 0 to 1. Such a mechanism results in a broken Tafel line, with two linear sections. Broken Tafel lines originates also from a transition from one to another rds in the same mechanism. As a rule, in a multistep reaction, a change in rds with increasing overpotential leads always to an increase in Tafel slope.

Reaction order. Reaction orders, β_i, provide useful information in elucidating the reaction mechanism, both in chemical reactions and electrode processes.

For an electrochemical reaction, the reaction order can be determined either at constant potential, E, or constant overpotential, η. The reaction order determined at constant E is chemically significant and can be expressed as follows:

$$\beta_i = \left(\frac{\delta \ln j}{\delta \ln a_i} \right)_{T,p,E,a_{j \neq i}} \tag{2.10}$$

where a_i represent the activity of the species i. The plot ln jvs. ln a_i gives a straight line, whose slope is the reaction order, β_i with respect to the species i. Analytical relationships between reaction order and Tafel slope can be derived from kinetics equation [6].

If double-layer effects are operating, the distortion of Tafel lines affects also the reaction order. Fractional reaction orders are indicative of possible double-layer effects [7].

2.2 Electrocatalysis

As in chemical kinetics, activation energies depend on the strength of chemical bonds formed and/or broken between the electrode surface and reactants, products or intermediates. Thus, if the electrode is modified, the activation energy and/or the reaction mechanism will be

modified. An electrocatalyst modifies the energetics of the reaction path, as it changes the activation energy which is proportional to the reaction rate.

Electrocatalysis is of great importance in improving the operating efficiency of electrolyzers. It deals with the search for new materials or new operating conditions in order to improve activity, efficiency and selectivity of electrodes, reduce investment and operational costs, increase the electrode life time and avoid pollution. Activity can be improved looking for new synthetic routes to known materials or new composite materials with synergetic effects. On the other hand, reduction of costs can be obtained by replacement of expensive active materials with cheaper ones. Nevertheless, non-noble materials are usually less active and need to be activated by suitable treatments.

The criterion for choosing an appropriate material electrode for practical applications implies a compromise among important factors such as electrocatalytic activity, thermodynamic stability, corrosion resistance, and fabrication costs.

Electrocatalytic activity is always assessed on a relative basis, by comparing the current density at constant overpotential or the potential at constant current density. The aim is to achieve higher rates at lower overpotentials. If current density is normalized to the apparent geometric surface area, electrocatalytic effects will also include geometric effects. This is apparent electrocatalysis. If current density is normalized to the real surface area (to a certain degree), true electronic effects will emerge.

Comparison of Tafel lines for different materials is the most common way to assess their relative activity. The relative position of two Tafel lines can be modified by modifying both geometric and electronic factors, the Tafel slope changes only if the mechanism changes. In this respect, the search for new materials or the optimization of existing materials is oriented to obtain as low Tafel slopes as possible. As a matter of fact, lower Tafel slopes allow lower energy consumption for the same production rate.

Two properties play an important role in selecting catalytically active materials for electrochemical reaction: the actual electrocatalytic effect of the material and its long-term stability. Usually, dealing with the suitable electrocatalyst only involves the electrochemical aspects. They are of importance with respect to the catalytic activity. The long-term stability also depends on actual working conditions and is, as such, a matter of electrochemical engineering.

2.2.1 Factors of electrocatalysis

A fundamental issue in electrocatalysis is the establishment of relationships between the properties of a given material and its electrocatalytic behaviour. Several properties affect the performance of an electrocatalyst: electronic properties, surface structure, different active sites, particle size, surface composition, and so on. All these properties can be roughly divided in electronic factors and geometric factors [8-10].

Electronic factors are related to the strength of the surface-intermediate bonds and depend on the surface chemical structure and composition. On the other hand, geometric factors are solely related to the extension of the actual surface area or actual site concentration. They influence the reaction rate but are not directly related to real electrocatalysis, because they do not affect the activation energy of the reaction. As a rule, electronic and geometric factors are closely interrelated. Nevertheless, a separation should be attempted in order to better understand why some materials exhibits better electrocatalytic performances than others [11].

In terms of current density, the knowledge of the real surface area would allow the separation of the two factors. Assuming that the concentration and the nature of active sites don't change, if a plot of log *j vs*. the real surface area at a constant potential gives a straight line, the effects are more likely to be geometric only. If the correlation deviates from linearity, electronic factors are most likely to be operating [12]. This approach will be applied in the discussion of transition metal oxides in the following chapters.

Electronic effects. The specific interaction between the electrode material and the reacting species is defined by the overlap of the electronic states of the reactant and the electrode material at the transition state. A strong overlap takes place when specific interactions exist. Outer-sphere reactions are always weakly overlapping. On the other hand, inner-sphere reactions can be strong or weak overlapping reaction, depending on the properties of the reactant and electrode material. Normally, if the reaction rates depend on the electrode material and its surface structure, it can be said that the electrode is acting as an electrocatalyst.

The theory of electrocatalysis was developed firstly for hydrogen evolution reaction in the second half of 1900. It has been verified that the electrocatalytic activity of simple metals depends on the heat of adsorption of the intermediates on the electrode surface. The reaction rate increases with the Gibbs energy of adsorption, reaches a maximum and then decreases. The result is a curve known as the volcano curve. This behaviour shows that adsorption increases reaction rate, provided that its energy is not too high. If the energy of adsorption is

too high, the adsorbed intermediate is too stable to give the products. This idea originates from the principle of Sabatier [13]. Such curves have been obtained for several electrochemical processes, like hydrogen evolution [14] and oxygen evolution [15].

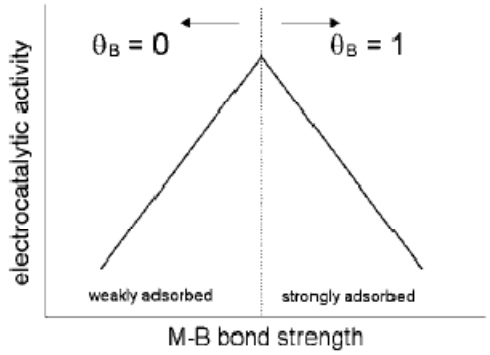

Figure 2.1 Sketch of the dependence of the electrocatalytic activity on the intermediate adsorption bond strength (volcano curve).

Surface structure effects. The adsorption of the species on the electrode surface depends on the structure of the surfaces site. A change in structure of the surface will involve different energy. Furthermore, the changes in surface geometry will lead to variation in the geometry of the adsorption sites and the distance between them. Real surfaces comprise several types of sites, like kinks and steps. The presence of defects in a surface structure plays an important role in the electrocatalytic process. The atoms that constitute defective sites exhibit special adsorption properties, because of a lower coordination number. These properties can result in improved catalytic activity [16]. An example will be provided in Chapter 6, where the effect of laser irradiation and atom bombardment on RuO_2 will be discussed [17].

Surface composition effects. In many cases, the most active metals have only a limited catalytic activity towards the reaction of interest. The modification of the surface properties of the metal is a suitable way to enhance its electrocatalytic activity. In most cases, this can be achieved by depositing a foreign ad-atom on the surface [18] or through the production of composite materials. Several examples can be found in the literature [12,19-21]. Composite materials allow for modulation of the electrocatalytic properties and possibly synergetic effects [22]. The effect of surface composition on electrocatalytic activity of Ir and Co mixed oxides will be discussed in Chapter 3. Mixing two oxides produces several effects. In addition to eventual surface segregation, the surface area is not monotonically related to composition. As a rule, it passes through a maximum at some intermediate compositions, which can be

interpreted as being related to decreasing particle size. Examples will be provided in the discussion of Ru and Ni mixed oxides (Chapter 4 and 5). Also stability is affected by mixing.

The two factors governing electrocatalytic activity are at the basis of the actual trends in research for more efficient electrocatalysis. In order to maximize the surface area, materials are more and more dispersed so as to increase the surface-to-volume ratio. On the other hand, new and more specific technologies of preparation are being tested in the search for conditions resulting in more and more enhanced surface area. The possibility to improve the activity of single-compound material is limited, so a lot of combinations have been investigated, looking for untested materials or improved already known electrocatalysts.

Conventional electrolysis in alkaline environment can be improved by using activate cathodes and anodes [23-25]. For anodes, Fe-doped Ni-based oxides exhibit the best performance. For cathodes, Ni-based activated electrodes are still a good choice. Furthermore, transition metal oxides like IrO_2 and RuO_2 are very good catalyst for the reaction of hydrogen evolution [26]. Looking at water electrolysis in acidic media (PEM electrolyzer), the extreme anodic conditions restrict the choice to mixture of IrO_2 with SnO_2, Ta_2O_5 and RuO_2 [27]. In the case of cathodes, most materials are not stable in contact with the acidic membrane. However, the MEA allows the use of gas diffusion electrodes. Thus, dispersion powdered material supported on carbon can be used [28]. An example will be shown in Chapter 7, dealing with nanoparticles of transition metal oxides.

2.3 The hydrogen evolution reaction

The hydrogen evolution reaction (HER) is certainly one of the most intensively studied electrochemical reactions [29].

The reaction of H_2 formation involves two electrons per mole of H_2:

$$2H^+ + 2e \rightarrow 2H_2 \tag{2.11}$$

in acid solutions ($E°$ = 0 V (RHE)) and

$$2H_2O + 2e \rightarrow H_2 + 2OH^- \tag{2.12}$$

in alkaline solutions ($E°$ = -0.8282 V (RHE)).

HER is catalytically non demanding, because only monoatomic species are involved as intermediates. Furthermore bonds formed and broken during the reaction are of moderate strength. Thus, activation energies are moderate. The global reaction rate is closely related to the energies of adsorption of the water molecule at the surface site (M) and desorption of intermediate atomic hydrogen formed by electron transfer.

HER occurs by a multi-step reaction and the now generally accepted mechanism is based on the following steps:

$$M + H^+ + e \rightarrow H_{ads} \tag{2.13}$$

$$MH_{ads} + H^+ + e \rightarrow M + H_2 \tag{2.14}$$

$$MH_{ads} + MH_{ads} \rightarrow 2M + H_2 \tag{2.15}$$

where the initial discharge step (2.13), involving an adsorbed H intermediate, H_{ads}, is followed by either the recombination of the H_{ads} to form H_2 (2.15) or electrochemical desorption of H_{ads} to form H_2 (2.14). Depending on the electrocatalytic properties of the electrode material, H_2 evolution proceeds through (2.13)+(2.14) or (2.13)+(2.15). Thus, the adsorbed intermediate can undergoes two alternative pathways, depending on the nature of the electrode. The electrochemical desorption is known as ion+atom recombination or Heyrovsky reaction and the chemical recombination step is known also as Tafel reaction. In acidic solutions, H_3O^+ ion is the proton source for the initial discharge step (2.13), while in alkaline solutions H_2O itself is the proton source.

Mechanistic studies to elucidate the elementary steps involved in HER are generally based on the determination and interpretation of kinetic parameters such as Tafel slope, reaction order and stoichiometric number obtained at a given electrode material.

Tafel slope values are predicted by theory. If the first discharge (2.13) is the rate determining step, Tafel slope values of 120 mV are observed. Tafel slope is 40 mV if the reaction (2.14) is the rate determining step and it is 30 mV if the chemical recombination (2.15) is rate determining. When the coverage of the electrode surface by intermediates, θ_H, is high, a Tafel slope of 120 mV is expected if reaction (2.14) is rate determining and a limiting current is expected if reaction (2.15) is rate determining.

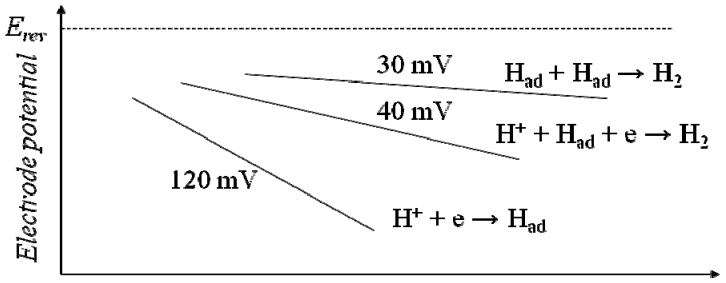

Figure 2.2 Steps involved in HER mechanism and relative Tafel slopes.

Steps	$\theta_H \approx 0$		$\theta_H \approx 1$	
	b	RO	b	*RO*
E	120 mV		–	
EC	60 mV		∞	
EE	40 mV	2	120 mV	1
EEC	30 mV	2	∞	0

Table 2.1 Tafel slope and reaction order predicted by theory for HER.

For materials which bind intermediate weakly, the mechanism is (2.13)+(2.14) and Tafel slopes of 120 mV are obtained. These are poorly active electrode materials. A Tafel slope of 30 mV is an indication of very active materials. This is the case of materials which bind intermediate strongly. However, on most active metals, H_2 evolution proceeds through (2.13)+(2.15), with (2.15) being the rate determining step.

Sometimes, Tafel lines with two different Tafel slope are observed. This can indicate a change in θ_H but can also point out for a change in the rate determining step. If Tafel slope turns from 40 mV to 120 mV, this means that at low current densities electrochemical desorption is rate determining, while at higher current densities the primary discharge becomes rate determining. In very few cases, a Tafel slope of 60 mV has been observed.

In the case of hydrogen evolution, the theory of electrocatalysis on single metals is well established. It has been verified that the electrocatalytic activity of simple metals depends on the heat of adsorption of the intermediates on the electrode surface. A useful guide for the choice of suitable electrocatalytically active material is the volcano-type curve, representing the relationship between the log j and different properties dependent on the electron configuration of the metal [14,30,31] .

The field is more complicated when dealing with composite materials, like the mixed transition metal oxides discussed in this work. Because a unifying leading idea does not yet exist, a convenient approach for selection and development of electrodic materials is “try and see”.

2.3.1 Materials for cathodes

Pt is the reference electrode material for H_2 evolution, because of its high activity. Nevertheless it is not suitable for practical applications. In practice, iron and mild steel in acidic solution and Ni in alkaline solution have long been used as cathode materials [9,32]. In alkaline electrolyzer, Ni is usually considered a quite good electrocatalyst, but its activity and stability decrease in time. Production of activated cathodes is a suitable way to overcome this problem. Activation has been attempted with several materials, from sulfides to oxides, from alloys to intermetallic compounds [33].

Precious metals are among the most active materials. After the advent of precious metals oxide as DSA, it was discovered that these oxides are active even for cathodic processes, like HER [34].

Oxides are unique cathode materials. In principle, precious metal oxides like IrO_2 and RuO_2 are thermodynamically unstable in the conditions of H_2 evolution. In practice, they are very active and enough stable also in strongly reducing conditions. This behaviour is due to their electronic conductivity [35,36].

2.4 The oxygen evolution reaction

Oxygen evolution is of great technological importance. It is the anodic reaction in water electrolysis and occurs in a few other industrial processes, like metal electro-winning and electro-organic reductions. Unfortunately, it is more complicated than hydrogen evolution, and is still a very active area of research.

The reaction of O_2 formation at the anode involves four electrons per mole of O_2:

$$2H_2O \rightarrow O_2 + 4H^+ + 4e \tag{2.16}$$

in acidic solutions ($E°$ = 1.229 V (RHE)) and

$$4OH^- \rightarrow O_2 + 2H_2O + 4e \tag{2.17}$$

in alkaline solutions ($E°$ = 0.401 V (RHE)).

The reaction is catalytically demanding. In fact, high-energy intermediates with complex molecular structure and complicates reaction pathways are involved. The rate of O_2 evolution at a given electrode thus is highly sensitive to the nature and the structure of the electrode material.

A generalized mechanism on oxide electrode materials has been proposed. The first step involves the discharge of water molecules (in acid) or OH^- (in alkali) on a surface active site (S):

$$S + H_2O \rightarrow S\text{-}OH^* + H^+ + e \tag{2.18}$$

where -OH* is an unstable adsorbed intermediate, which need stabilization by a surface rearrangement or a surface migration to a more active site:

$$S\text{-}OH^* \rightarrow S\text{-}OH \tag{2.19}$$

The more stable species thus undergoes an electrochemical oxidation:

$$S\text{-}OH \rightarrow S\text{-}O + H^+ + e \tag{2.20}$$

and O_2 is finally evolved in the last step:

$$2S\text{-}O \rightarrow 2S + O_2 \tag{2.21}$$

Other mechanisms can be proposed [37], however the following common conclusion is valid: the reaction occurs through the formation of unstable higher oxides and their following decomposition (M is the metal atom):

$$MO_x + H_2O \rightarrow MO_{1+x} + 2H^+ + 2e \quad (2.22)$$

$$MO_{1+x} \rightarrow MO_x + \tfrac{1}{2}O_2 \quad (2.23)$$

The analysis of reaction mechanism is mostly based on the value of the Tafel slope. A broad range of Tafel slopes is observed on oxide electrodes, from 30 mV up to 120 mV depending on electrode material and electrolyte. Usually two different Tafel slope values can be observed as a function of overpotential, a lower slope (typically 40-60 mV) at low overpotentials and a higher one (120 mV) at high overpotentials. Transitions in Tafel slopes are usually attributed to change in rate determining step of the same mechanism or change in mechanism. Furthermore, the factor that mainly affects the Tafel slope on different oxides is the strength of interaction between the oxide surface and oxygenated intermediates [15,38].

For materials which bind intermediates weakly, usually high overpotentials for OER are observed. According to the proposed mechanism, step (2.18) is the rate determining step (Tafel slope close to 120 mV). On the other hand, if oxygenated intermediates are adsorbed strongly, step (2.18) is very fast and step (2.19) or (2.20) become rate determining. In more detail, step (2.21) is rate determining on oxides that exhibit a 40 mV Tafel slope, step (2.19) on oxides with 60 mV Tafel slope. These materials are more active electrocatalyst.

As a consequence of OH^- or H_2O oxidation, atomic oxygen and oxygenated intermediates are formed and they are strongly adsorbed on metal surfaces. O_2 evolution always takes place on a metal surface covered by a film of metal oxide. The thickness of this film depends on the affinity of oxygen for the metal as well as on the mechanism of growth. As a consequence, it is possible to obtain a wide range of electrode materials with different degrees of hydration and stoichiometry through the variation of the procedure of formation. This possibly enables the modulation of the activity of a given nominal oxide for O_2 evolution.

Reaction order is another kinetic parameter which can be useful to identify the rate determining step in a reaction mechanism. Integral reaction order between 0 and 2, either positive or negative, are predicted. However, fractional reaction orders are observed, between 0.5 and 1.5, when the rate determining step is an electrochemical one [7,39] .

Experimental observations of kinetic parameters for O_2 evolution can be explained in terms of the acid-base properties of oxide surfaces in aqueous solutions [39]. Oxide surfaces

interact strongly with water molecules, becoming covered by a carpet of OH groups which behave as weak bases or weak acids. In aqueous solution, the dissociation of OH groups gives rise to a phenomenon of surface charging:

$$\text{S-OH} + \text{H}^+ \rightleftarrows \text{S-OH}_2^+ \tag{2.24}$$

$$\text{S-OH} + \text{OH}^- \rightleftarrows \text{S-O}^- + \text{H}_2\text{O} \tag{2.25}$$

Dissociation of OH groups is a function of the pH of the solution. The pH at which an oxide surface is electrically neutral is referred as the point of zero charge (pzc). Since pzc depends on the nature of the metal ion-OH group chemical interaction, it is an intensive property. Oxides with basic pzc are highly stable in alkaline solutions and undergo dissolution in acidic solutions. Viceversa, oxides with acid pzc are stable in acidic solution and much less in alkaline ones.

2.4.1 Materials for anodes

The main requisites needed for an electrode material to be useful for technological applications for the OER are: high surface area, high electrical conduction, good electrocatalytic behavior, minimization of the gas bubble problem, low cost, and safety as regards health [15].

A number of metals and alloys have been tested as electrocatalysts, and nickel and noble metals are thought to be the best anode materials in alkaline and acid solutions, respectively. An oxide layer is always formed at the surface in the potential region at which oxygen evolves, even if an inert metal electrode is used as the anode. Therefore, the oxide formed on the metal substrate always affects the reaction mechanism and electrocatalysis for the OER [37].

Although the activity of Ni decreases with time, it has been traditionally used as anode in water electrolysis from strongly alkaline solutions. The advent of DSA in the chlor-alkali technology led to the development of activated anodes. As a matter of fact, transition metal oxides prepared by thermal decomposition on Ni showed better electrocatalytic performances than Ni itself. In the case of water electrolysis, Ni is typically used as a support in alkaline solutions and Ti is used in acidic solutions.

The anodic stability of oxides used as electrodes can be predicted on the basis of the point of zero charge (pzc). Acid oxides are expected to be stable in strongly acidic media, while basic oxides are stable in alkaline solutions. As a matter of fact, IrO_2 (pzc < 2) is the most stable oxide electrode in strongly acidic solution under O_2 evolution. On the other hand, NiO (pzc > 9) is among the most stable oxide electrodes in strongly alkaline solutions. Co_3O_4

and $NiCo_2O_4$ are among the most active materials for O_2 evolution in alkaline solutions. Their activity is further increased if a small amount of Fe oxide is added [40]. Water electrolysis is feasible in strongly acidic medium too, thanks to the development of proton-conducting membranes. In this case, precious transition metal oxides (in particular IrO_2 and RuO_2) constitute the active component of electrode materials.

2.5 References

[1] S. Trasatti, International Journal of Hydrogen Energy 20 (1995) 835-844.

[2] J.O. 'M Bockris, Trans. Faraday Soc. 43 (1947) 417.

[3] J.O. 'M Bockris, S.U.M. Khan, Surface Electrochemistry: A Molecular Level Approach, Plenum Press, New York, 1993.

[4] M. Stern, L. Geary, Journal of The Electrochemical Society (1957) 56.

[5] D.M. Shub, M.F. Reznik, Soviet Electrochemistry 21 (1985) 878-882.

[6] B.V. Tilak, B.E. Conway, Electrochimica Acta 37 (1992) 51-61.

[7] A. Carugati, G. Lodi, S. Trasatti, Materials Chemistry 6 (1981) 255- 266.

[8] V.S. Bagotzky, Y.B. Vassiliev, I.I. Pyshnograeva, Electrochimica Acta 16 (1971) 2141-2167.

[9] S. Trasatti, in: H. Gerischer, C.W. Tobias (Eds.), Advances In Electrochemical Science and Engineering. Vol 2, VCH, Weinheim, 1992, p. 1.

[10] S. Trasatti, in: A. Wieckowski (Ed.), Interfacial Electrochemistry: Theory, Practice and Applications., Marcel Dekker, New York, 1999, pp. 769-792.

[11] E. Guerrini, S. Trasatti, Russian Journal of Electrochemistry 42 (2006) 1017-1025.

[12] C. De Pauli, S. Trasatti, Journal of Electroanalytical Chemistry 538-539 (2002) 145-151.

[13] R.I. Masel, Principles of adsorption and Reaction on Surfaces, John Wiley, New York, 1996.

[14] S. Trasatti, Journal of Electroanalytical Chemistry 39 (1972) 163-172.

[15] S. Trasatti, Electrochimica Acta 29 (1984) 1503-1512.

[16] E. Herrero, J.M. Feliu, A. Aldaz, in: Encyclopedia of Electrochemistry, Wiley-VCH, 2007, p. 443.

[17] E. Guerrini, A. Colombo, S. Trasatti, Journal of Chemical Sciences 121 (2009) 639-646.

[18] I. Bianchi, E. Guerrini, S. Trasatti, Chemical Physics 319 (2005) 192-199.

[19] X.M. Liu, X.G. Zhang, Electrochimica Acta 49 (2004) 229-232.

[20] M. Musiani, Electrochimica Acta 45 (2000) 3397-3402.

[21] V. Dusastre, J.A. Kilner, Solid State Ionics 126 (1999) 163-174.

[22] S. Trasatti, Portugaliae Electrochimica Acta 19 (2001) 197-208.

[23] T. Schmidt, H. Wendt, Electrochimica Acta 39 (1994) 1763-1767.

[24] H. Wendt, H. Hofmann, V. Plzak, International Journal of Hydrogen Energy 9 (1984) 297-302.

[25] H. Suffredini, J.L. Cerne, F.C. Crnkovic, S.A.S. Machado, L.A. Avaca, International Journal of Hydrogen Energy 25 (2000) 415-423.

[26] I.M. Kodintsev, S. Trasatti, Electrochimica Acta 39 (1994) 1803-1808.

[27] A. Marshall, S. Sunde, M. Tsypkin, R. Tunold, International Journal of Hydrogen Energy 32 (2007) 2320-2324.

[28] S. Grigoriev, P. Millet, V. Fateev, Journal of Power Sources 177 (2007) 281-285.

[29] B.E. Conway, B.V. Tilak, Electrochimica Acta 47 (2002) 3571-3594.

[30] M. Jaki, Electrochimica Acta 45 (2000) 4085-4099.

[31] A.C.D. Angelo, International Journal of Hydrogen Energy 32 (2007) 542-547.

[32] J. De Carvalho, G. Tremiliosi Filho, L. Avaca, E. Gonzalez, International Journal of Hydrogen Energy 14 (1989) 161-165.

[33] E. Guerrini, S. Trasatti, in: P. Barbaro, C. Bianchini (Eds.), Catalysis for Sustainable Energy Production, Wiley-VCH, Weinheim, 2009, p. 235.

[34] S. Trasatti, in: J. Lipkowski, P.N. Ross (Eds.), The Electrochemistry of Novel Materials, VCH, New York, 1994.

[35] S. Trasatti, Electrochimica Acta 36 (1991) 225-241.

[36] J.C.F. Boodts, S. Trasatti, Journal of Applied Electrochemistry 19 (1989) 255-262.

[37] Y. Matsumoto, E. Sato, Materials Chemistry and Physics 14 (1986) 397-426.

[38] S. Trasatti, Journal of Electroanalytical Chemistry 111 (1980) 125-131.

[39] C. Angelinetta, M. Falciola, S. Trasatti, Journal of Electroanalytical Chemistry 205 (1986) 347-353.

[40] E. Guerrini, M. Piozzini, A. Castelli, A. Colombo, S. Trasatti, Journal of Solid State Electrochemistry 12 (2007) 363-373.

Chapter 3. IrO_2 enhancement by Co oxide

3.1 Introduction

Among potential candidates for cathodic electrocatalysts in alkalis, IrO_2 has proved to be as active as RuO_2 and more active than Co_3O_4 [1].

The behaviour of RuO_2-doped Ni/Co_3O_4 electrodes for cathodic hydrogen evolution in alkaline solutions was investigated by Trasatti and coworkers [2,3]. It turned out that less than 10 mol% RuO_2 in a Co_3O_4 matrix allows for the same electrocatalytic response as pure RuO_2.

On the other hand, IrO_2 is even more active than RuO_2 for H_2 evolution [4,5], while the opposite is the case for O_2 evolution . Therefore it is of interest to study the properties of IrO_2+Co_3O_4 mixtures. In the present work, mixed (IrO_2+Co_3O_4) electrodes were produced at different compositions and tested as cathodic material towards the hydrogen evolution reaction in alkaline solutions. The surface properties of mixed oxides were monitored by SEM and cyclic voltammetry in the composition range 0 to 20 mol% IrO_2. Mechanism and electrocatalysis of hydrogen evolution were investigated by cathodic polarization experiments. Tafel slope and reaction order values were determined.

3.2 Experimental

3.2.1 Preparation of Electrode

Ti/(IrO_2+Co_3O_4) electrodes were prepared by thermal decomposition of aqueous 0.1 mol dm^{-3} precursor mixtures. H_2IrCl_6 (Aldrich) and $Co(NO_3)_2 \cdot 6H_2O$ (Aldrich, 98%) were dissolved in deionized water (Millipore). Solutions were brushed onto both faces of a Ti support and calcinated in a pre-heated oven in ambient atmosphere for 5 min at 450 °C. This procedure was repeated until a final oxide loading of 2 mg cm^{-2} was reached. A final annealing for 1 hour at the same temperature was performed. The temperature of calcination was chosen on the basis of thermal gravimetric analysis (TGA) in air. As shown in Figure 3.1, decomposition starts close to 130 °C for both Ir and Co precursors and ends close to 170 °C for Ir and 270 °C for Co. At temperatures higher than 270°C the decomposition to oxide is completed for both compounds.

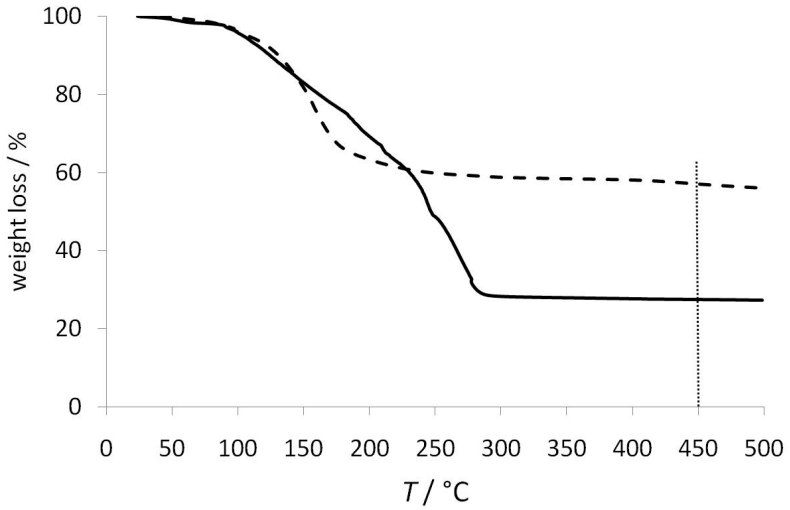

Figure 3.1 Thermogravimetric analysis in air of Ir and Co precursors. Scan rate, 10 °C/min. (——) Cobalt; (- - -) Iridium.

Electrodes were prepared with the following Ir content: 0, 1, 2, 3, 5, 7.5, 10, 15, 20, 100 mol% (three samples at each composition; two sample were used to electrochemical experiments, the third sample was used for SEM analysis).

Ti platelets (10 × 10 × 0.2 mm) with a thin stem on one side were used as a support. Just before the oxide deposition, Ti supports were sandblasted with quartz powder and then chemically etched for 1 h in boiling 10 w% oxalic acid. In order to prevent the formation of TiO_2 which is an interfering in electrochemical experiments, a thin intermediate layer of RuO_2 was deposited between Ti and the active layer. A 0.02 mol dm^{-3} $RuCl_3 \times nH_2O$ solution was brushed onto Ti to prepare a thin RuO_2 layer by thermal decomposition at 450 °C. This approach has been adopted because Ti/Co_3O_4 electrodes show ohmic drop effects related to the passivation of Ti substrate and the presence of an interlayer of RuO_2 can prevent such problems [6].

A thin Cu wire was voltaic-arc welded to the Ti stem to ensure electrical connection. Electrodes were mounted in a Pyrex® tube. The apparent geometric surface area exposed was 1 cm^2 on each of the two faces of the platelets.

3.2.2 Methods of characterization

The morphology of the oxide layer was observed on a LEO 1430 scanning electron microscope (SEM).

Electrodes were studied by cyclic voltammetry (CV) and quasi-steady state polarization curves in 1.0 mol dm^{-3} NaOH (Fluka, 98%) aqueous solutions. Solutions were kept at 25±0.1°C in a water thermostat and were deaerated before each experiment using

nitrogen gas. Experiments were carried out using an EG&G Model 273A potentiostat/galvanostat connected to a personal computer. The four-compartments electrochemical cell contained two Pt counterelectrodes separated from the central compartment of the working electrode by glass frits. The compartment of the reference electrode was connected to the surface of the working electrode by a Luggin capillary. Potentials were read and are reported against a satured calomel electrode (SCE).

Voltammetric curves were recorded at 20 mV s^{-1}. Quasi-steady state polarization curves were obtained by keeping the electrode at open circuit potential (OCP) for 15 min, then at –1.0 V (SCE) for 5 min, then moving the electrode potential by 10 mV steps and reading the current after 1 min at each potential (forward scan). As the current reached about 200 mA, the direction of potential variation was reversed until the current became anodic (backward scan).

The reaction order with respect to H^+ for the cathodic H_2 evolution was determined by varying NaOH concentration between 0.05 and 0.5 mol dm^{-3}, keeping the ionic strength constant by addition of $NaClO_4$. The pH of the solutions was 12.75, 13, 13.25, 13.5, 13.75. The order of reaction was determined by recording potential step experiments. The electrode was kept at -0.4 V for 5 min, then the potential was moved to -1.0 V, -1.25 V, -1.15 V(SCE) (180 sec at each potential). The current related to the step at -1.15 V(SCE) was read directly from the chronoamperometric curve.

3.3 Results

After preparation, fresh samples were observed by SEM. Electrodes were thus subjected to the following experiments:

i) Cyclic voltammetry (CV) in a restricted potential range to obtain the "electrochemical spectrum" of the surface (and the related surface charge).
ii) Quasi-steady state polarization curves for the reaction of H_2 evolution (Tafel lines), followed by CV.
iv) Determination of the reaction order with respect to H^+ in forward conditions of polarization, followed by CV.

3.3.1 Surface morphology

Figure 3.2 shows SEM images of samples at different composition. There is an evident change in morphology as the content of IrO_2 increases. The layer of pure Co_3O_4 is quite smooth and compact. The introduction of IrO_2 in the Co_3O_4 matrix produces increasing cracks and roughness.

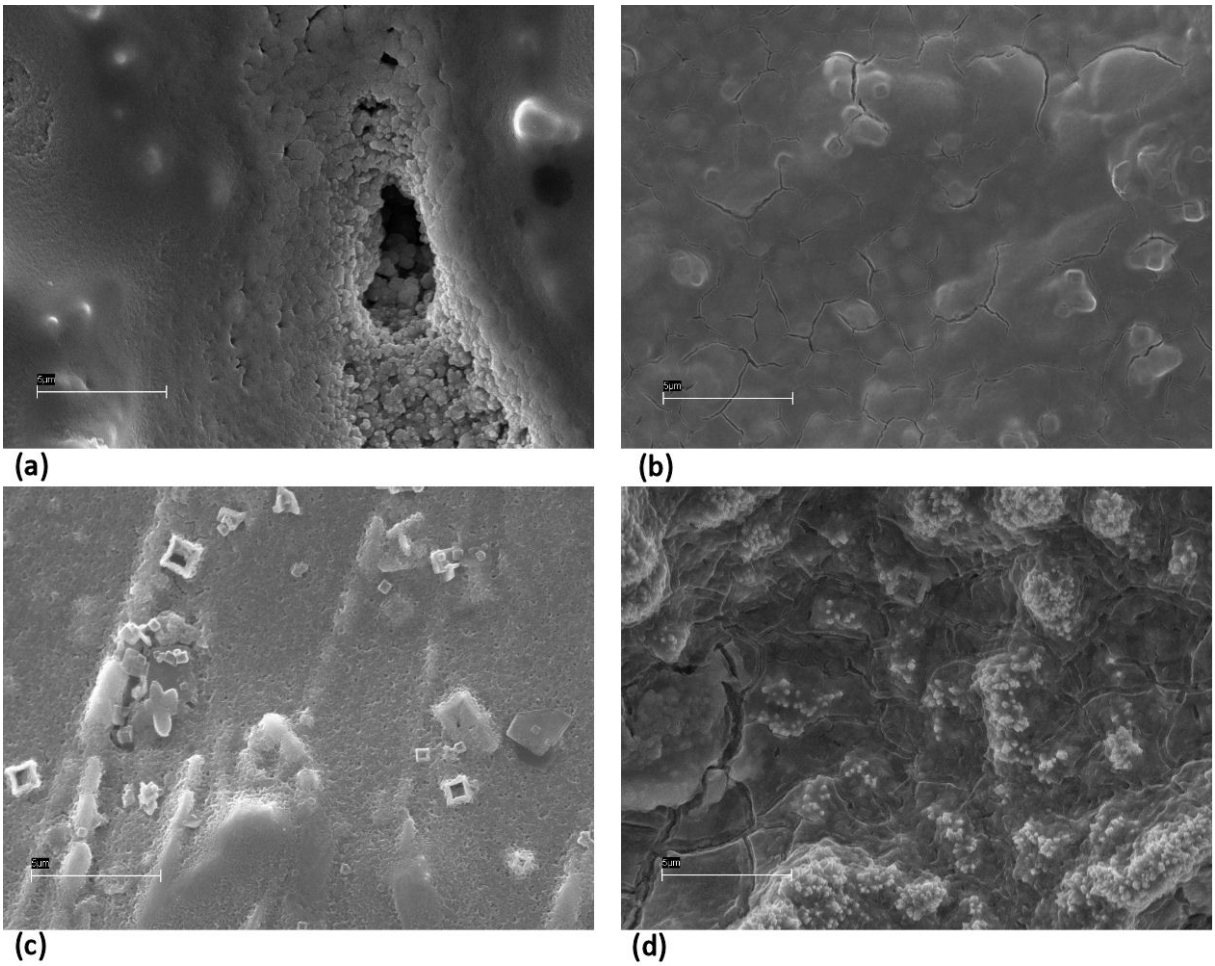

Figure 3.2 SEM micrographs (5000 ×) of fresh samples of IrO_2+Co_3O_4 at different contents of IrO_2. (a) 0; (b) 10; (c) 20; (d) 100 mol% IrO_2. The marker is 5 μm.

SEM pictures at higher magnification are shown in Figure 3.3. When IrO_2 is added to the Co_3O_4 matrix, the electrode surface exhibits a cracked dried-mud look, which is the typical structure of DSA electrodes [7]. However, well defined geometric structures become clearly visible on the surface, as the IrO_2 content increases. The surface is probably composed of small well dispersed IrO_2 particles. At 15 and 20 mol% IrO_2 the morphology is very similar to that of pure IrO_2.

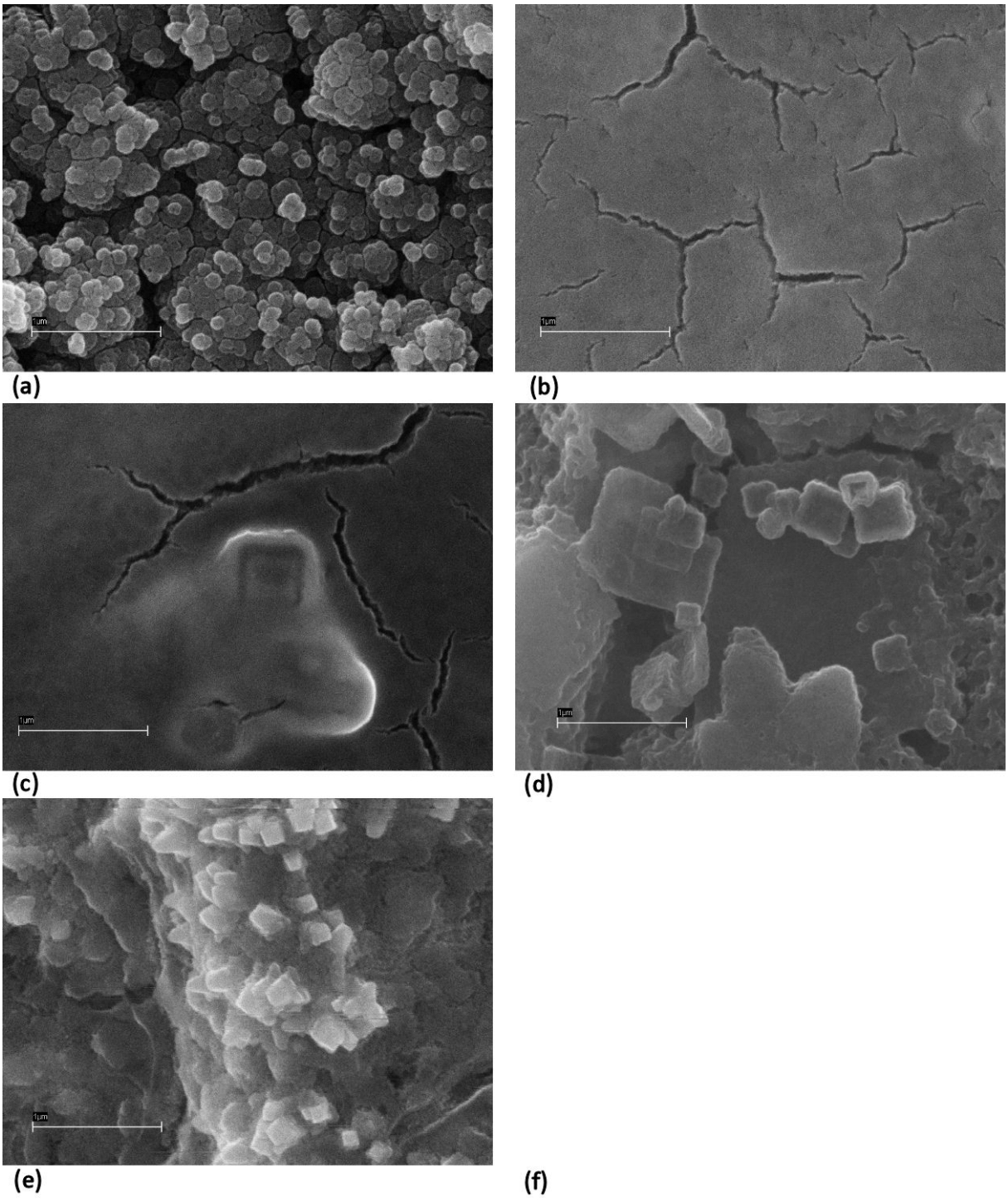

Figure 3.3 SEM micrographs (30000 ×) of fresh samples of IrO_2+Co_3O_4 at different contents of IrO_2. (a) 0; (b) 5; (c) 10; (d) 20; (e) 100 mol% IrO_2. The marker is 1μm.

3.3.2 Voltammetric curves

Voltammetric curves were recorded for fresh samples, for samples after H_2 evolution polarization curves, and for samples after determination of the reaction order. Voltammetric curves are characteristic for a given compound and can give information on surface morphology [8].

Figure 3.4 shows a series of CV curves recorded on fresh electrodes at different composition (from pure Co_3O_4 to pure IrO_2). A typical voltammetric curve for Co_3O_4 in alkaline solution is obtained for 0 mol% IrO_2. The pair of peaks around 0.4 V (SCE) is related to the complete oxidation of the surface of Co_3O_4 to Co(IV), according to the following reaction [9]:

$$CoOH \rightleftarrows CoO_2 + H^+ + e \tag{3.1}$$

Since the Co(III)/Co(IV) redox transition is reversible, anodic and cathodic peak are symmetric. The featureless voltammograms recorded for electrode of pure IrO_2 is typical of thermal IrO_2. The symmetry with respect to x-axis indicates a good pseudo-capacitive behaviour [10].

Shape and area of voltammograms turn from the features of Co_3O_4 to those of IrO_2, as the IrO_2 content increases. More in details, an increasing content of IrO_2 reduces the peak of Co(III)/Co(IV) transition with respect to the capacitive area. Furthermore, the cathodic peak is slightly shifted towards less positive potentials. At 10 mol% IrO_2, the Co_3O_4 peak disappears. The shift of peak potential suggests a possible interaction between the two components.

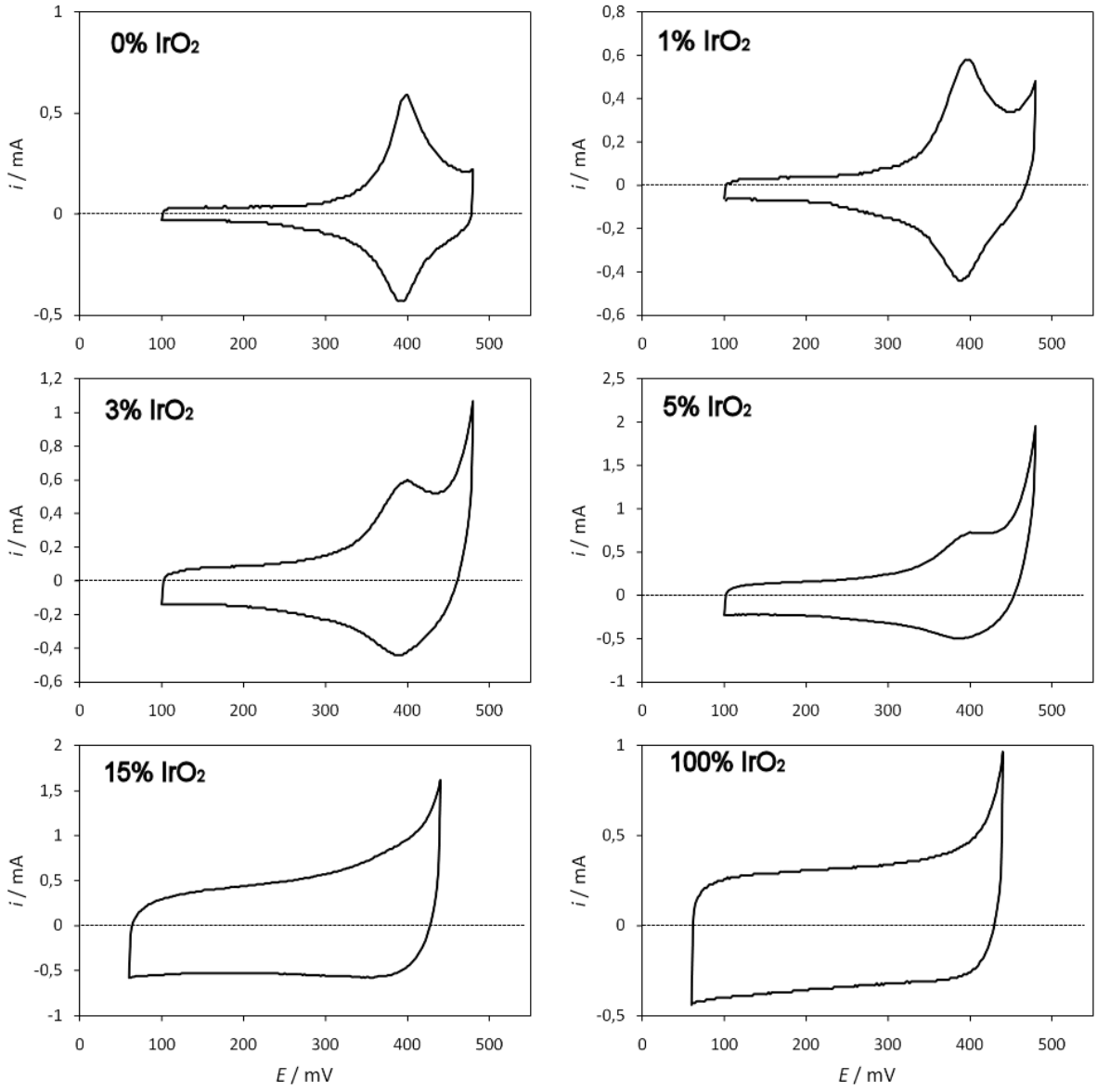

Figure 3.4 Cyclic voltammetric curves at 20 mV s^{-1} in 1 mol dm-3 NaOH solution of IrO_2+Co_3O_4 electrodes with different IrO_2 contents.

3.3.3 Surface charge

The voltammetric charge spent in sweeping the potential in the range 0.06–0.44 V (SCE) was determined by graphical integration of the voltammetric curves. The reported charge density, q^*, is obtained by dividing the total integrated charge by the geometric surface area of the samples (2 cm^2). The voltammetric charge in this potential range can be taken as a relative measure of the electrochemically active surface area. Actually, the charge is proportional to the number of protons exchanged between the solution and the oxide surface, according to the following general redox reaction:

$$M(OH)_xO_y + \delta H^+ + \delta e \rightleftarrows M(OH)_{x+\delta}O_{y-\delta} \qquad (3.2)$$

and it is related to the surface concentration of active sites.

The charge is determined by reaction (3.1) for Co_3O_4 and by the following reaction for IrO_2 [10]:

$$IrO_y(OH)_x + \delta H^+ + \delta e \rightleftarrows IrO_{y-\delta}(OH)_{x+\delta} \qquad (3.3)$$

Figure 3.5 shows the voltammetric charge, q^*, as a function of the nominal composition. The charge increases approximately with a linear trend from 0 to 5 mol% IrO_2 and reaches an almost constant value at 7.5 mol% IrO_2. These data suggest that the surface morphology is dominated by IrO_2 for electrodes with more than 5 mol% of IrO_2 content.

Since voltammetric charge is a measure of the extent of the active surface area, a phenomenon of surface segregation can be inferred. Active surface area increases with IrO_2 content up to 7.5 mol% IrO_2. If IrO_2 content is further increased, the area keeps constant and the electrodes behave as pure IrO_2.

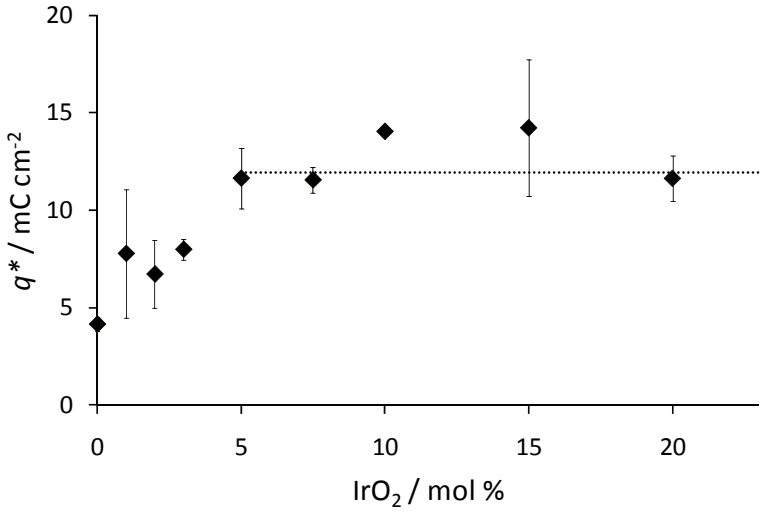

Figure 3.5 Surface charge q^* as a function of nominal composition of IrO_2+Co_3O_4 oxide electrodes. q^* from integration of voltammetric curves. The value for 100 mol% IrO_2 is indicated (···).

3.3.4 Polarization curves

The kinetic behaviour of the electrodes toward the reaction of hydrogen evolution was studied by recording polarization curves. A marked hysteresis was observed between forward and backward polarization scans for electrodes with more than 5 mol% IrO_2. Significant kinetic data are those taken in backward scan, since in forward scan the surface is prepared to hydrogen evolution by some reduction or site rearrangement. In Figure 3.6, a representative polarization curves is plotted as E *vs*. log j. Deviations from Tafel plot are clearly visible at high current densities. They are related to uncompensated ohmic drops and an eventual change in Tafel slope.

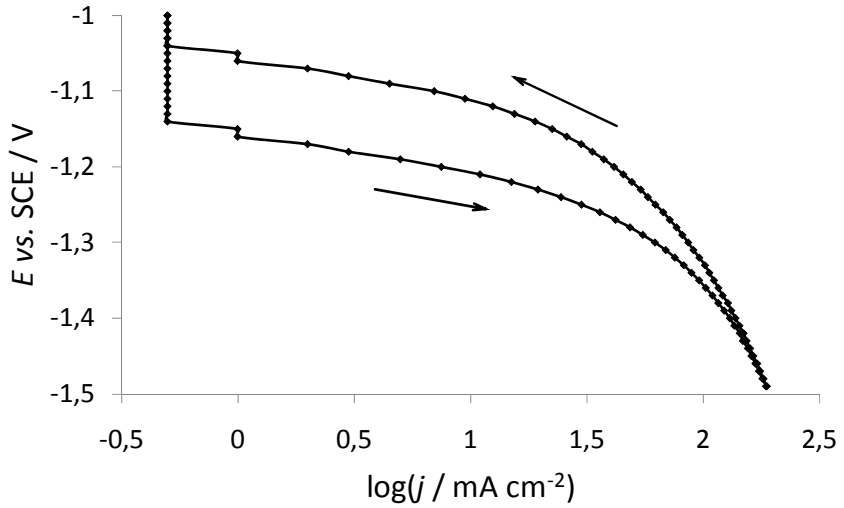

Figure 3.6 Polarization curve for H_2 evolution from 1 mol dm^{-3} NaOH on a Co_3O_4 electrode with 5 mol% IrO_2. Arrows indicate the direction of potential variation.

Tafel slopes and resistance values were obtained by polarization curves using two different approaches: i) derivative method and ii) *IR* compensation method. These two methods are briefly described in the following.

i) In the presence of uncompensated ohmic drops, the electrode potential, *E*, at each current can be written as:

$$E = a + b \log j + jSR \tag{3.4}$$

where *a* e *b* are the Tafel empiric parameters, *j* is the current density, *R* is the resistance and *S* is the geometric surface area. Differentiation with respect to current density *j* gives:

$$\frac{dE}{dj} = \frac{b}{j} + RS \tag{3.5}$$

Thus, a plot of $\Delta E/\Delta j$ *vs.* $1/j$ results in a straight line, whose slope is *b* and whose intercept is *RS* (Figure 3.7). The resulting *R* can be used to correct experimental polarization curves.

ii) A straight line is drawn graphically from the linear part of the experimental polarization curve in the low current range and extended to high currents. The slope of the straight line gives the Tafel slope, *b*. In the high current range of the curve, deviations of the experimental points, ΔE, from the straight line are determined and plotted as a function of current, *I*. If a straight line is obtained (Ohm law), this indicates that deviations are only due to uncompensated ohmic drops, therefore, only one Tafel line is operating. The slope of the *ΔE vs. I* straight line gives the uncompensated resistance (Figure 3.8). If the ΔE *vs. I* plot results in a curve, it means that two different Tafel lines are probably operating, or that the drawn Tafel line is inaccurate.

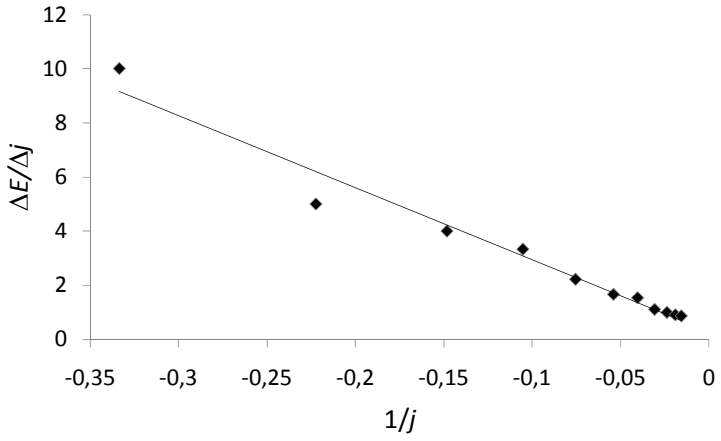

Figure 3.7 Typical plot of $\Delta E/\Delta j$ *vs.* $1/j$

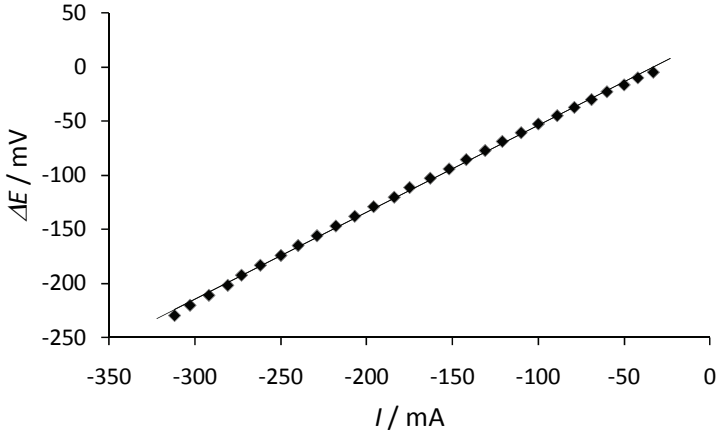

Figure 3.8 Typical plot of ΔE *vs.* I.

The kinetic parameters obtained by the two procedures are summarized in Table 3.1.

	Forward polarization			**Backward polarization**		
IrO_2 / mol%	***b* / mV decade^{-1}**		***R* / Ω**	***b* / mV decade^{-1}**		***R* / Ω**
	low current	high current		low current	high current	
0	49	110	0.69	72	116	0.48
1	65	140	0.97	82	131	0.8
2	40	112	0.76	49	138	1.01
3	51	180	0.6	56	120	0.92
5	43	122	0.47	36	75	0.78
7.5	45	63	0.41	32	55	0.71
10	44	74	0.57	36	55	0.86
15	52		0.30	27		0.68
20	49		0.21	36		0.68
100	68		0.56	66		1.76

Table 3.1 Kinetic parameters for HER on IrO_2+Co_3O_4 electrodes.

The uncompensated resistance, *R*, calculated from polarization curves (Figure 3.6) is lower than 1.0 Ω for most electrodes, as shown in Figure 3.9. *R* entails the solution resistance and eventual ohmic drops in the oxide layer, but the two components cannot be distinguished. The value of *R* increases after massive hydrogen evolution for electrodes with more than 2 mol% IrO_2. Two possible explanations can be proposed: i) the mechanical stress of the electrode due to H_2 evolution destabilizes the catalytic film; ii) Ir_2O_3 (less conductive than IrO_2) originates at cathodic potentials of H_2 evolution [11].

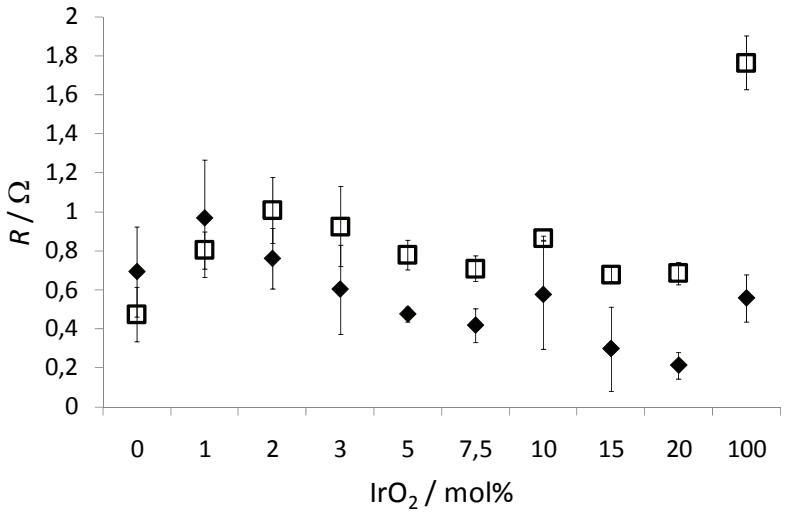

Figure 3.9 Uncompensated ohmic resistance in 1 mol dm^{-3} NaOH solution for IrO_2+Co_3O_4 electrodes as a function of composition. (◆) Forward and (□) backward potential scan. Data from both derivative method and *IR* compensation method are included.

In Figure 3.10, the polarization curves for selected electrodes are reported after the correction for uncompensated ohmic drops. The overpotential decreases as the IrO_2 content increases. Electrodes of pure IrO_2 exhibit higher overpotentials than mixed oxides.

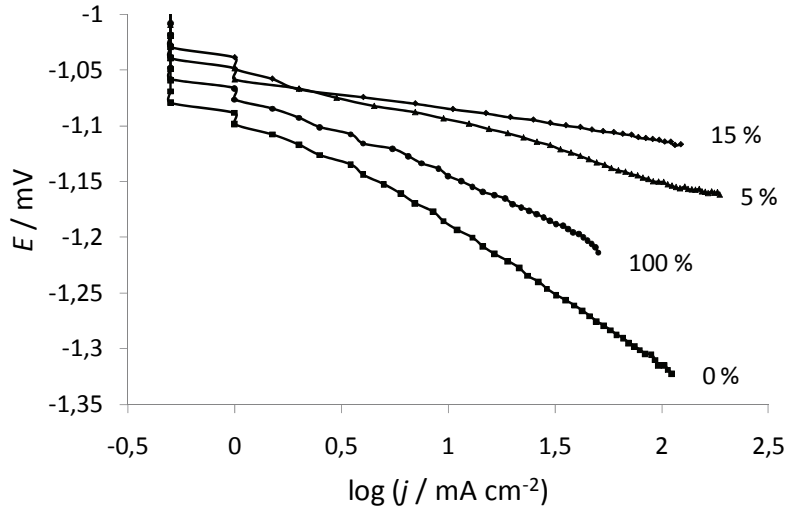

Figure 3.10 Polarization curves corrected for ohmic drop at different IrO_2 content (as indicated).

3.3.5 Tafel slopes

Figure 3.11 shows Tafel slope values in the low current density range for forward and backward scan as a function of nominal composition. Data are the average of values obtained by the two methods described in previous section (2 values × 2 electrodes = 4 data per point). In the forward scan, the Tafel slope increases from 50 mV for pure Co_3O_4 to more than 70 mV when 1 mol% IrO_2 is added to the Co_3O_4 matrix, and then it decreases to less than 50 mV for further addition of IrO_2. Similar trend is observed in the backward scan. In the composition range 3 to 20 mol% IrO_2, the Tafel slope for forward scan is slightly higher than for backward polarization. The lowest values (~30–40mV) are observed in the backward polarization for electrodes with more than 5 mol% IrO_2. Electrodes at intermediate compositions appear to be activated after cathodic hydrogen evolution and this can be related to the high concentration of atomic hydrogen adsorbed on the electrode surface during backward polarization. Electrodes of pure IrO_2 are not activated after H_2 evolution, as suggested by the similar Tafel slope value in the forward and in the backward scan.

As previously said, significant kinetic data are those in backward scan. For this reason, in Figure 3.12 Tafel slope taken in the backward scan at low current densities are reported together with values obtained at high current densities. A second Tafel line of slope close to 120 mV dec^{-1} appears at high current densities for electrodes with lower IrO_2 content. As the IrO_2 content increase up to 10 mol%, a second Tafel line of slope between 55 and 75 $mVdec^{-1}$ is observed. At higher IrO_2 content, a single Tafel line was observed.

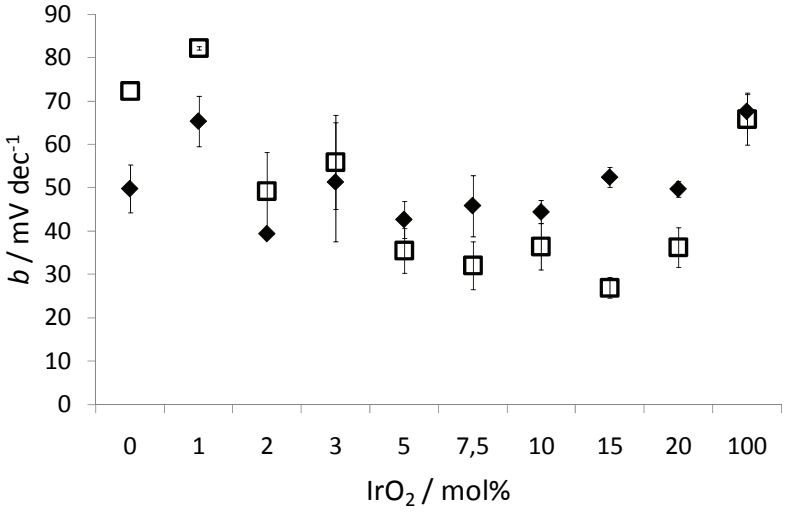

Figure 3.11 Tafel slope for H_2 evolution at low current density from 1.0 mol dm^{-3} NaOH solution on IrO_2+Co_3O_4 electrodes as a function of composition. (◆) Forward and (□) backward potential scan.

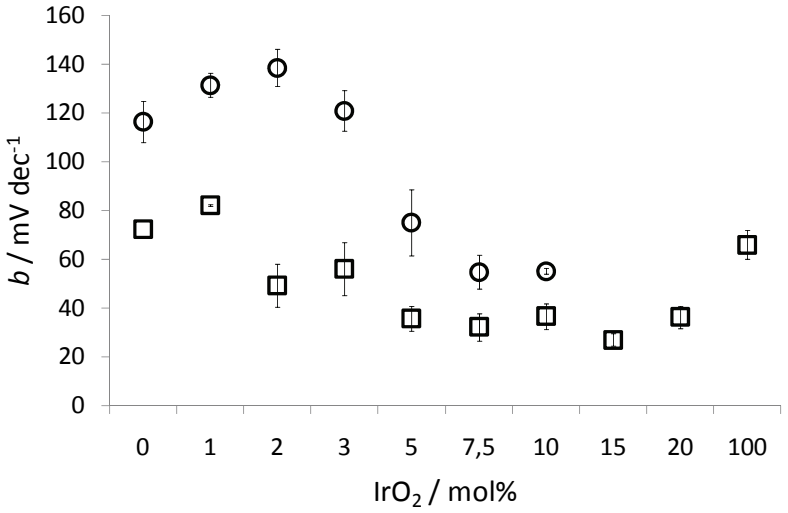

Figure 3.12 Tafel slope for H_2 evolution in the backward scan for IrO_2+Co_3O_4 electrodes as a function of composition. (○) High current density and (□) low current density.

3.3.6 Reaction order

The electrodes have then been subjected to further H_2 evolution in order to determine the reaction order, β_{H+}. The reaction order was derived from plots of (log j) at -1.15 V (SCE) *vs.* pH. The value of potential was selected so as to lie on the linear section of the polarization curves. The trend is for a negative reaction order which is less than unity. Reaction order is higher for the electrodes with lower content of IrO_2, it approaches 0 for electrodes with more than 5 mol% IrO_2. Since the reaction order was determined in the high overpotentials range, a value of zero can be plausible if a coverage, θ, close to 1 can be assumed.

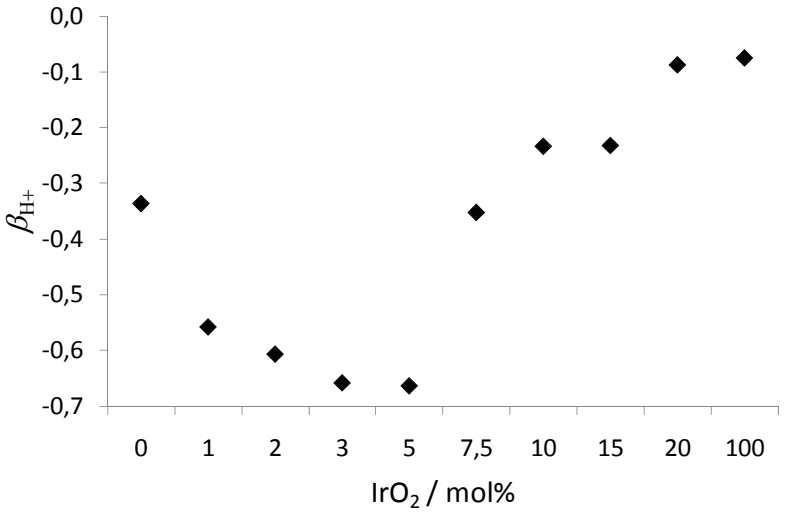

Figure 3.13 Order of reaction with respect to H^+ for H_2 evolution from NaOH + $NaClO_4$ solutions at variable H^+ concentration and constant ionic strength.

3.4 Discussion

3.4.1 Reaction mechanism

On the basis of Tafel parameter, *b*, a reaction mechanism can be proposed. The generally accepted mechanism for H_2 evolution has been discussed in Chapter 2 and is reported here:

$$M + H^+ + e \rightarrow H_{ads} \tag{3.6}$$

$$MH_{ads} + H^+ + e \rightarrow M + H_2 \tag{3.7}$$

$$MH_{ads} + MH_{ads} \rightarrow 2M + H_2 \tag{3.8}$$

The 60 mV Tafel slope observed on electrodes of pure Co_3O_4 and pure IrO_2 indicates that the rate-determining step is a chemical reaction following the primary discharge of water molecules on the oxide surface (EC mechanism).

On electrode with IrO_2 content in the range between 5 and 20 mol%, the 40 mV Tafel slope in the backward scan suggests that the second electron transfer is rate determining (EE mechanism). The Tafel slope close to 120 mV at higher current densities for some electrodes is probably related to a shift of the rate-determining step from the step (3.6) to the primary discharge (3.7). This is quite often observed in hydrogen electrocatalysis mechanism [12].

A Tafel slope very close to 30 mV was observed for the electrodes with 15 mol% IrO_2. This value suggests that this composition is very active. The electrode material binds the intermediate strongly and the step (3.8) is rate determining.

3.4.2 Electrocatalytic activity

The introduction of small amounts of IrO_2 in the Co_3O_4 matrix modifies the electrocatalytic properties as well as the H_2 evolution mechanism. In Figure 3.14 the overpotential at 50 mA cm^{-2} is plotted as a function of the IrO_2 content. There is a great decrease in overpotential, as IrO_2 content is increased from 0 to 5 mol%. At higher IrO_2 contents, the overpotential is almost constant. As already shown in Figure 3.10, the overpotential for pure IrO_2 is very high. A possible explanation may be the low surface area of 100% IrO_2 electrode, as measured by voltammetric curves after polarization experiments. Furthermore, synergetic effects are likely to be operating, because Tafel slopes obtained for mixed IrO_2+Co_3O_4 are lower than for pure IrO_2.

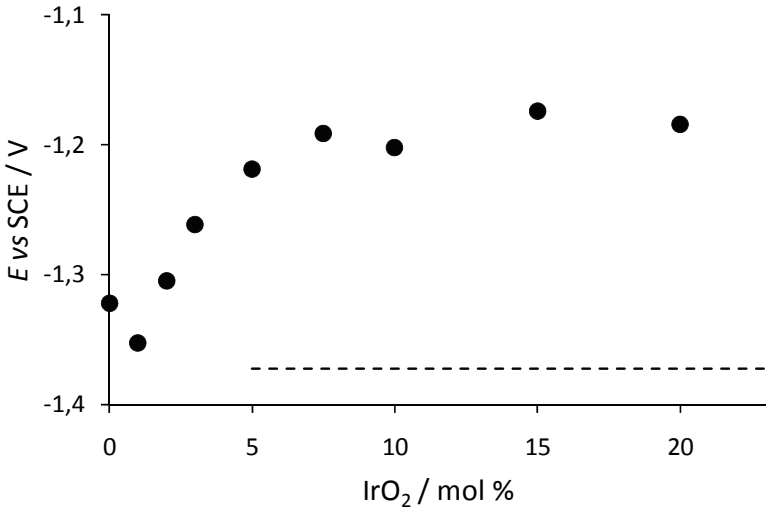

Figure 3.14 Overpotential for H_2 evolution at j = -50 mA cm^{-2} as a function of composition. The value for 100 mol% IrO_2 is indicated (---).

In Figure 3.15, the apparent current density recorded during the determination of reaction order is plotted as a function of nominal composition. The current increases as the IrO_2 content increase up to 5 mol%, and then it slightly decreases and settles to quite constant values for higher IrO_2 content. Looking at this graph only, it appears that electrodes with 5 mol% IrO_2 are the more active towards the reaction of H_2 evolution (HER).

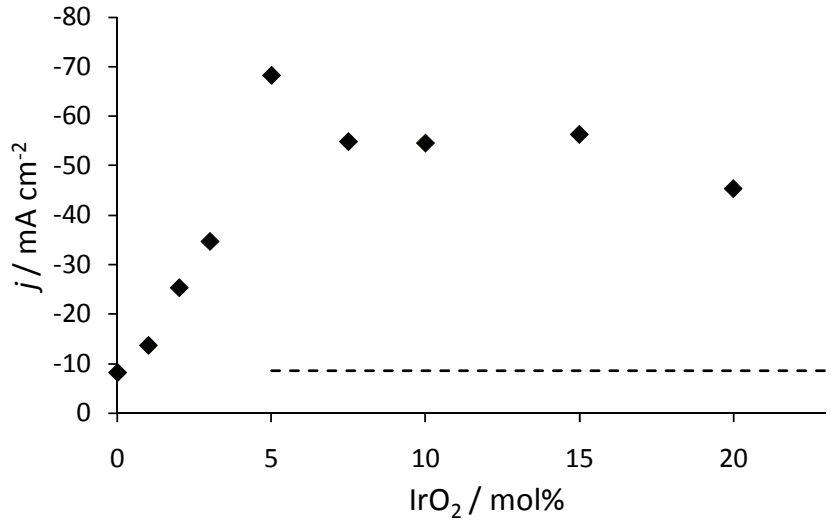

Figure 3.15 Apparent current density for H_2 evolution at -1.15 V(SCE) on IrO_2+Co_3O_4 electrodes as a function of nominal composition. The current was the one taken during the determination of reaction order. The value for 100 mol% IrO_2 is indicated (---).

Though a separation of electronic effect from geometric ones could be in principle attempted, this is not possible in the present work. The voltammetric charge is considered as a measure of electrochemically active surface area and it is usually used to normalize the current density, which is a measure of reaction rate. After H_2 evolution the charge was greatly enhanced as a consequence of Co_3O_4 reduction [1]. This charge is related to electrochemically active surface sites and includes also redox transition in the bulk of Co_3O_4. However, H_2 evolution occurs mostly on Ir sites, thus the voltammetric charge cannot be used to normalize the current density.

3.4.3 Effect of polarization and electrode stability

Cyclic voltammograms of the electrodes were recorded again after cathodic polarization, in order to monitor the state of the surface. The shapes of voltammograms as well as the voltammetric charges have to be taken into account. The evolution of CV curves after H_2 evolution is shown in Figure 3.16. Modifications are observed both in the shape and in the size. The pseudo-capacitive area is greatly enhanced, while the faradaic current related to the Co(III)/Co(IV) transition does not change appreciably. The shape after H_2 evolution gets closer to that of IrO_2.

As regards the voltammetric charge, Figure 3.17 shows the values of q^* obtained by integration of voltammetric curves after cathodic polarization. The trend is similar to the one recorded on fresh electrodes (Figure 3.5). The charge increases from 0 to 7.5 mol% IrO_2, than settles to an almost constant value. Comparison of voltammetric charge for the same electrode

before and after cathodic polarization experiments can provide some indication about whether the surface state has been affected or not. As shown in Figure 3.18, it is evident that there is a great increase in q^* after H_2 evolution. In Figure 3.19, q^* after polarization is compared with q^* after determination of reaction order. The electrode surface is not stable also after this further experiment. The charge increases again, with the exception of one composition (100 mol% IrO_2).

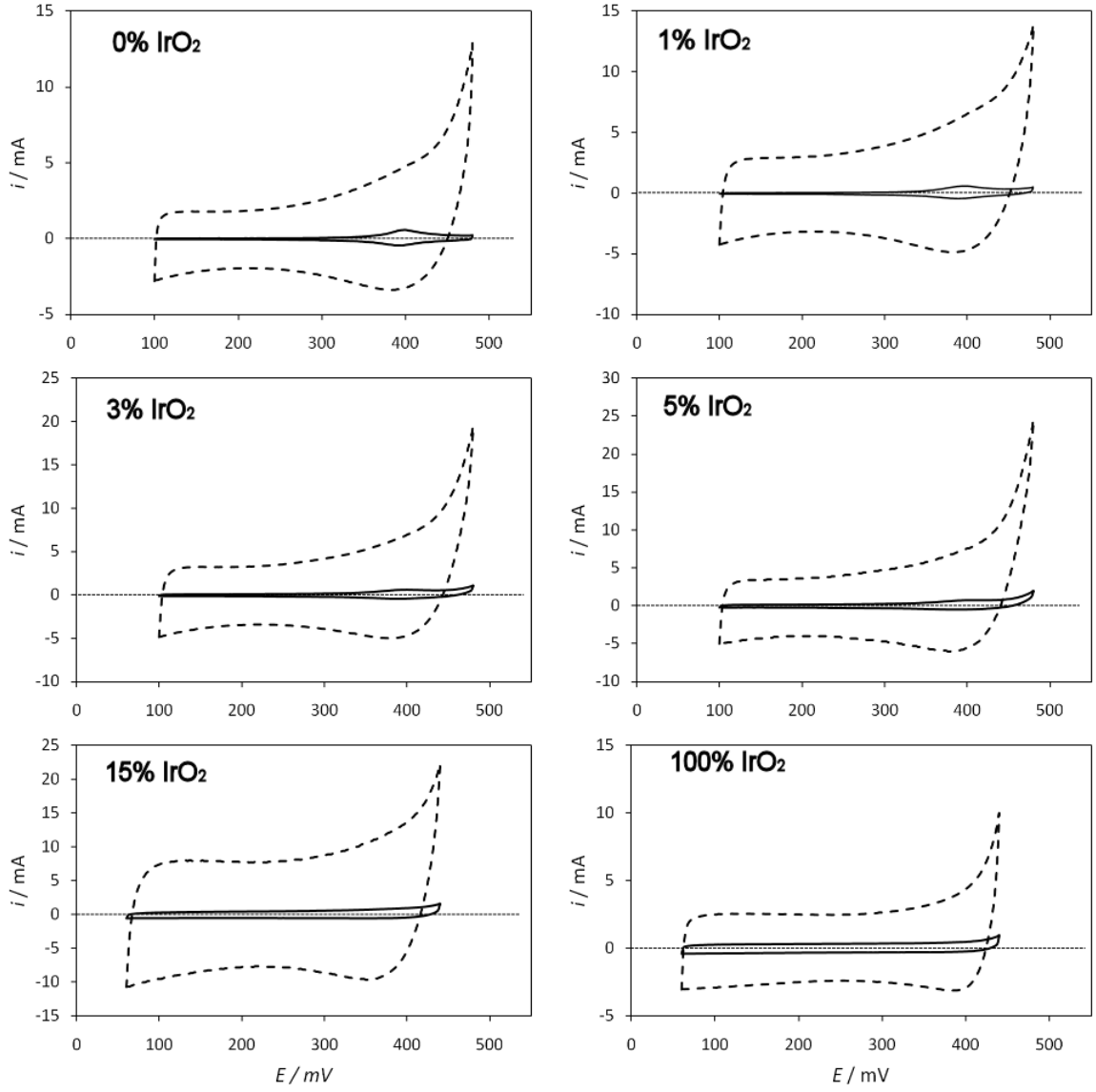

Figure 3.16 Comparison of voltammetric curves recorded before and after polarization experiments. (—) Fresh electrodes; (- - -) After cathodic polarization.

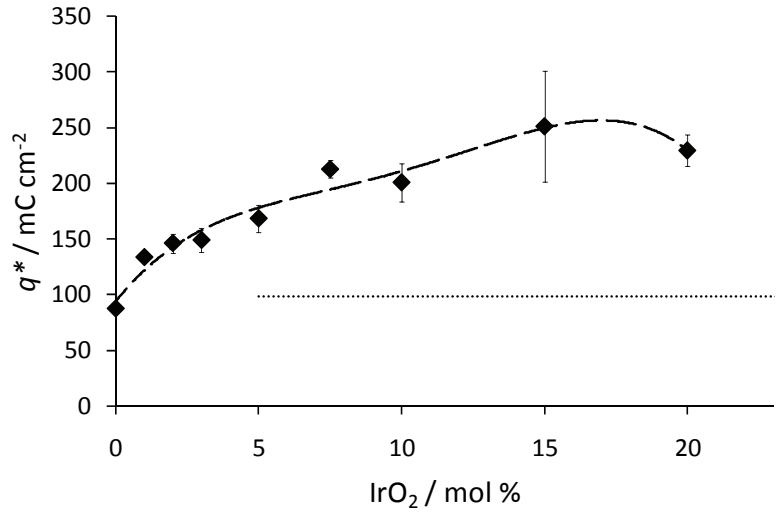

Figure 3.17 Surface charge q^* as a function of nominal composition of IrO_2+ Co_3O_4 oxide electrodes. q^* from integration of voltammetric curves recorded after polarization experiments. The value for 100 mol% IrO_2 is indicated (···).

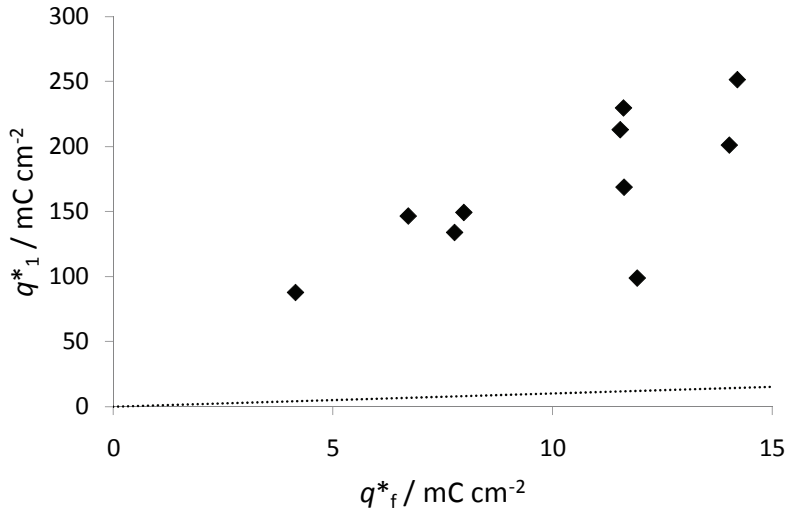

Figure 3.18 Voltammetric charge for fresh sample (q^*_f) plotted against voltammetric charge after cathodic polarization (q^*_1). (···) Straight line of unit slope.

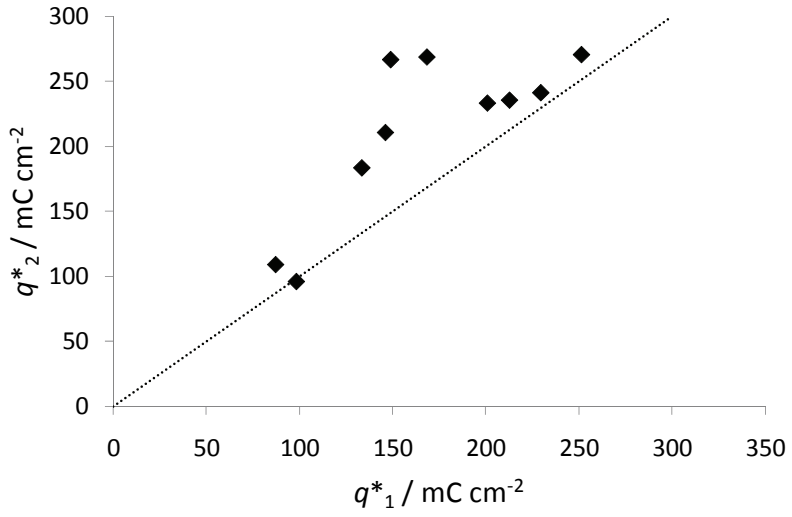

Figure 3.19 Voltammetric charge for electrode after cathodic polarization (q^*_1) plotted against voltammetric charge after determination of reaction order (q^*_2). (···) Straight line of unit slope.

An alternative representation of the same data is provided in Figure 3.20 and in Figure 3.21. Depending on IrO_2 content, charge increases up to 20 times after hydrogen evolution. Furthermore, the charge increases at a higher extent for electrodes with lower IrO_2 content. Since durability tests have not been carried out, a preliminary evaluation of the electrode stability can be done on the basis of data recorded after the determination of reaction order. It is evident that for electrodes with lower IrO_2 content, the charge increases again after prolonged cathodic load.

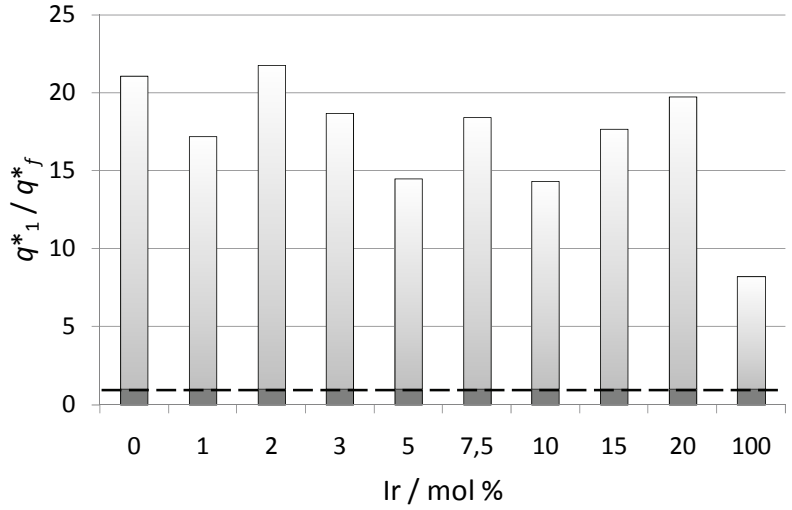

Figure 3.20 Ratio of voltammetric charge after and before H_2 evolution, as a function of composition.

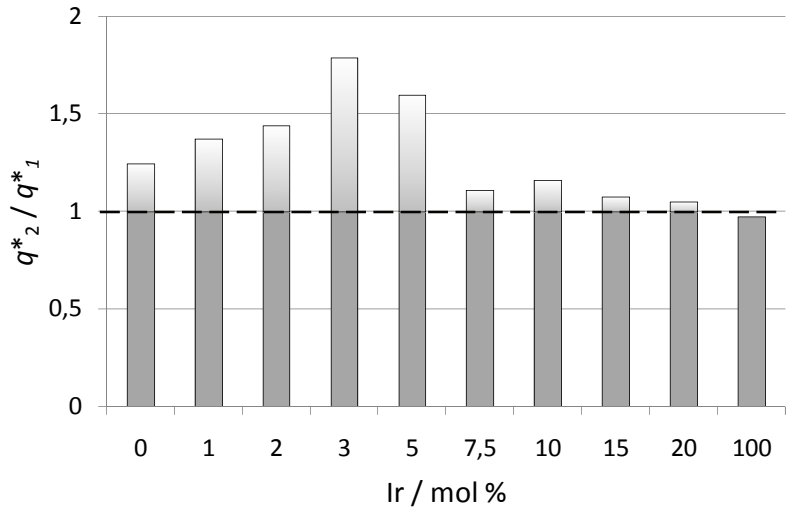

Figure 3.21 Ratio of voltammetric charge after and before the determination of reaction order, as a function of composition.

3.5 Conclusions

- IrO_2+Co_3O_4 mixed oxides produced by thermal decomposition exhibit a surface morphology and a voltammetric behaviour typical of Co_3O_4 up to 5 mol% IrO_2. Features more similar to pure IrO_2 appear for higher IrO_2 content. A phenomenon of surface enrichment in IrO_2 can be inferred, though XPS analysis data are not available. The voltammetric charge is proportional to surface active area and it increases with increasing IrO_2 content.
- Uncompensated ohmic resistances are lower than 1.0 Ω and slightly increase after massive hydrogen evolution as a consequence of the formation of Ir_2O_3. Tafel parameters are lower for mixed oxides than for the pure components. The same behaviour is observed looking at overpotential at high current densities. On the basis of Tafel slopes, two different steps can be considered rate determining, depending on the electrode surface composition.
- Electrodes at 15 mol% IrO_2 presents the lowest value of Tafel slope (about 30 mV). Furthermore, on this electrodes the overpotential is minimum. They also show a good stability, as shown by comparison of voltammetric charge before and after the determination of reaction order.
- As shown by the data for Tafel slopes and changes in surface area, electrodes exhibit activation after a short period of H_2 evolution.

3.6 References

[1] E. Veggetti, I.M. Kodintsev, S. Trasatti, Journal of Electroanalytical Chemistry 339 (1992) 255-268.

[2] N. Krstajic, S. Trasatti, Journal of The Electrochemical Society 142 (1995) 2675.

[3] N. Krstajic, S. Trasatti, Journal of Applied Electrochemistry 28 (1998) 1291-1297.

[4] I.M. Kodintsev, S. Trasatti, Electrochimica Acta 39 (1994) 1803-1808.

[5] L. Chen, D. Guay, A. Lasia, Journal of The Electrochemical Society 143 (1996) 3576-3584.

[6] R. Boggio, A. Carugati, G. Lodi, S. Trasatti, Journal of Applied Electrochemistry 14 (1985) 1561-349.

[7] S. Trasatti, in: J. Lipkowski, P.N. Ross (Eds.), The Electrochemistry of Novel Materials, VCH, New York, 1994.

[8] S. Trasatti, in: A. Wieckowski (Ed.), Interfacial Electrochemistry: Theory, Practice and Applications., Marcel Dekker, New York, 1999, pp. 769-792.

[9] R. Boggio, A. Carugati, S. Trasatti, Journal of Applied Electrochemistry 17 (1987) 828-840.

[10] H. Chen, S. Trasatti, Journal of Applied Electrochemistry 23 (1993) 559-566.

[11] L.D. Burke, D.P. Whelan, Journal of Electroanalytical Chemistry 124 (1981) 333-337.

[12] A. Anani, Z. Mao, S. Srinivasan, Journal of Applied Electrochemistry 21 (1991) 683-689.

Chapter 4. Thermal Ru-based oxides: modification by Ni oxide

4.1 Introduction

Doping would be one of the possible options to improve the material performance. It was reported that heterovalent substitution of Ru in RuO_2 structure with Fe [1], Co [2] and Ni [3] improved the electrocatalytic properties of the materials towards O_2 evolution reaction in acidic media. According to the authors, Ni substitution yields the most active electrocatalyst in that series. However, in our opinion, the stability of materials in acidic solution needs further investigation.

The present chapter deals with mixed RuO_2 and NiO_x oxides prepared on nickel and titanium substrates in order to evaluate their electrocatalytic properties for H_2 evolution reaction. Possibilities of application of such oxides have been already investigated in literature in the field of electrochemical supercapacitors [1,2].

Ni is the most used electrode material for cathodes in alkaline solutions [6]. Although its electrocatalytic activity is not excellent, the metal is resistant to corrosion at high pH values. There are, however, important problems of electrocatalytic stability. As a matter of fact, Ni exhibits a Tafel slope for H_2 evolution close to 120mV and the overpotential is not stable with time, especially in conditions of intermittent electrolysis as in the case of electrolyzers driven by solar energy conversion [7]. To overcome these problems, a lot of research work has been addressed to the preparation of activated Ni cathodes [8-12]. Activation of Ni has been the subject of previous work from our laboratories. Activation was performed by depositing thin layers of electroactive oxide, mainly RuO_2, either by direct thermal decomposition [13], or by electrodeposition of preformed RuO_2 particles from a Ni plating bath [14]. In both cases activation is excellent, but residual difficulties are still present. In the case of thermal decomposition in particular, the mechanical stability of the overlayer can lead to loss of material by erosion due to the evolving gas.

RuO_2 has been shown to possess interesting electrocatalytic properties both in acid [15] and in alkaline solutions [16]. However, the anchorage to a Ni support is not as excellent as on Ti, thus loss of material by mechanical erosion often occurs. On the other hand, Ti is

unsuitable in the strong alkaline media used in conventional electrolysis, for it undergoes passivation.

RuO_2+NiO_x mixed oxides supported on Ti as well as on Ni were prepared with different composition and their electrochemical and electrocatalytic properties towards H_2 evolution reaction were investigated both in acidic and alkaline solutions. In the following, the results obtained for Ti-supported and Ni-supported electrodes are presented separately. Some general conclusions will be drawn at the end of the present chapter.

4.2 Experimental

4.2.1 Electrodes

Ti/(RuO_2+NiO_x) and Ni/(RuO_2+NiO_x) electrodes were obtained by thermal decomposition of 0.1 mol dm^{-3} mixtures of ruthenium(III)-nitrosylnitrate, $RuNO(NO_3)_3$ and nickel nitrate, $Ni(NO_3)_2 \times 6H_2O$ in appropriate proportions.

$RuNO(NO_3)_3$ (Alfa Aesar) and $Ni(NO_3)_2 \times 6H_2O$ (Aldrich) were dissolved in deionized water (Millipore). Solutions were then deposited onto both faces of the support by brushing and calcinated in a pre-heated oven in ambient atmosphere for 5 min at 450 °C. This procedure was repeated until a final oxide loading of 2 mg cm^{-2} was reached. A final annealing for 1 h at the same temperature was performed.

Two series of electrodes were prepared, differing only in the metal substrate: Ti for the first series and Ni for the second one. Electrodes were prepared at different compositions, as reported in Table 4.1. For both series, three samples were produced at each composition for electrochemical characterization. An additional fourth sample was prepared on Ti and used for SEM analysis.

4.2.2 Support

Ti and Ni platelets (10 × 10 × 0.2 mm) with a thin stem on one side were used as a support. Just before the oxide deposition, Ti supports were sandblasted with quartz powder and then chemically etched for 1 h in boiling 10 w% oxalic acid.

Ni supports were sandblasted with quartz powder and degreased with acetone before the deposition of the precursors.

A thin Cu wire was welded to the Ti and Ni stem to ensure electrical connection. Electrodes were mounted in a Pyrex® tube. The geometric surface area exposed was 1 cm^2 on each of the two sides of the platelets.

Electrodes	RuO_2 / mol%	NiO_x / mol%
1	0.5	99.5
2	1	99
3	2	98
4	4	96
5	5	95
6	6	94
7	8	92
8	10	90
9	15	85
10	20	80
11	25	75
12	30	70
13	35	65
14	40	60
15	45	50
16	50	50
17	55	45
18	60	40
19	65	35
20	70	30
21	75	25
22	80	20
23	85	15
24	90	10
25	92	8
26	94	6
27	95	5
28	96	4
29	98	2
30	99	1
31	99.5	0.5
32	100	0

Table 4.1 Nominal composition of the prepared mixed oxides.

4.2.3 Methods

The morphology of the oxide layer was observed on a LEO 1430 scanning electron microscope (SEM).

Electrochemical characterization was carried out by cyclic voltammetry (CV) and quasi-steady state polarization curves. Experiments were performed in 0.5 mol dm^{-3} $HClO_4$ (Aldrich, 70%) and 1 mol dm^{-3} NaOH (Fluka, 98%) aqueous solutions, respectively for Ti/(RuO_2+NiO_x) and Ni/(RuO_2+NiO_x) electrodes. Solutions were kept at 25±0.1°C in a water thermostat and were deaerated before and during each experiment using nitrogen gas. Experiments were carried out using an EG&G Model 273A potentiostat/galvanostat connected to a personal computer. Measures were carried out in a cell with four separated compartments. Two Pt wires were used as counterelectrodes. The compartment of the

reference electrode was connected to the surface of the working electrode via a Luggin capillary. Potentials were read and are reported against a satured calomel electrode (SCE).

Voltammetric curves were recorded at 20 mV s^{-1}. Quasi-steady state polarization curves were obtained by keeping the electrode at open circuit potential (OCP) for 15 min, then at the potential of incipient H_2 evolution for 5 min (-1.0 V(SCE) for Ti series and -1.1 V(SCE) for Ni series). The electrode potential was then moved by 10 mV steps and the current read after 1 min at each potential (forward scan). As the current reached about -100 mA, the direction of potential variation was reversed until the current became anodic (backward scan).

4.3 Ti/(RuO_2+NiO_x) electrodes

4.3.1 Surface morphology

SEM images of Ti/(RuO_2+NiO_x) electrode are reported in Figure 4.1 (5000×) and Figure 4.2 (30000x). At lower magnification, not shown here, electrodes looks uniformly covered by the oxide layer and the effects of support pretreatment are not visible. The morphology is very different for different compositions. At lower RuO_2 content, the amorphous layer is mostly constituted by NiO_x. Some globular particles, mainly constituted by RuO_2, are uniformly distributed in the NiO_x matrix. As the RuO_2 content increases, the number of these particles increases and the shape is more defined. At higher RuO_2 content, SEM images reveal a cracked surface, which is typical of thermally prepared RuO_2 oxide [17].

A further magnification of the particles pointed out that they are aggregates of smaller and well defined geometric structures, whose size is lower than 1 μm. From images for electrodes at 80 and 100 mol% (Figure 4.2 (d), (e), (f)), it is clearly visible that these structures grow preferentially in the defective regions of the oxide layer below.

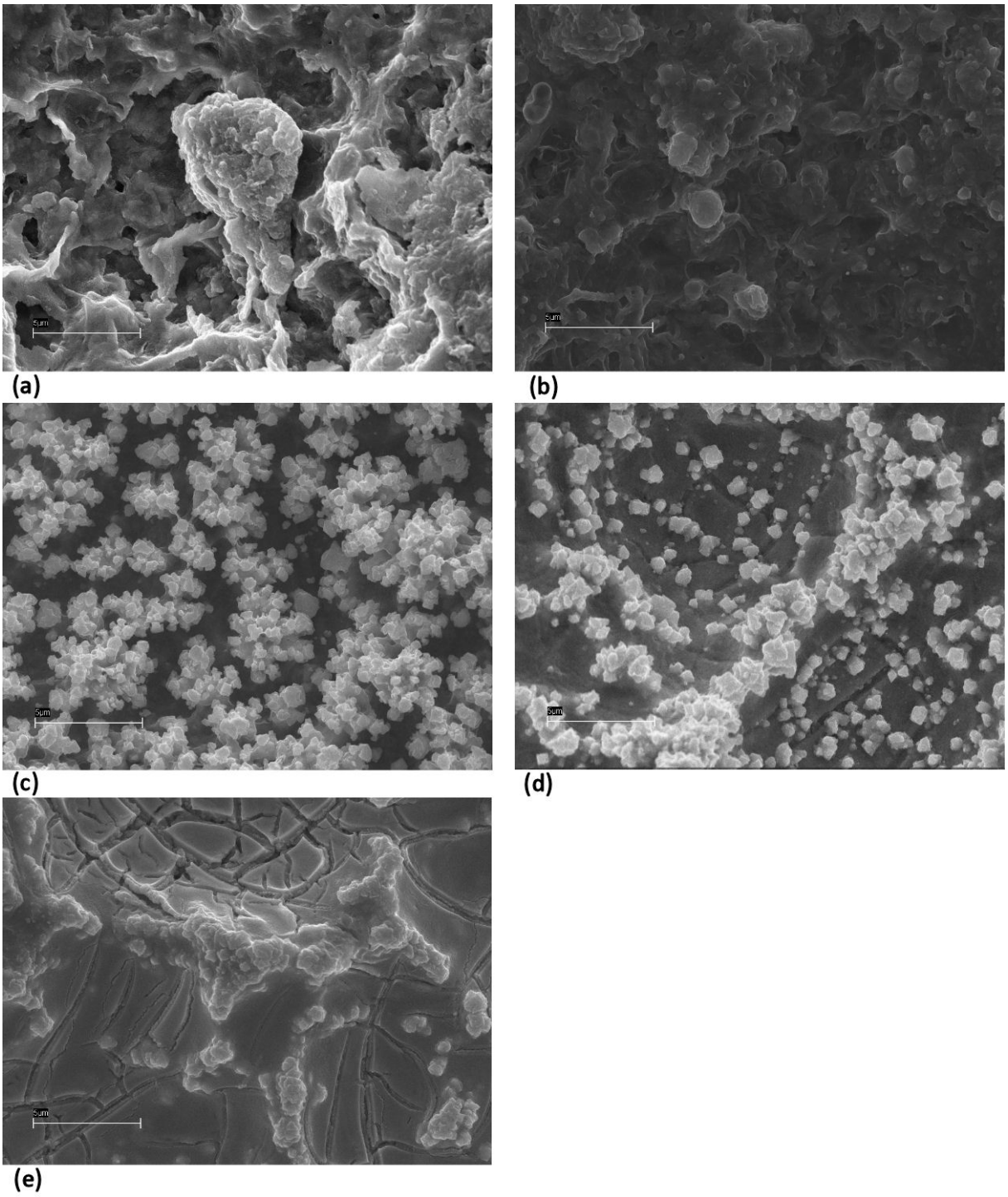

Figure 4.1 SEM micrographs (5000 ×) of fresh samples of RuO_2+NiO_x at different contents of RuO_2. (a) 0.5; (b) 10; (c) 50; (d) 80; (e) 100 mol% RuO_2. The marker is 5 μm.

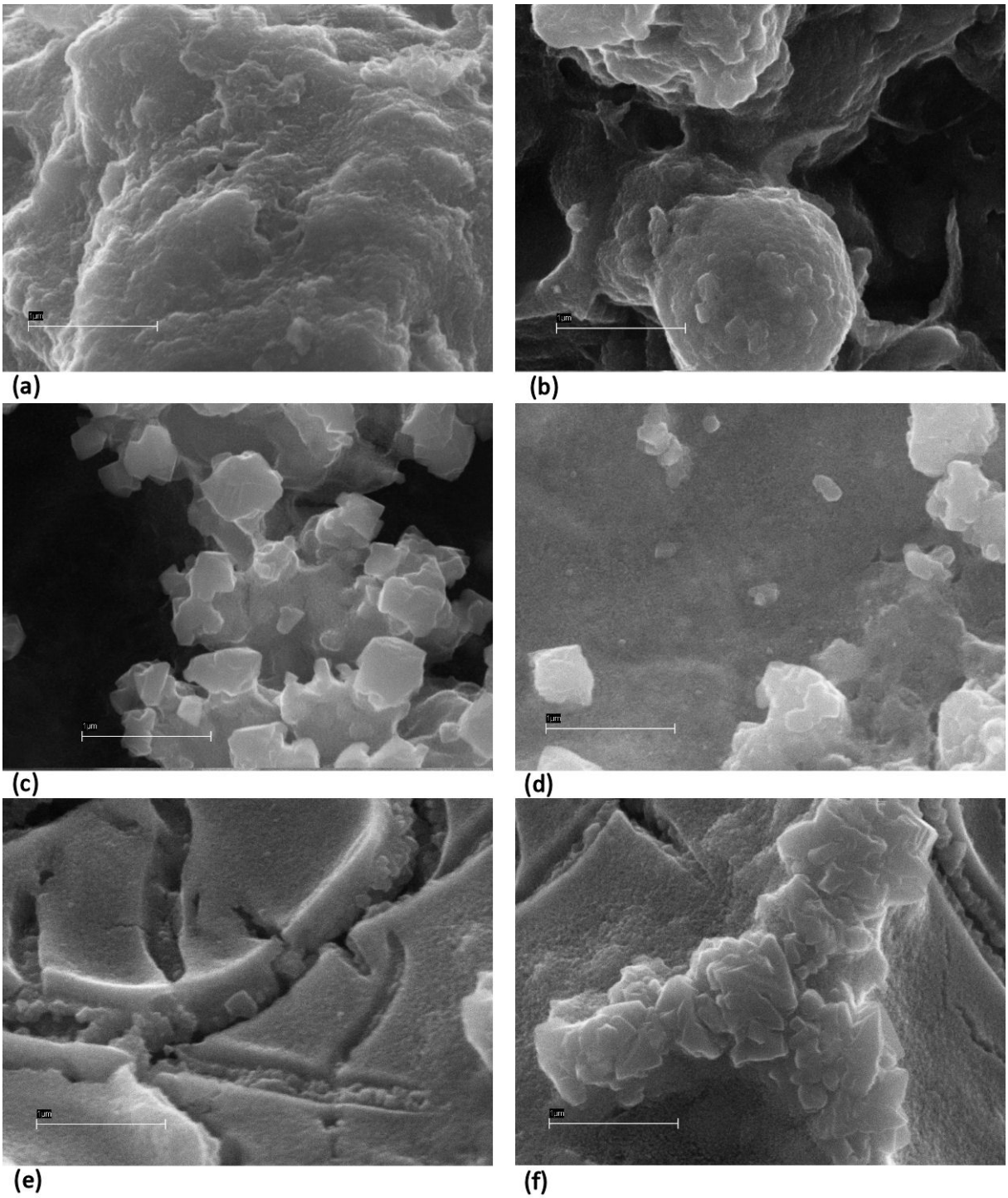

Figure 4.2 SEM micrographs (30000 ×) of fresh samples of RuO_2+NiO_x at different contents of RuO_2. (a) 0.5; (b) 10; (c) 50; (d) 80; (e) and (f) 100 mol% RuO_2. The marker is 1 μm.

4.3.2 Voltammetric curves

Voltammetric behaviour of fresh Ti/(RuO_2+NiO_x) electrodes was investigated by cyclic voltammetry (CV). Voltammetric curves can be regarded as electrochemical spectra. They constitute the electrochemical fingerprint of a given compound and can give information on surface morphology [17].

Figure 4.3 shows voltammetric curve in the range between -0.3 and 1.1 V(SCE) for some composition.

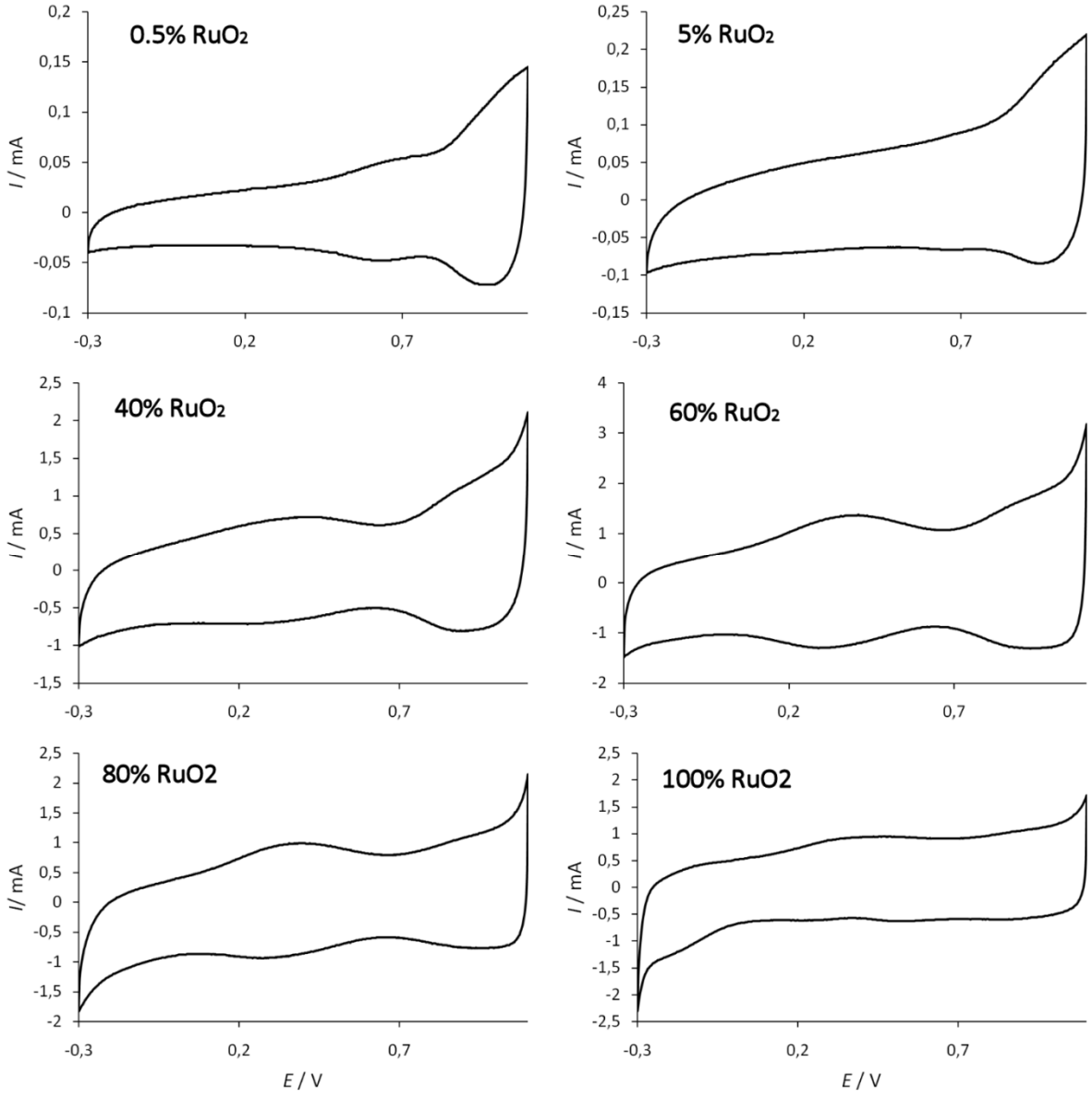

Figure 4.3 Voltammetric curves at 20 mV s^{-1} in 0.5 mol dm^{-1} $HClO_4$ solution of Ti/(RuO_2+NiO_x) mixed oxides.

No Ni(II)/Ni(III) redox peaks are evident from voltammetric curves, even at lower RuO_2 content. A similar behaviour was already reported in literature for nickel oxide

electrodes tested by CV in acidic media [18], although others studies on single crystals of NiO in H_2SO_4 have been reported to exhibit Ni(II)/Ni(III) redox peaks [19]. Since electrochemical characterization is performed in acidic solution, the absence of Ni(II)/Ni(III) redox peaks can be also attributed to NiO_x dissolution.

For electrodes with higher RuO_2 content, the features of the curves are consistent with a poorly crystalline nature of this oxide. The curves are broad and exhibit pseudo-capacitive behaviour, consistent with the electrochemical mechanism expected for the RuO_2 film [20]. RuO_2 surface sites are reversibly oxidized and reduced with the simultaneous exchange of protons with the electrolytic solutions, according to the following reaction:

$$\mathrm{RuO}_x(\mathrm{OH})_y + \delta \mathrm{H}^+ + \delta e \rightleftarrows \mathrm{RuO}_{x-\delta}(\mathrm{OH})_{y+\delta} \tag{4.1}$$

As a consequence of such electrochemical reactions, voltammograms voltammetric curves recorded for the hydrous surface of RuO_2 in aqueous electrolyte between H_2 and O_2 evolution potentials are capacitive and nearly featureless [21].

Figure 4.4 shows the effect of composition on the current of starting H_2 evolution reaction. The current is very negligible for electrodes with less than 15 mol% RuO_2. The highest current value is for the electrode at 60 mol% RuO_2. It is interesting that the currents of starting H_2 evolution decrease slightly as the RuO_2 content increases further.

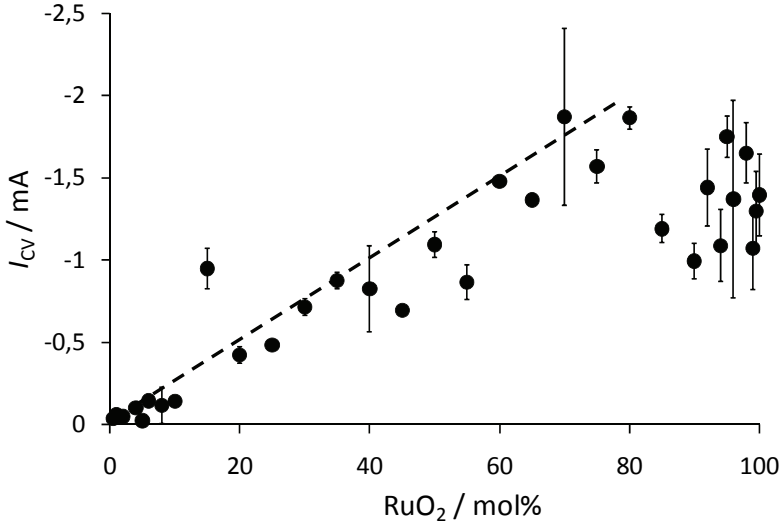

Figure 4.4 Current of starting H_2 evolution (at -0.3 V (SCE) from voltammetric curves).

A similar pattern is observed in Figure 4.5, which shows the dependence of voltammetric charge on RuO_2 content. The voltammetric charge, q^*, is obtained by integration of voltammetric curves. q^* is related to surface redox transitions and can be taken as a measure of electrochemically active surface sites [22]. The charge increases almost linearly up to 60 mol% RuO_2, and then decreases slightly. Data are more scattered for

electrodes at higher RuO_2 content. Electrodes with RuO_2 content close to 40 mol% exhibit charge values similar to pure RuO_2.

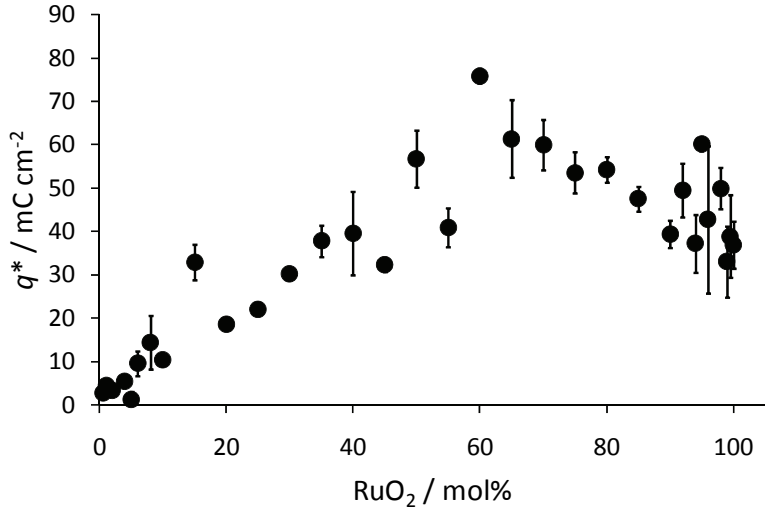

Figure 4.5 Voltammetric charge, *q, by integration of voltammetric curves on fresh electrodes as a function of composition.**

4.3.3 Polarization curves and Tafel slopes

Figure 4.6 shows quasi-stationary polarization curves for H_2 evolution from 0.5 mol dm^{-3} $HClO_4$ solution. A marked hysteresis was observed between the forward and the backward potential scan for all the electrodes. A linear portion of the curve (Tafel line) was identified both in forward and backward scans. Deviations from linearity at high current densities were attributed to uncompensated ohmic drops in the forward scan. When the backward scan is considered, deviations were found to imply also a change in Tafel slope.

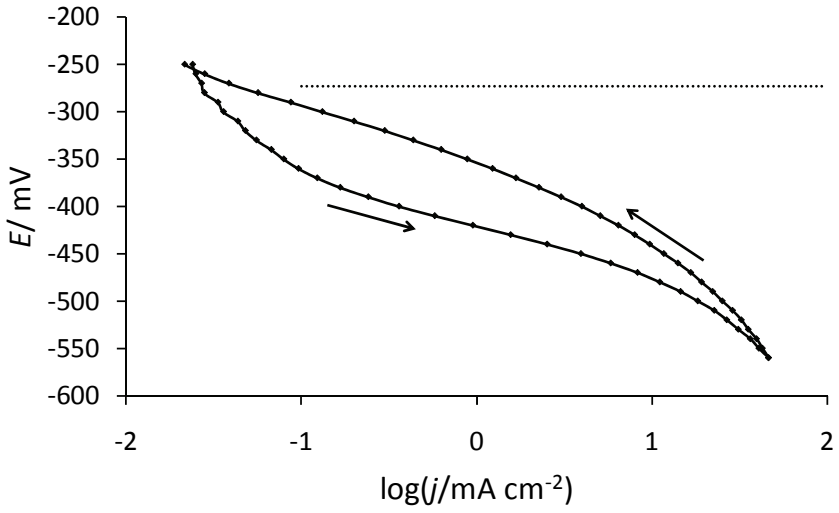

Figure 4.6 Polarization curve for H_2 evolution from 0.5 mol dm^{-3} HClO4 on a RuO_2+NiO_x electrode with 40 mol% RuO_2. Arrows indicate the direction of potential variation. The reversible potential for H2 reaction is indicated (···).

Kinetic parameters were obtained by polarization curves using two different methods. In the *IR* compensation approach a Tafel line is drawn in the linear section of the curve in the low current density range. Deviations of experimental points from the Tafel straight line are plotted against the current *I*. The plot results in a straight line, whose slope is the uncompensated ohmic resistance, *R*. In the derivative method, uncompensated ohmic drops are included into the Tafel equation:

$$E = a + b \log j + RI \tag{4.2}$$

The uncompensated resistance and the Tafel slope are obtained, respectively, as the intercept and the slope of a plot $\Delta E/\Delta j$ *vs*. $1/j$.

It is important to evaluate the ohmic drops, because they are related to the state of the support/active layer interface. Figure 4.7 shows the average uncompensated ohmic resistance as a function of RuO_2 content. Reported values are the average between *IR* compensation method and derivative method.

For electrodes with more than 10 mol% RuO_2, ohmic resistances values are between 0.5 and 1.0 Ω and can be attributed only to the solution resistance between the electrode surface and the Luggin capillary. Very high resistance values for electrodes with lower RuO_2 content are probably due to the resistivity of the oxide layer, which is mainly constituted by NiO_x.

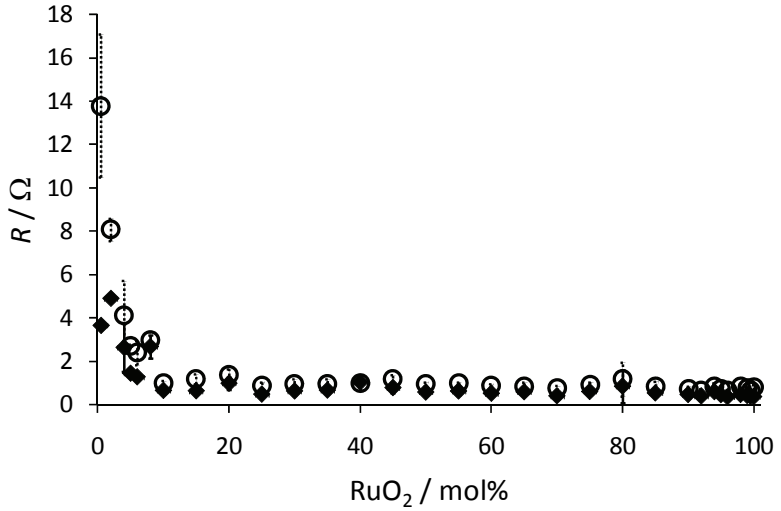

Figure 4.7 Uncompensated ohmic resistance in 0.5 mol dm^{-3} $HClO_4$ solution for Ti/(RuO_2+NiO_x) electrodes as a function of composition. (◆) Forward and (○) backward potential scan. Data from both derivative method and *IR* compensation method are included.

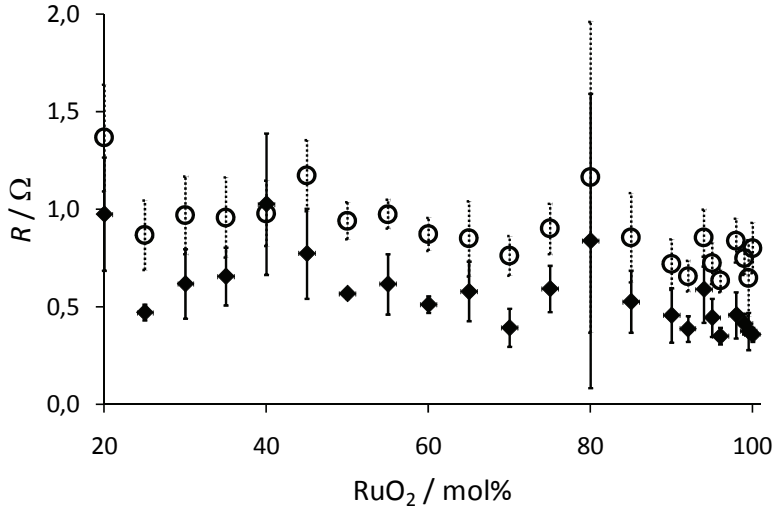

Figure 4.8 Uncompensated ohmic resistances for Ti/(RuO_2+NiO_x) electrodes with RuO_2 content >20 mol%. (◆) Forward and (○) backward polarization scan.

Figure 4.9 shows the dependence of Tafel slope, *b*, from the RuO_2 content. The value of Tafel slope is close to 120 mV for electrodes with less than 10 mol% RuO_2. As the RuO_2 content exceeds 10 mol%, the Tafel slope varies in the range between 41 and 64 mV, both in the forward and in the backward polarization scan. Values of Tafel slope are slightly higher in the backward polarization. This means that H_2 evolution reaction does not result in electrode activation.

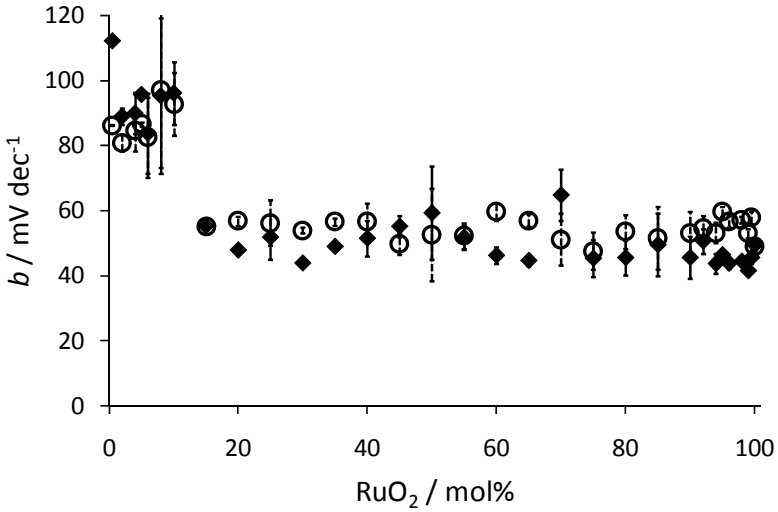

Figure 4.9 Tafel slope for H_2 evolution at low current density from 0.5 mol dm^{-3} $HClO_4$ solution on Ti/(RuO_2+NiO_x) electrodes as a function of composition. (◆) Forward and (○) backward potential scan.

In the backward scan, polarization curves exhibit two Tafel slopes (Figure 4.10). A second Tafel slope can indicate a variation in the reaction mechanism or a change in the rate

determining step for the same mechanism. The two Tafel slope for electrodes with more than 10 mol% RuO_2 are reported in Figure 4.10.

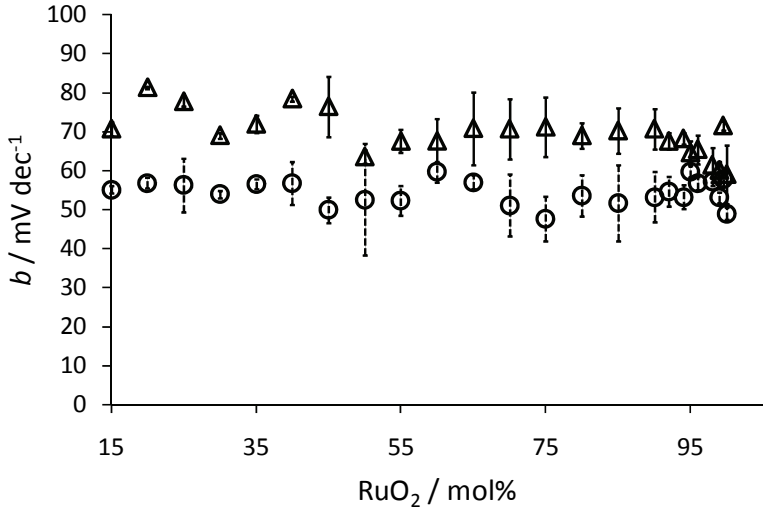

Figure 4.10 Tafel slope for H_2 evolution in the backward scan for Ti/(RuO_2+NiO_x) electrodes as a function of composition. (○) Low current density and (Δ) high current density.

4.3.4 Electrocatalytic activity

Electrocatalytic properties can be assessed only on a relative basis by comparing current at constant potential (Figure 4.11) or potential at constant current (Figure 4.14) [23]. Figure 4.11 shows the dependence of the current density, *j*, on the RuO_2 content at -430 mV. The value of potential is situated in the linear section of Tafel polarization curves.

Current density is a measure of electrocatalytic activity towards the given reaction. In this case the activity towards H_2 evolution varies in a way similar to the variation of voltammetric charge, q^*. This means that, at a first sight, the electrocatalytic activity appears to be proportional to the surface concentration of active sites and not to their nature. Activity is appreciable for electrodes with more than 20 mol% RuO_2 and reaches a maximum at around 65-75 mol% RuO_2. There is a great decrease in activity for higher compositions.

As a matter of fact, both electronic and geometric factors contribute to electrocatalytic activity. A first separation is achieved on the basis of Tafel slope, which is an intensive property not depending on surface area extent. Figure 4.12 shows the correlation between the activity, *j*, at E = -430 mV(SCE) and the corresponding voltammetric charge obtained after polarization experiments. The dependence on the charge is non linear and the increase is more than proportional with increasing q^*. This indicates that not only geometric effects are operating.

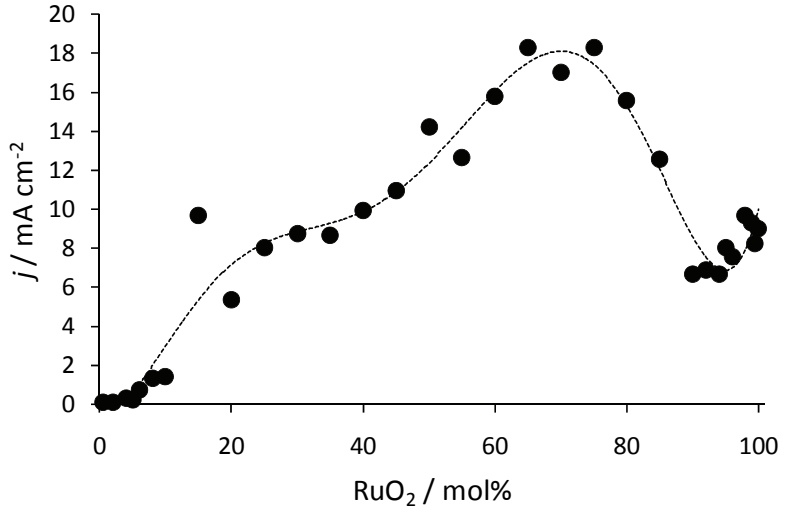

Figure 4.11 Current density of H_2 evolution at -430 mV(SCE) as a function of composition.

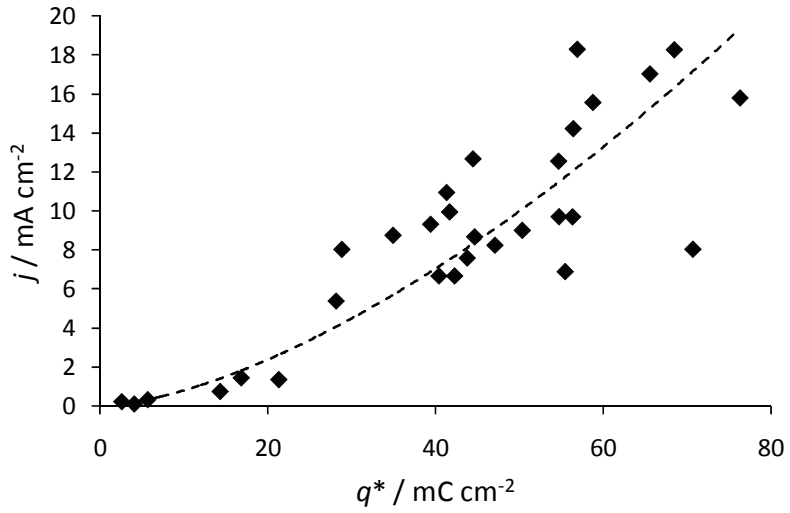

Figure 4.12 Current density of H_2 evolution at -430 mV(SCE) as a function of voltammetric charge obtained after cathodic polarization experiment.

Normalization of activity, *j*, to the unit surface area would allow for better separation of geometric and electronic factors. In heterogeneous catalysis the surface area is normally measured by the BET method. In this case thin layer of oxides are deposited on a substrate and the resulting area/volume ratio is usually too low for the technique to be applied properly. In addition, the surface area measured by BET method may not correspond to the true electrochemically active surface area [24]. The latter can be determined on a relative basis by integration of voltammetric charge, q^*. q^* measures the amount of protons exchanged per unit surface between the oxide surface and the solution. Proton exchanges occurs on surface active sites, thus q^* can be considered a measure of the electrochemically active surface area.

Since q^* measures the concentration of surface active sites, the ratio j/q^* is proportional to the electrocatalytic activity of a single active site. In Figure 4.13 the variation of j/q^* is plotted as a function of RuO_2 content. The activity greatly increases for RuO_2 content higher than 20 mol%. Electrodes with more than 85 mol% RuO_2 show lower activity than electrodes at intermediate compositions.

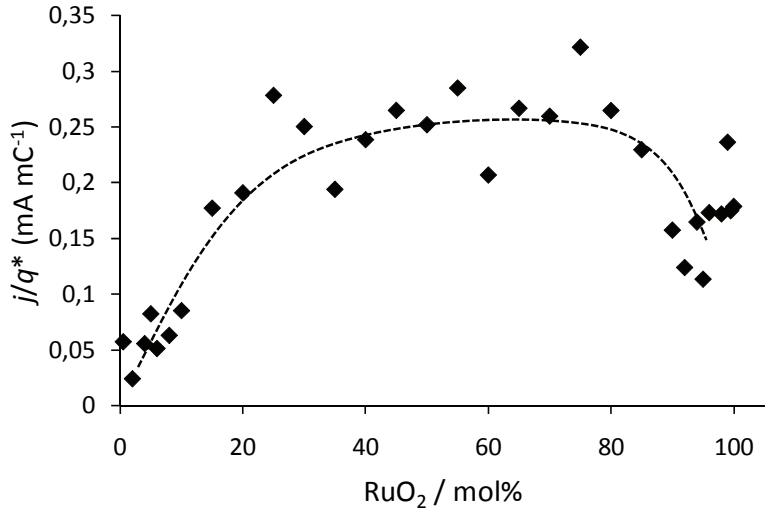

Figure 4.13 Current of H_2 evolution normalized to unit voltammetric charge as a function of electrode composition.

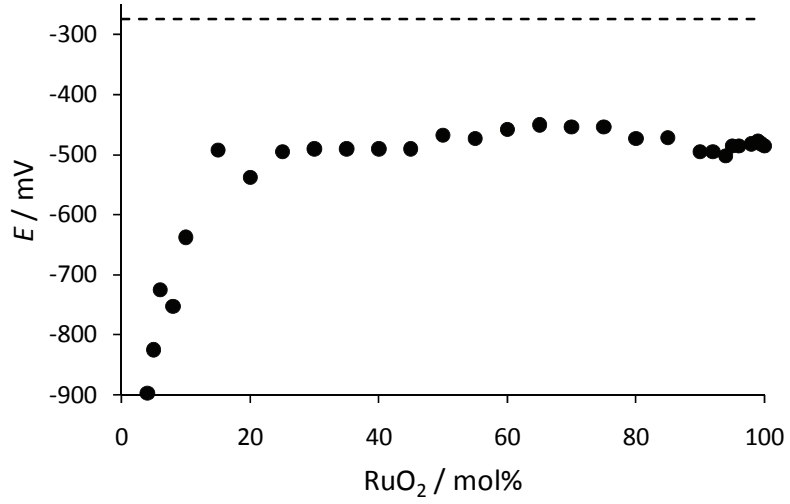

Figure 4.14 Overpotential for H_2 evolution in acidic solution at j = -50 mA as a function of composition. The reversible potential for H_2 reaction is indicated (···).

The dependence of the overpotential at j=-50 mA from the backward polarization curves is reported in Figure 4.14 as function of RuO_2. The overpotential exhibits a sharp decrease when RuO_2 content is increased from 10 to 15 mol%. At higher composition the

overpotential is almost constant. In more detail, the lowest value is observed for electrodes at 60-75 mol% RuO_2, and slightly increases when RuO_2 is further increased.

4.3.5 Stability

The electrode stability can be defined as the behaviour of the electrode potential with time in conditions of continuous H_2 evolution. Durability tests have not been carried out in this work. However, since stability implies also constancy of electrode surface properties, voltammetric curves were recorded again after steady-state polarization experiments and compared with voltammetric curves for fresh electrodes (Figure 4.15).

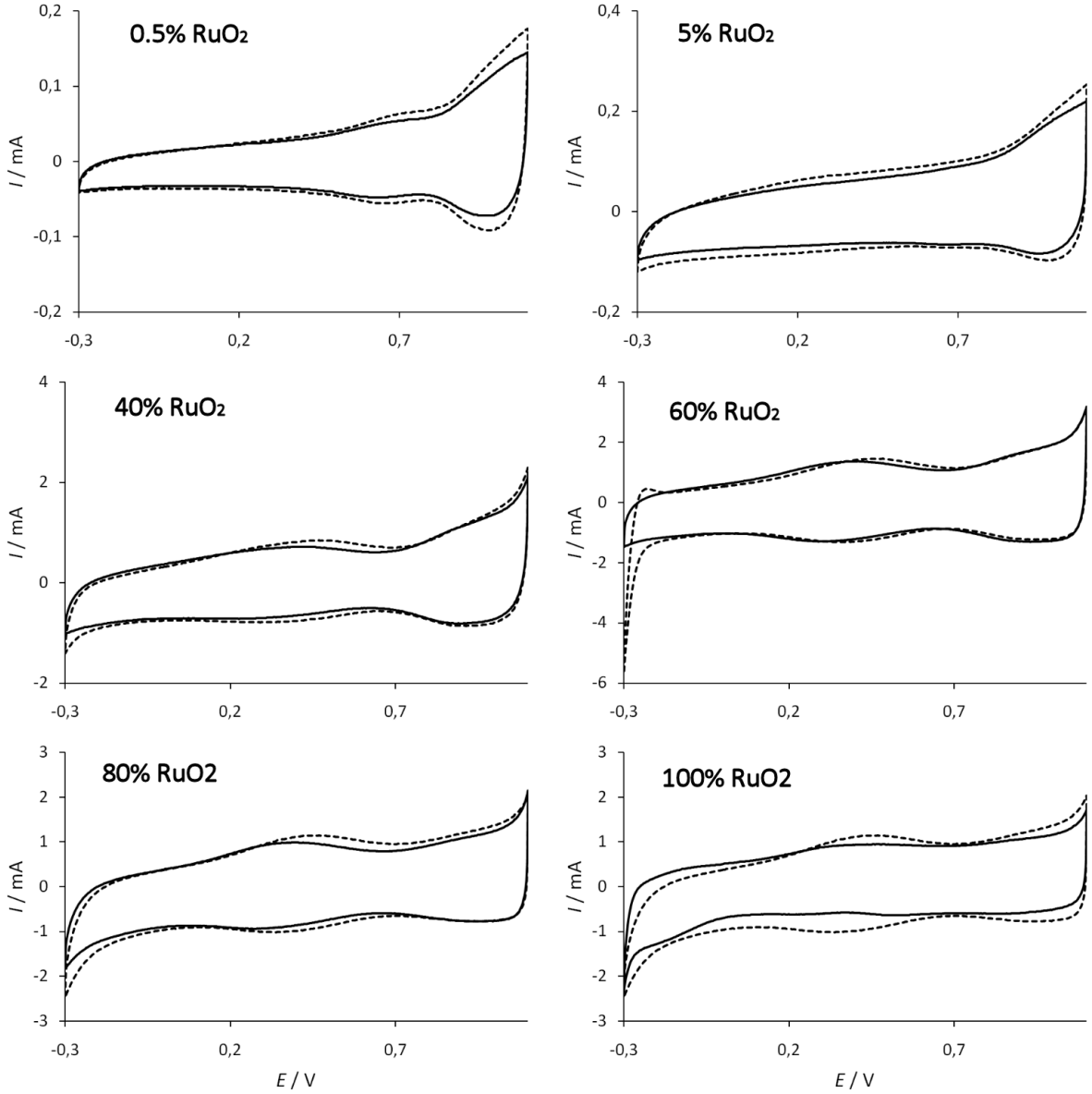

Figure 4.15 Voltammetric curves at 20 mV s^{-1} in 0.5 mol dm^{-1} $HClO_4$ solution of (RuO_2+NiO_x) mixed oxides after H_2 evolution. (—) Fresh electrodes; (- - -) After cathodic polarization.

The voltammetric charge, q^*, can help to check the surface state of an electrode after an experiment. Eventual variations in voltammetric charges after cathodic polarization reveal if the surface is stable towards the H_2 evolution reaction. Figure 4.16 shows the effect of composition on the voltammetric charge. q^* goes through a maximum at about 60 mol% RuO_2, then it decreases slightly. The trend is similar to the one observed on fresh electrodes (cf. Figure 4.5). However, if q^* after polarization is plotted against q^* for fresh electrodes, the active surface area appears to be enhanced for most electrodes (Figure 4.17).

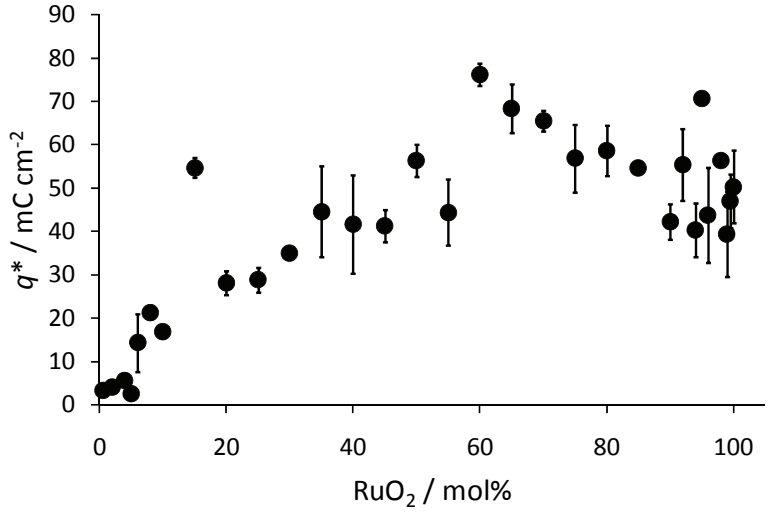

Figure 4.16 Voltammetric charge (q^*) from integration of voltammetric curves as a function of composition.

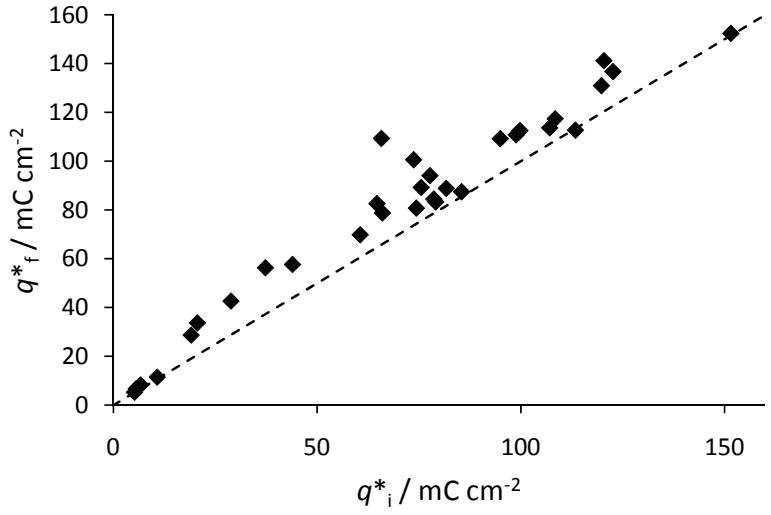

Figure 4.17 Voltammetric charge for fresh electrodes (q^*_i) *vs.* voltammetric charge after polarization (q^*_f). (- - -) Bisecting line

In Figure 4.18, the ratio (q^*_f/q^*_i) is reported for each electrode as a function of composition. An increase in q^* can be seen as an increase in the wetted oxide surface or can be due to surface roughening. The charge increases at a higher extent for electrode with lower

RuO_2 content. The charge increases at a lower extent in the composition range between 50 and 94 mol% RuO_2. An eventual loss of oxide material would result in a decrease in q^*.

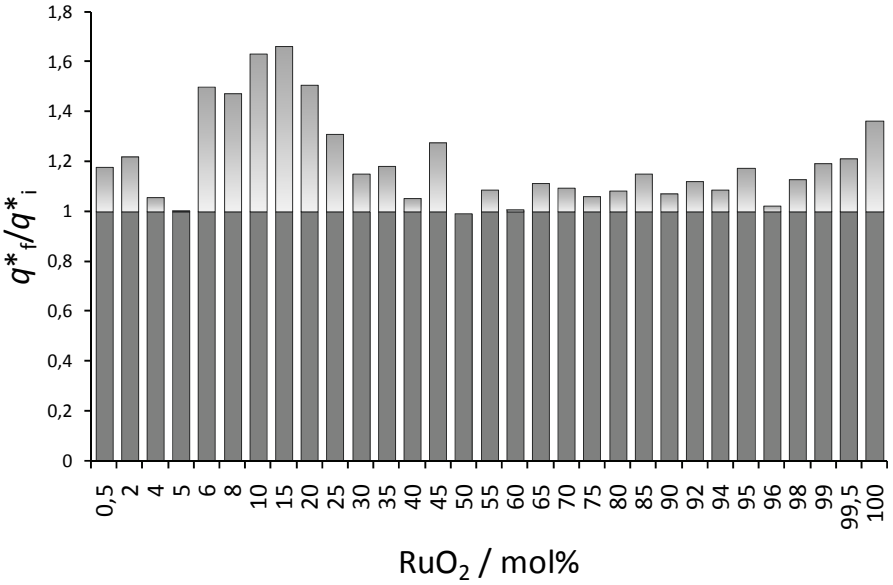

Figure 4.18 Ratio of voltammetric charge after (q^*_f) *vs.* before (q^*_i) H_2 evolution as a function of composition.

4.3.6 Conclusions

- RuO_2+NiO_x mixed oxide electrodes were prepared by thermal decomposition on Ti, in the composition range between 0.5 and 100 mol% RuO_2.
- Ti/(RuO_2+NiO_x) electrodes show a maximum in voltammetric charge at 60 mol% RuO_2.
- The highest apparent activity is observed for electrode with RuO_2 content between 60 and 80 mol%.
- Separation of electronic and geometric factors shows that electrodes at intermediate composition (20-80 mol% RuO_2) are more active towards H_2 evolution than pure RuO_2. The true electrocatalytic activity is maximum at 75 mol% RuO_2.
- Pseudo-capacitive region does not vary too much after cathodic polarization. Increase in surface area can be attributed to an increase in RuO_2 wetting.
- Electrodes with less than 20 mol% RuO_2 are not stable towards H_2 evolution reaction. Electrodes at intermediate composition (between 20 and 80 mol% RuO_2) exhibit similar kinetic parameters.
- Electrodes between 60 and 80 mol% exhibit better electrocatalytic performances than pure RuO_2.

4.4 Ni/(RuO_2+NiO_x) electrodes

4.4.1 Voltammetric curves

Electrochemical behaviour of fresh Ni/(RuO_2+NiO_x) electrodes was investigated by cyclic voltammetry in the potential range between -1.1 and 0.45 V(SCE). As for electrodes prepared on Ti, also in this case voltammetric curves were further recorded after steady-state polarization experiments, in order to evaluate eventual modifications of the surface.

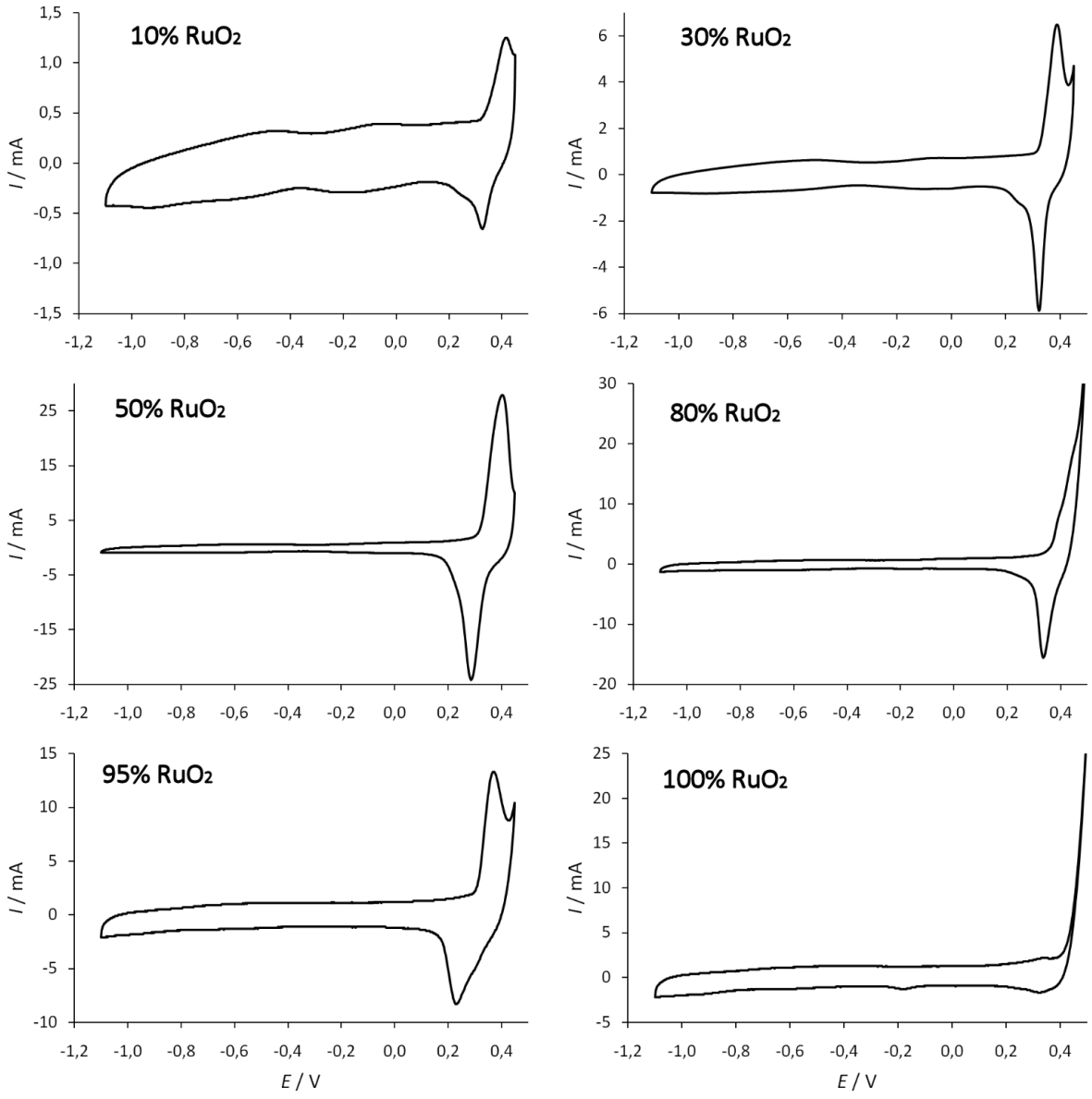

Figure 4.19 Voltammetric curves at 20 mV s^{-1} in 1.0 mol dm^{-1} NaOH solution of Ni/(RuO_2+NiO_x) electrodes.

The cyclic voltammograms show a pair of peaks, centered at ~0.3 V(SCE), which are characteristic of the Ni(II)/Ni(III) redox transition. The oxidation reaction of Ni(II) to Ni(III) is described by the following equation [25]:

$$Ni(OH)_2 + OH^- \rightleftarrows NiOOH + H_2O + e \quad (4.3)$$

The height of the peaks increases with increasing RuO_2 content. The peak typical of Ni(II)/Ni(III) redox transition is clearly visible also for the electrode of pure RuO_2. This is a clear indication that the Ni substrate interfere with the oxide active layer or is easily accessible to the solution. The large anodic current observed at potentials more positive than the Ni(II)/Ni(III) redox peaks correspond to the starting O_2 evolution reaction. The voltammetric curves in the potential range between -1.1 and 0.0 V(SCE) show pseudo-capacitive behaviour.

Voltammetric curves of Ni/(RuO_2+NiO_x) are qualitatively and quantitatively different from curves recorded for fresh Ti/(RuO_2+NiO_x). The potential range is approximately the same on the (NHE) potential scale. At lower RuO_2 content, the current in the capacitive region is higher for Ni/(RuO_2+NiO_x) electrodes. Considering this observation, a phenomenon of pseudo-capacitance attributable to NiO_x cannot be ruled out in alkaline environment. Ti/(RuO_2+NiO_x), on the other hand, were tested in $HClO_4$. In acidic environment pseudo-capacitance was not observed [18]. Furthermore, the Ni(II)/Ni(III) redox peaks are hardly identified for Ti/(RuO_2+NiO_x) electrodes, even when NiO_x is the main component.

Voltammetric charge was obtained by integration of voltammetric curves in the pseudo-capacitive region (between -0.8 and 0.0 V(SCE)). In this range of potential, the faradaic contributions due to Ni(II)/Ni(III) are excluded. Figure 4.20 shows the dependence of the voltammetric charge, q^*, on composition.

The charge is minimum for electrodes with lower RuO_2 content, then gradually increases and settles to an almost constant value for electrodes with 15-50 mol% RuO_2. For electrodes with more than 50 mol% RuO_2, q^* increases again, slightly decreases up to 90 mol% RuO_2 and then reaches the highest value for pure RuO_2.

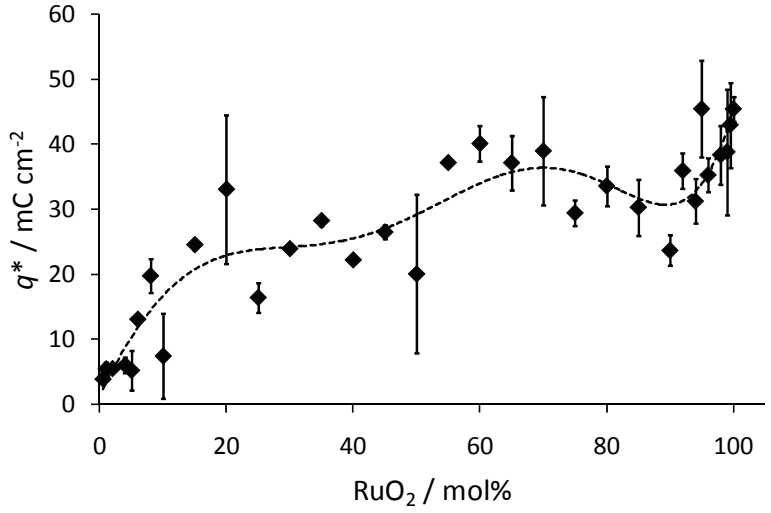

Figure 4.20 Voltammetric charge (*q) by integration of voltammetric curves as a function of composition.**

4.4.2 Polarization curves and Tafel slopes

Figure 4.21 shows a typical polarization curve for H_2 evolution on Ni/(RuO_2+NiO_x). A marked hysteresis is clearly visible between the forward and the backward polarization scan. In particular, electrodes exhibit higher current at lower potential in the backward direction. This behaviour points out an activation of electrodes as a consequence of H_2 evolution reaction.

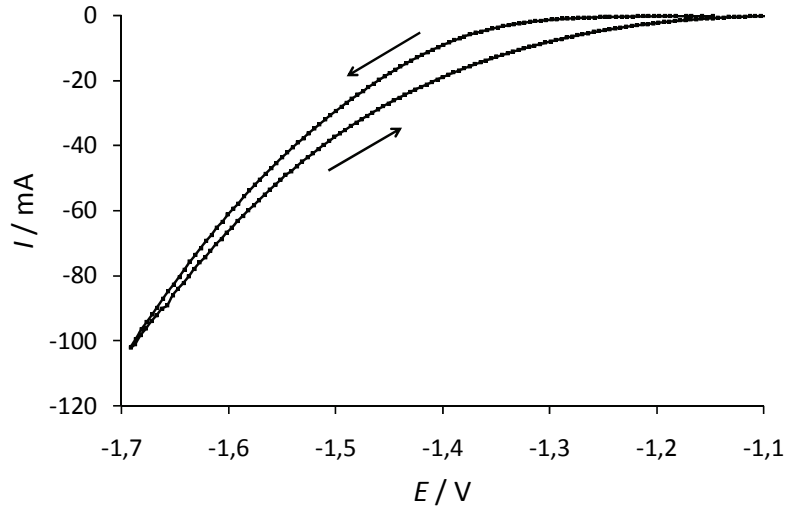

Figure 4.21 Polarization curve for H_2 evolution from 1 mol dm^{-3} NaOH (electrode at 40 mol% RuO_2). Arrows indicate the direction of potential variation.

Uncompensated ohmic resistance values, *R*, and Tafel slopes, *b*, were obtained by the two methods already discussed in Section 4.3.3. Deviations from linearity were observed in the high current density range and were attributed to both uncompensated ohmic drops and/or a change in Tafel slope.

Figure 4.22 shows the uncompensated resistance, *R*, plotted as a function of the composition. Very high *R* values were obtained for electrodes with RuO_2 content less than 10 mol%. This indicates a great instability of the active layer, which is mainly constituted by NiO_x at these compositions. *R* is close to 1.0 Ω for all other electrodes and slightly decreases at very high RuO_2 content. *R* is higher in the backward polarization scan, mostly for electrodes in the composition range between 30 and 90 mol% RuO_2. A possible explanation is the passivation of the Ni substrate.

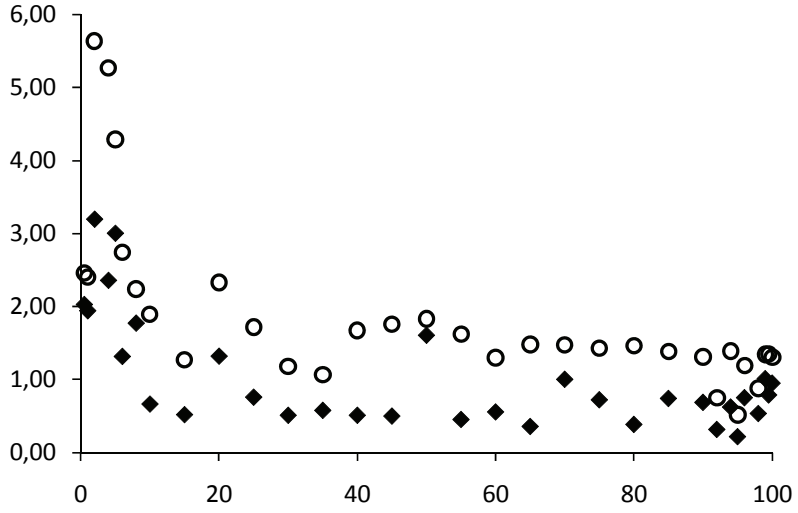

Figure 4.22 Uncompensated ohmic resistance in 1 mol dm^{-3} NaOH solution for Ni/(RuO_2+IrO_x) electrodes as a function of composition. (◆) Forward and (○) backward potential scan. Data from both derivative method and *IR* compensation method are included.

Figure 4.23 shows the dependence of Tafel slope, *b*, as a function of RuO_2 content. Two distinct Tafel slope are identified at low current density and at high current density, in the backward polarization scan.

Tafel slope values close to 120 mV are obtained in the low current density range for electrodes with less than 10 mol% RuO_2. These electrodes exhibit Tafel slope higher than 120 mV at high current density in the backward scan.

Electrodes at intermediate compositions (RuO_2 content between 30% and 90%) show similar Tafel slopes and resistance values. Data are more scattered for electrodes with RuO_2 content higher than 90%. At a first sight, the reaction mechanism is closely related to the applied potential. On the other hand, it does not appear to be affected by variation in composition in the range 30 to 100 mol% RuO_2.

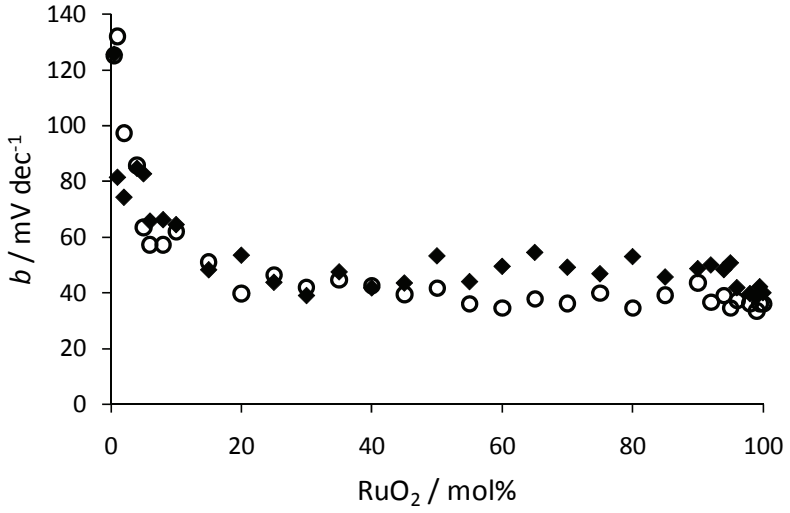

Figure 4.23 Tafel slope for H_2 evolution at low current density from 1.0 mol dm^{-3} NaOH solution on Ni/(RuO_2+IrO_x) electrodes as a function of composition. (◆) Forward and (○) backward potential scan.

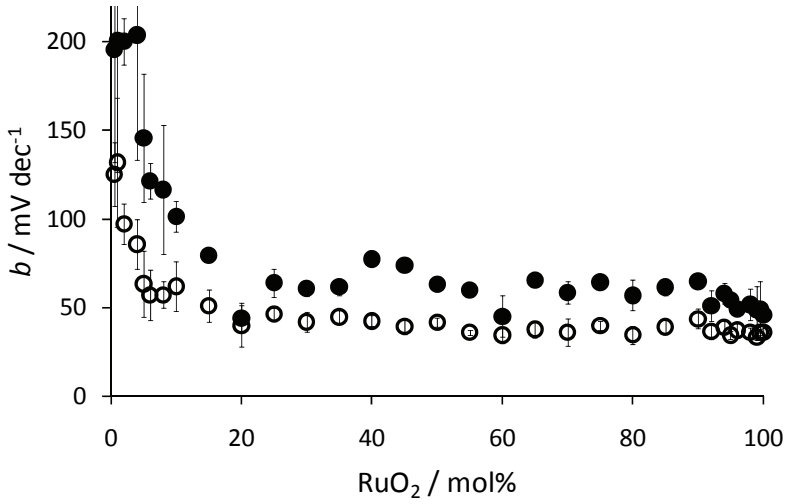

Figure 4.24 Tafel slope for H_2 evolution in the backward scan for Ni/(RuO_2+IrO_x) electrodes as a function of composition. (○) Low current density and (●) high current density.

4.4.3 Electrocatalytic activity

The dependence of the current, *I*, on the composition is shown in Figure 4.25. The current taken during the backward polarization scan can be taken as a measure of the total amount of H_2 produced by the electrodes. The current is almost zero for electrodes with less than 5 mol% RuO_2. They are unsuitable electrocatalyst towards H_2 evolution reaction, as confirmed by high values of resistance and Tafel slope. Then the current starts to increase and is almost constant in the range between 15 and 90 mol% RuO_2. A further increase is visible for electrodes with more than 90 mol% RuO_2.

However, such an evaluation entails both electronic and geometric factors, since the current is an extensive property. In Figure 4.26, the current is reported as a function of voltammetric charge obtained by voltammetric curves after polarization experiment. The trend of data bends upward, suggesting that not only geometric factors are operating.

A better separation between true electrocatalysis and surface area effects can be achieved by normalization to unit voltammetric charge (Figure 4.27). Looking at this picture, electrodes at 25-40 mol% RuO_2 seem to be the most active. It is also noteworthy that the electrodes of pure RuO_2 exhibit slightly lower electrocatalytic activity than electrodes with a small amount of NiO_x (80-95 mol% RuO_2).

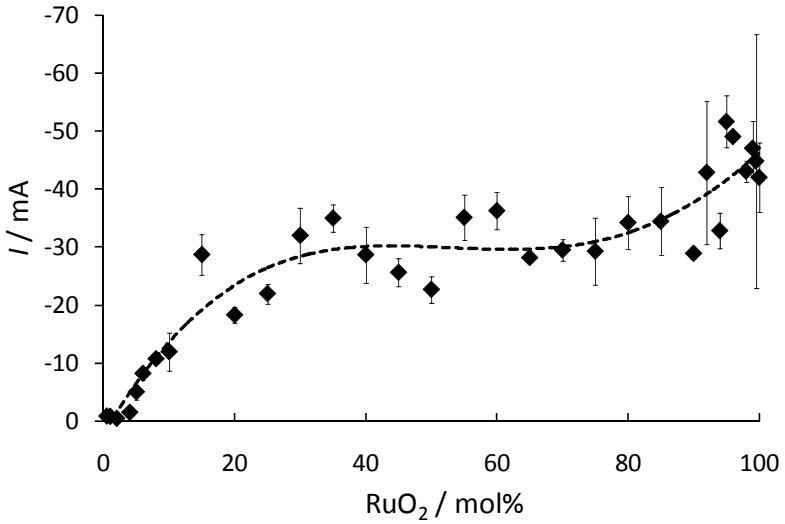

Figure 4.25 Apparent current for H_2 evolution at -1.2 V(SCE) on Ni/(RuO_2+NiO_x) electrodes as a function of nominal composition. The current was taken from the backward scan of polarization curves.

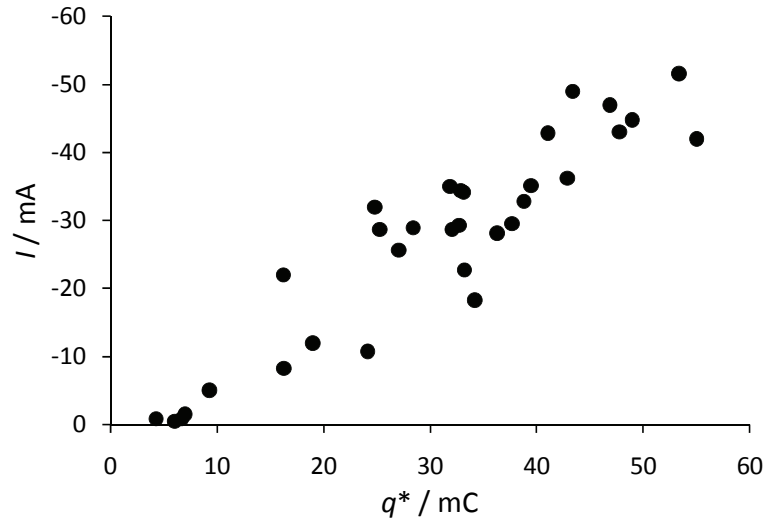

Figure 4.26 Apparent current for H_2 evolution at -1.2 V(SCE) on Ni/(RuO_2+NiO_x) electrodes as a function of voltammetric charge.

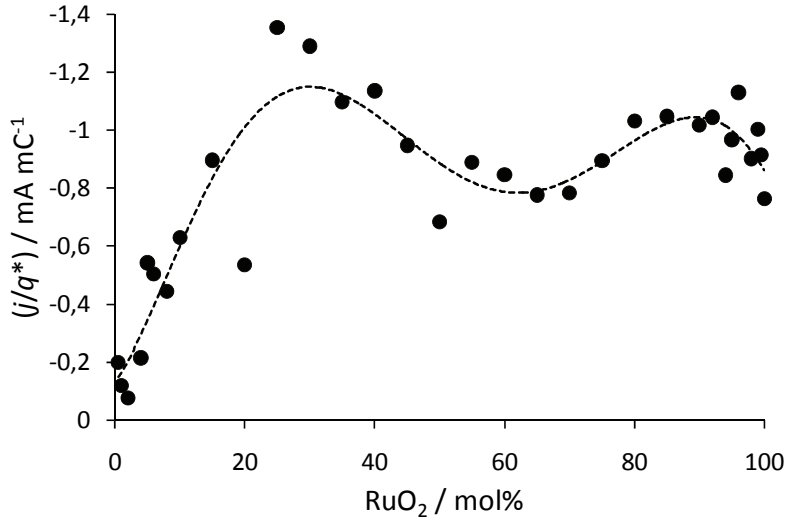

Figure 4.27 Current of H_2 evolution normalized to unit voltammetric charge as a function of electrode composition.

From Figure 4.28, it is clearly visible that electrodes with high NiO_x content need a great overpotential to evolve H_2 at high current. Electrodes at intermediate composition exhibit similar overpotential towards H_2 evolution reaction from alkaline solution. Overpotential for electrode of pure RuO_2 is slightly higher than overpotential for electrode with very small amount of NiO_x.

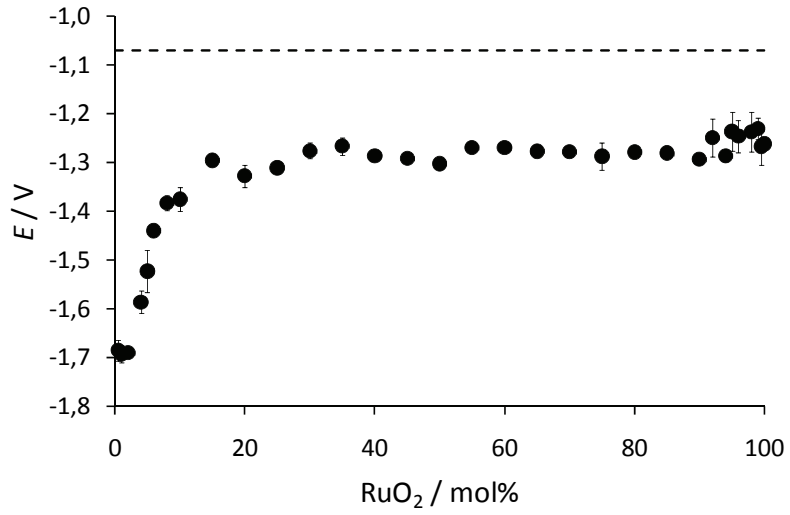

Figure 4.28 Overpotential for H_2 evolution from alkaline solution at I = -50 mA as a function of composition. Reversible potential for H_2 evolution is indicated.

4.4.4 Effects of polarization on the electrode surface state

Voltammetric curves recorded after cathodic polarization experiments are reported in Figure 4.29 for selected samples. CV on fresh electrodes are also reported for comparison. The pseudo-capacitive region is generally enhanced, to a greater extent for electrode with lower RuO_2 content. This is probably due to a partial dissolution of NiO_x with consequent exposure of new RuO_2 surface to the electrolytic solution. For electrodes with lower RuO_2 content, the Ni(II)/Ni(III) redox peak increases after H_2 evolution, probably because more Ni(II) sites become accessible to the solution as a consequence of the increased wetting. This is also likely to be due to the penetration of electrolytic solution through the oxide layer up to the Ni substrate.

Figure 4.30 shows the increase in the pseudo-capacitive region as the RuO_2 content increases. Furthermore, for electrodes at intermediate compositions, the position of Ni(II)/Ni(III) redox peak is shifted towards more positive potentials after the cathodic polarization experiment.

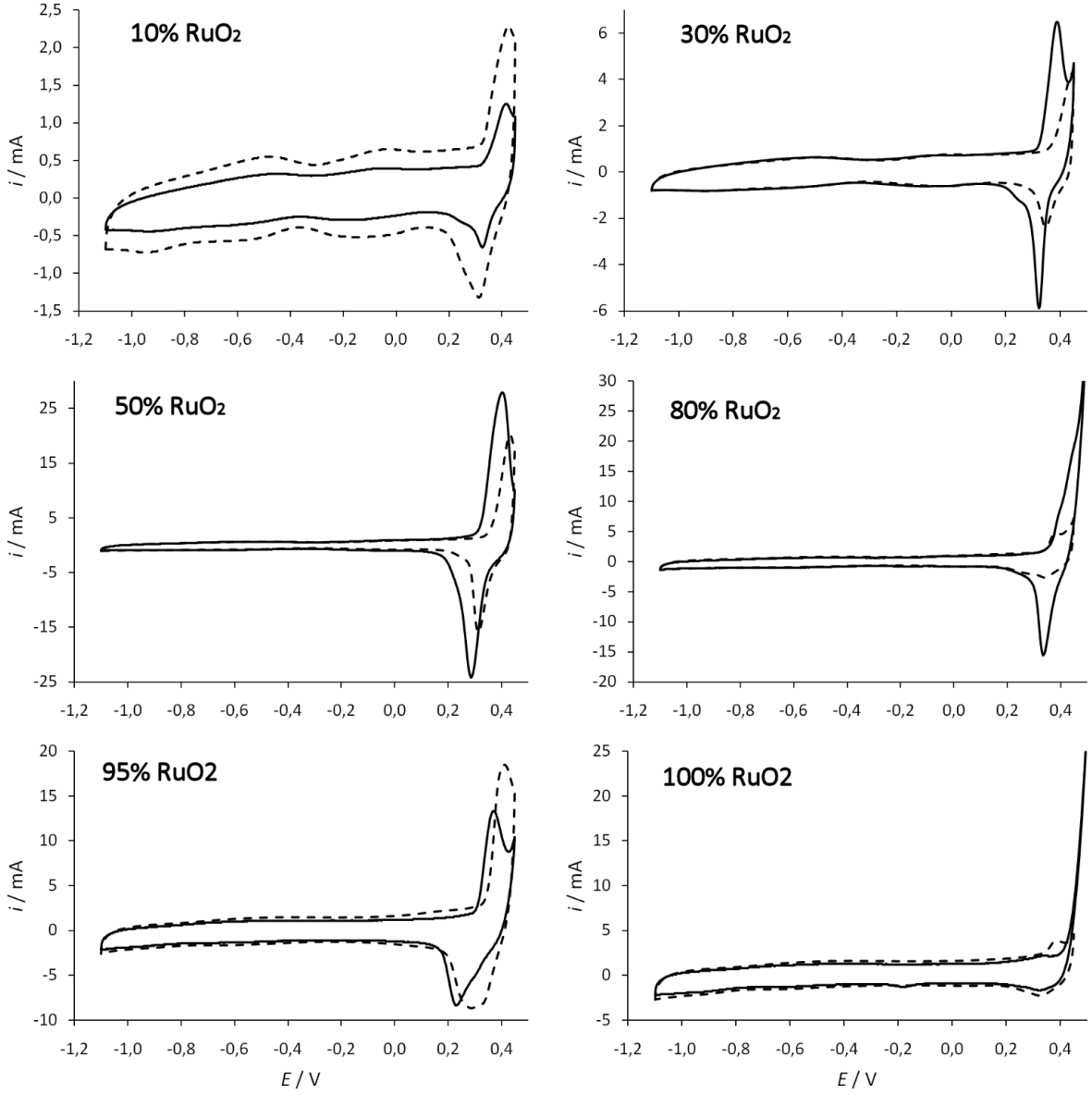

Figure 4.29 Comparison of voltammetric curves recorded before and after polarization experiments. (—) Fresh electrodes; (- - -) After cathodic polarization.

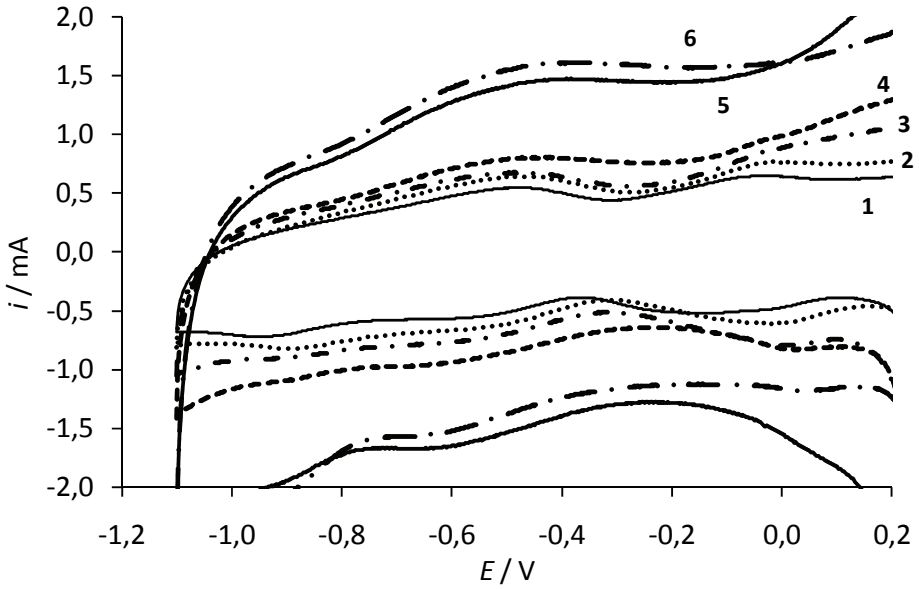

Figure 4.30 Overlay of CV recorded after polarization experiments. (1) 10; (2) 30; (3) 50; (4) 80; (5) 95; (6) 100 mol% RuO_2.

Voltammetric charge, q^*, obtained by integration of voltammetric curves after H_2 evolution is shown in Figure 4.31. The trend is similar to the one recorded on fresh electrodes, with a relative maximum at 60 mol% RuO_2. The highest values were obtained for electrode with more than 90 mol% RuO_2.

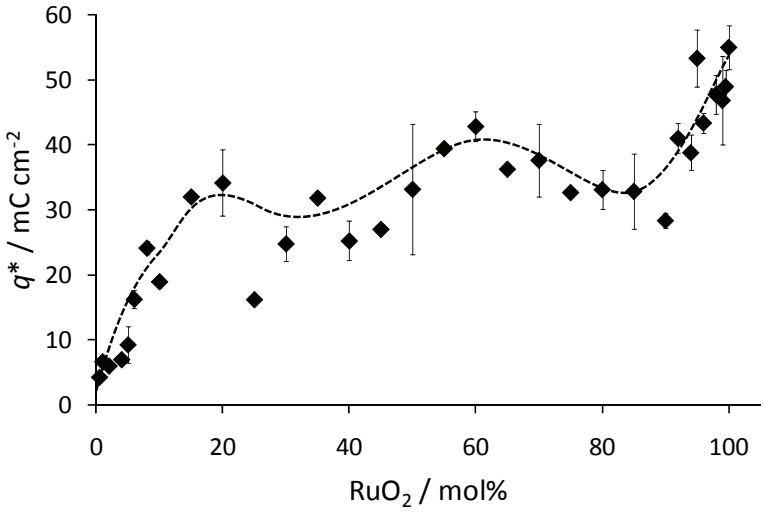

Figure 4.31 Voltammetric charge (q^*) by integration of voltammetric curves after cathodic polarization.

A comparison of voltammetric charge obtained before and after cathodic polarization experiment is provided in Figure 4.31 and Figure 4.32. This is just an indication of the relative stability of electrodes towards the H_2 evolution reaction. There is a general increase in

voltammetric charge after polarization, because of the increased wetting of oxide material as a consequence of cathodic load.

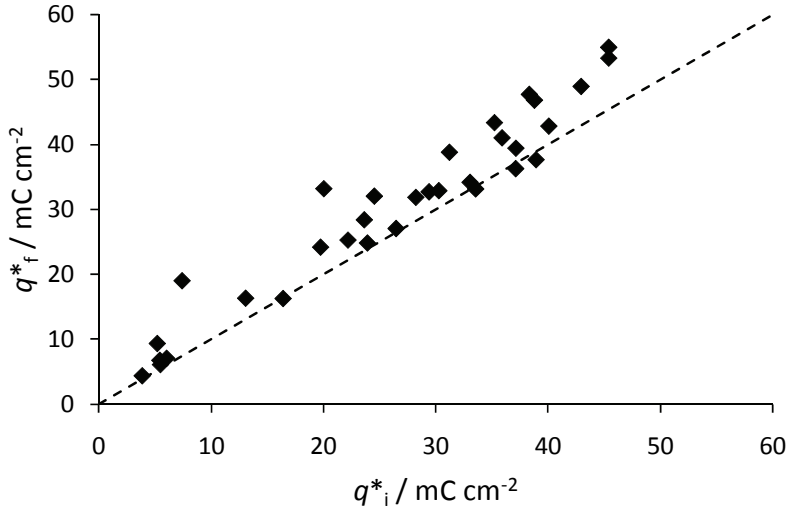

Figure 4.32 Voltammetric charge for fresh sample (q^*_i) plotted against voltammetric charge after cathodic polarization (q^*_f). (···) Straight line of unit slope.

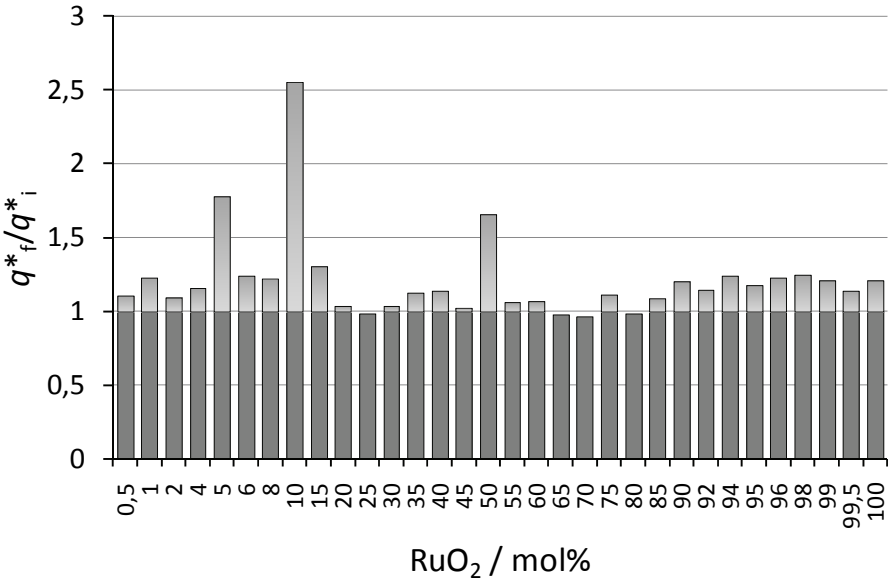

Figure 4.33 Ratio of voltammetric charge after (q^*_f) *vs.* before (q^*_i) H_2 evolution as a function of composition.

SEM analysis was carried on an electrode at 80 mol% RuO_2, previously subjected to cathodic polarization experiment. At lower magnification (Figure 4.34 (a)), the electrode morphology does not differ to the one observed on fresh electrode. Defined geometric structures are well distributed on the amorphous layer below and the cracks are clearly visible. At higher magnification (Figure 4.34 (b) and (c)), the surface appears to be uniformly covered by very small particles. The size is below 50 nm.

It is evident that H_2 evolution from alkaline solution deeply modifies the electrode surface. A possible explanation is the partial dissolution of NiO_x with the exposure of new RuO_2 active sites. In agreement with CV and polarization experiments, after an initial activation process, the electrode surface results to be stabilized.

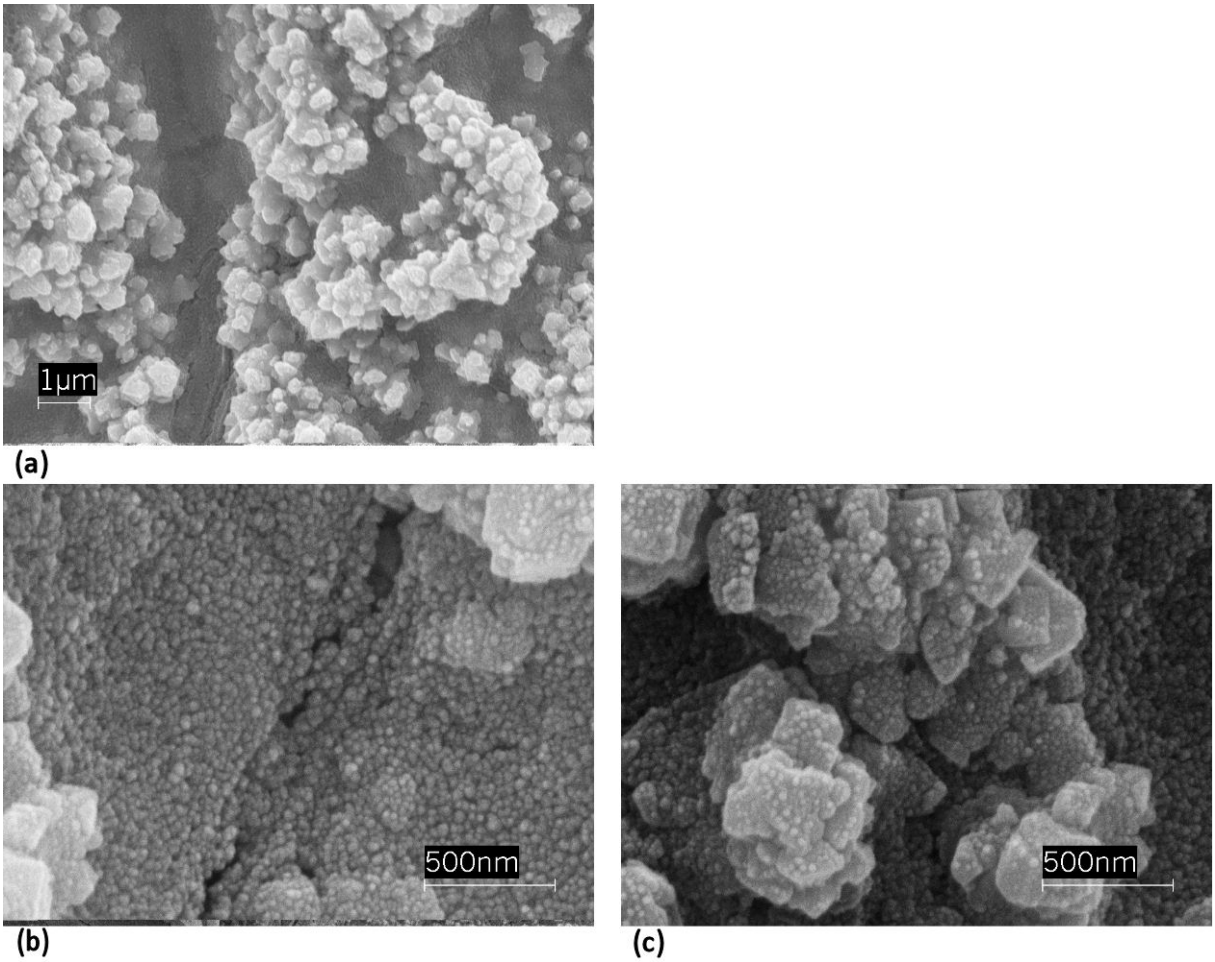

Figure 4.34 SEM micrographs of an electrode at 80 mol% RuO_2 after polarization experiments. (a) 10000×; (b) e (c) 50000×.

4.4.5 Conclusions

- RuO_2+NiO_x mixed oxide electrodes were prepared by thermal decomposition on Ni, in the composition range between 0 and 100 mol% RuO_2.
- Voltammetric behaviour of Ni/(RuO_2+NiO_x) is due to the pseudo-capacitive features of RuO_2 as well as the Ni(II)/Ni(III) redox transition peak of NiO_x.
- Pseudo-capacitive region does not vary too much after cathodic polarization. Increase in surface area is attributed to an increase in RuO_2 wetting.

- As a consequence of cathodic load, the Ni substrate becomes exposed to the electrolytic solution, as confirmed by the appearance of typical Ni(II)/Ni(III) peak for electrodes at 100 mol% RuO_2.
- All electrodes need an activation pretreatment, after which the H_2 evolution mechanism results modified and the apparent activity is greatly enhanced.
- Two distinct Tafel slopes are identified in the low overpotential and in the high overpotential range, for electrodes at higher RuO_2 content. The reaction mechanism is different when the electrode potential is varied.
- Electrode with less than 30 mol% RuO_2 are not stable towards H_2 evolution reaction. Electrodes at intermediate composition (between 30 and 90 mol% RuO_2) exhibit similar kinetic parameters. Electrodes with more than 98 mol% behave as pure RuO_2.
- SEM micrographs recorded before and after cathodic polarization clearly show modifications of the morphology of the electrode surface. This behaviour is likely to be related to the dissolution of NiO_x, with exposure of new active sites to the electrolytic solution.

4.5 Final remarks

- RuO_2+NiO_x mixed oxides prepared by thermal decomposition exhibit different behaviour when tested in alkaline or acidic media.
- Evidences for NiO_x dissolution are provided by cyclic voltammetry and resistance values. Electrodes with less than 20 mol% RuO_2 are not stable towards H_2 evolution reaction neither in alkaline nor in acidic solutions.
- Electrodes prepared on Ti are suitable towards H_2 evolution reaction. It has been found that electrodes with RuO_2 content between 60 and 80 mol% exhibit better electrocatalytic performances than pure RuO_2.

4.6 References

[1] K. Macounova, M. Makarova, J. Franc, J. Jirkovsky, P. Krtil, Electrochem. and Solid State Letters 11 (2008) F27.

[2] M. Makarova, J. Jirkovsky, M. Klementova, I. Jirka, K. Macounova, P. Krtil, Electrochimica Acta 53 (2008) 2656.

[3] K. Macounova, M. Makarova, J. Jirkovsky, J. Franc, P. Krtil, Electrochimica Acta 53 (2008) 6126-6134.

[4] F. Pico, J. Ibanez, T. Centeno, C. Pecharroman, R. Rojas, J. Amarilla, J. Rojo, Electrochimica Acta 51 (2006) 4693-4700.

[5] X.M. Liu, X.G. Zhang, Electrochimica Acta 49 (2004) 229-232.

[6] H. Wendt, V. Plzak, in: H. Wendt (Ed.), Electrochemical Hydrogen Technologies, Elsevier, Amsterdam, 1990, p. 15.

[7] S. Trasatti, International Journal of Hydrogen Energy 20 (1995) 835-844.

[8] S. Trasatti, in: H. Gerischer, C.W. Tobias (Eds.), Advances In Electrochemical Science and Engineering. Vol 2, VCH, Weinheim, 1992, p. 1.

[9] T. Borucińsk, S. Rausch, H. Wendt, Journal of Applied Electrochemistry 22 (1992) 1031-1038.

[10] L. Vázquez-Gómez, S. Cattarin, R. Gerbasi, P. Guerriero, M. Musiani, Journal of Applied Electrochemistry 39 (2009) 2165-2172.

[11] M. De Giz, J. Silva, M. Ferreira, S. Machado, E. Ticianelli, L. Avaca, E. Gonzalez, International Journal of Hydrogen Energy 17 (1992) 725-729.

[12] K. Lohrberg, P. Kohl, Electrochimica Acta 29 (1984) 1557-1561.

[13] M. Jaccaud, P. Leroux, J.C. Millet, Materials Chemistry and Physics 22 (1989) 105-119.

[14] A.C. Tavares, S. Trasatti, Electrochimica Acta 45 (2000) 4195- 4202.

[15] J.C.F. Boodts, G. Fregonara, S. Trasatti, in: F. Hine, J.M. Fenton, B.V. Tilak, J.D. Lisius (Eds.), Performance of Electrodes for Industrial Electrochemical Processes, The Electrochemical Society, Pennington, NJ, 1989, p. 135.

[16] S. Trasatti, in: T.C. Wellington (Ed.), Modern Chlor-Alkali Technology, Elsevier, Amsterdam, 1992, p. 281.

[17] S. Trasatti, in: J. Lipkowski, P.N. Ross (Eds.), The Electrochemistry of Novel Materials, VCH, New York, 1994.

[18] V. Srinivasan, J.W. Weidner, Journal of The Electrochemical Society 147 (2000) 880-885.

[19] D. Yohe, A. Riga, R. Greef, E. Yeager, Electrochimica Acta 13 (1968) 1351-1358.

[20] S. Trasatti, G. Buzzanca, Journal of Electroanalytical Chemistry 29 (1971) A1-A5.

[21] B.E. Conway, Journal of The Electrochemical Society1 138 (1991) 1539.

[22] S. Trasatti, Electrochimica Acta 36 (1991) 225-241.

[23] S. Trasatti, G. Lodi, in: S. Trasatti (Ed.), Electrodes of Conductive Metallic Oxides, Part B, Elsevier, 1981, p. 521.

[24] S. Trasatti, Materials Chemistry and Physics 16 (1987) 157-174.

[25] S.I. Cordoba-Torresi, A. Hugot-LeGoff, S. Joiret, Journal of The Electrochemical Society 138 (1991) 1554.

Chapter 5. RuO_2 modified by NiO_x: a non-aqueous synthesis

5.1 Introduction

As said in Chapter 4, ruthenium oxide is one of the most active materials for cathodic hydrogen evolution from acidic solutions. Its stability in acidic media is due to high conductivity of the crystalline phase [1].

Looking at the literature, most studies on electrochemical behaviour of RuO_2 deal with films prepared by conventional thermal decomposition of chloride or nitrates in the temperature range 175-450 °C. The electrochemical response is strongly affected by the preparation method, which affects hydration and microstructure of the samples. The electrochemical response is directly related to the crystallinity of the sample.

The electrocatalytic activity of RuO_2 can be enhanced by increasing crystal defects and modifying the number or energy profile of surface active sites. Thus the reduction of the size of crystallites is a suitable way. Doping and chemical mixing of RuO_2 with other elements points to the same goal (cf. Chapter 4).

In this part of the present work, both strategies have been applied. Ni-doped RuO_2 was synthesized by co-precipitation method, followed by dehydration, annealing and milling. Nickel was used to distort RuO_2 crystal structure. The same method was used by Krtil to prepare Ni-doped RuO_2[2].

The precipitation of oxides, from both aqueous and nonaqueous solutions, is less straightforward than the precipitation of metals. Reactions for the synthesis of mixed oxides by co-precipitation can generally be divided into two categories: those that produce an oxide directly and those that produce a precursor that must be subjected to further processing (drying, calcination, etc.) [3]. In both cases, monodispersed oxide nanoparticles, like metals, frequently require a capping ligand or other surface-bound stabilizer to prevent agglomeration of the particles. However, when calcination or annealing is necessary, some agglomeration is unavoidable.

The products of co-precipitation reactions, particularly those performed at or near room temperature, are usually amorphous. In those cases where hydroxides of mixed metals

are precipitated from solution and subjected to a calcination or annealing process, it is extremely difficult to experimentally determine whether the as-prepared precursor is a single-phase solid solution or a multi-phase, nearly-homogeneous mixture of the constituent metal hydroxides-oxides that react to form a single-phase mixed-metal oxide when heated.

Beyond the control of the composition and the processing of materials, the development of low-temperature routes to materials aims to allow the control of their microstructure. In sol-gel methods, which are based on the hydrolysis-condensation of molecular precursors, such as metal alkoxides, the major problem is to control the reaction rates which are generally too fast, resulting in loss of microstructural control over the final oxide material. A suitable strategy to overcome this problem is provided by nonhydrolytic sol-gel processes, in which precursors, solvent, experimental conditions, and reaction mechanisms are changed [4].

Reactions in non-aqueous solvent can be particularly advantageous in the co-precipitation of different metals that cannot be simultaneously precipitated from aqueous solution, because of large variations in the pH values are needed to induce precipitation of the cations.

The here adopted synthesis was firstly proposed by Music and co-workers [5]. It is based on the addition of a strong organic alkali (tetramethylammonium hydroxide, TMAH) into an alcoholic solution of $RuNO(NO_3)_3$ and heating at 90°C. Further thermal treatment of amorphous ruthenium hydrous oxide resulted in 14 nm crystalline RuO_2. On the other hand, precipitation of ruthenium hydrous oxide from aqueous solution required over 2 weeks at 90 °C and ultimately resulted in products containing about 5% metallic Ru.

Very detailed investigations have been carried out on the structural and electrochemical properties of transition metal oxides. However little is known regarding the structure and electrocatalytic properties of oxide powders. This is mainly due to the prevalence of transition metal oxides electrodes in industrial processes compared with the same oxide compositions in particle form. Furthermore, it is well known that a wide range of preparation conditions affect the formation and properties of oxide layers [6]. Therefore the characterization of oxides powder would give an insight to the their specific nature as electrocatalysts and in the same time would provide a possible use in PEM water electrolysis applications.

5.2 Experimental

5.2.1 Electrodes

Ruthenium(III)-nitrosylnitrate, $RuNO(NO_3)_3$, was supplied by Alfa Aesar. Nickel nitrate, $Ni(NO_3)_2 \times 6H_2O$, tetrabuthylammonium hydroxide TBAH, $(CH_3CH_2CH_2CH_2)NOH$, 40% w/w aqueous solution, ethanol, C_2H_6O, and 2-propanol, C_3H_8O, were supplied by Sigma Aldrich. Mixture of ethanol and 2-propanol (volume ratio 1:1) was used as solvent for $RuNO(NO_3)_3$.

Ru and Ni mixed oxide powders were prepared at different composition. Proper amount of $RuNO(NO_3)_3$ and $Ni(NO_3)_2 \times 6H_2O$ were dissolved in 30 mL of the alcoholic solvent. The RuO_2 content in the starting solutions was: 10, 30, 40, 50, 60, 80, 98, 99.5, 100 mol%. The TBAH (4 mL) was added to the alcoholic solution of precursor salts. The precipitate formed immediately and was then dissolved after strong stirring. The suspension was aged for 24 hours at 100 °C. After cooling, H_2O_2 (4 mL) was slowly added to oxidize Ru^{3+} into Ru^{4+}. The precipitate was isolated using a centrifuge. After elimination of mother liquor, the precipitate was washed several times with double distilled water, dried in open air and then annealed at 400 °C for 1 hour. Products were then milled in an agate mortar in order to destroy agglomerates.

To obtain electrodes suitable for electrochemical characterization, oxide powder were suspended in water and sonicated. Catalyst powder suspensions were then deposited by brushing onto Ti platelets (5×5 mm size) until a load of 4 mg was reached. Three samples were prepared at each composition. The Ti platelets were previously sandblasted and etched in boiling oxalic acid (10% w/w) for 1 hour just before use. Such prepared electrodes were further stabilized by annealing at 400 °C in air for 1/2 hour and mounted in a Pyrex tube.

5.2.2 Experimental methods

The phase composition of the samples was determined at room temperature by X-ray powder diffraction. The particle morphology and chemical composition of the prepared materials were analyzed using a scanning electron microscope (SEM model LEO 1430) equipped with an energy dispersive X-ray analyser.

Electrochemical techniques were used to investigate the electrochemical response of the surface towards H_2 evolution reaction. All electrochemical experiments were conducted in 0.5 mol dm^{-3} $HClO_4$ aqueous solutions at 25±0.1 °C in a water thermostat. Solutions were deareated by bubbling purified N_2 for 20 minutes before experiments. The water used to prepare solutions was obtained from a Millipore-Milli Q distillation apparatus. Electrode

potentials were measured and are reported with a satured calomel electrode (SCE) as reference electrode.

All electrochemical experiments were carried out using an EG&G Model 273A potentiostat/galvanostat connected to a personal computer. The electrochemical cell was constituted by four compartments separated by glass frits. Two Pt electrodes were used as counterlectrodes. The compartment of the reference electrode was connected to the surface of the working electrode via a Luggin capillary.

Voltammetric curves were recorded when stabilized (10 cycles). The electrode potential was scanned between -0.2 and 1.1 V (SCE) at 20 mV s^{-1}. As usual, voltammetric curves were recorded for fresh samples, for samples after cathodic polarization curves, for samples after determination of the reaction order. Voltammetric charges were obtained by graphical integration of the voltammetric curves.

Quasi-stationary potentiostatic curves were recorded by keeping the potential at open circuit potential for 15 min, then at -0.2 V(SCE) for 5 min, and then by stepping the potential of 10 mV. The current was read after 1 minute at each potential. As the current reached about 100 mA, the direction of potential scan was reversed and experiments continued until the current became anodic.

The reaction order with respect to H^+ for the cathodic H_2 evolution was determined by recording polarization curves at different concentrations of $HClO_4$ (0.1, 0.18, 0.32, 0.56, 1 mol dm^{-3}). The ionic strength was kept constant by addition of proper amount of $NaClO_4$.

The electrode was kept at -0.2 V for 5 min, then the potential was stepped in the cathodic direction and then reversed and stepped in the anodic direction. Potential and time sequence was as follows: -0.2 V (3 min) → -0.25 V (3 min) → -0.3 V (3 min) → -0.32 V (3 min) → -0.3 V (3 min) → -0.25 V (3 min) → -0.2 V (3 min). The current was read directly from the chronoamperometric curve at -0.3 V(SCE) in the reverse scan. The potential was selected as to lie in the linear portion of polarization curves. The order of reaction was derived from plots of log j at -0.3 V(SCE) *vs.* pH.

5.3 Results

5.3.1 Physico-chemical characterization

The XRD patterns of NiO_x and RuO_2+NiO_x at three different compositions are shown in Figure 5.1. The XRD patterns were successfully indexed on the base of material structure. The XRD patterns exhibited the characteristic peaks of rock salt NiO_x at 2θ = 37.1, 43.1 and

62.7°, 75.2°, 79.2°. The grain size of the crystalline, *D*, was calculated from the major diffraction peak (200) using the well-known Scherrer's formula:

$$D = \frac{0.9\lambda}{B\cos\theta} \tag{4.4}$$

where λ is the wavelength, *B* the full width at half maximum of the peak, and θ the Bragg's angle of the XRD peak. The grain size was found to be about 118 nm.

For electrodes at 98 and 95 mol% RuO_2, the characteristic peaks of RuO_2 were shown at 2θ = 28.0, 35.1 and 54.5°. Peaks of RuO_2 appear broader than peaks of NiO_x and their relative intensities are much lower.

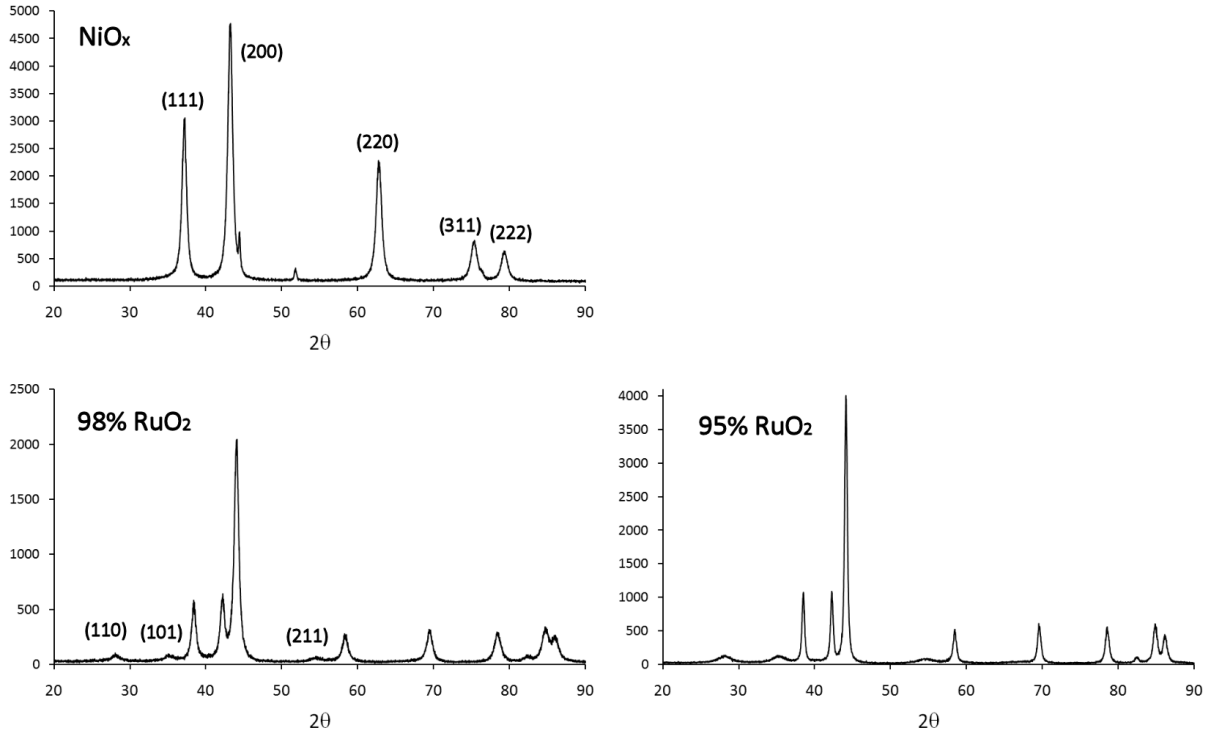

Figure 5.1 XRD patterns of samples at different compositions.

The addition of H_2O_2 was a key point in the synthetic procedure. Music and coworkers [5] showed that amorphous ruthenium hydrous oxide, obtained by hydroxide precipitation, easily transforms into RuO_2 and Ru upon thermal treatment. Smaller crystallites and absence of Ru metal have been obtained by heating the reaction mixture for 24 h and then adding H_2O_2.

In the present work, the effect H_2O_2 on NiO_x was also investigated. The addition of H_2O_2 influences the size of crystallites. As a matter of fact, the grain size calculated from the peak (200) of NiO_x was about 180 nm when H_2O_2 was not added during the synthesis.

SEM images of samples at various compositions are shown in Figure 5.2. Big blocks of irregular shape coexist with smaller structures for electrodes at 50 and 80 mol% RuO_2. The

morphology can be probably attributed to insufficient milling of powders. SEM images at higher magnification (Figure 5.3) shows that bigger particles consist of agglomerates of smaller particles.

The relative content of Ni and Ru agrees with the nominal relative content of NiO_x and RuO_2, as confirmed by EDX analysis (Figure 5.4).

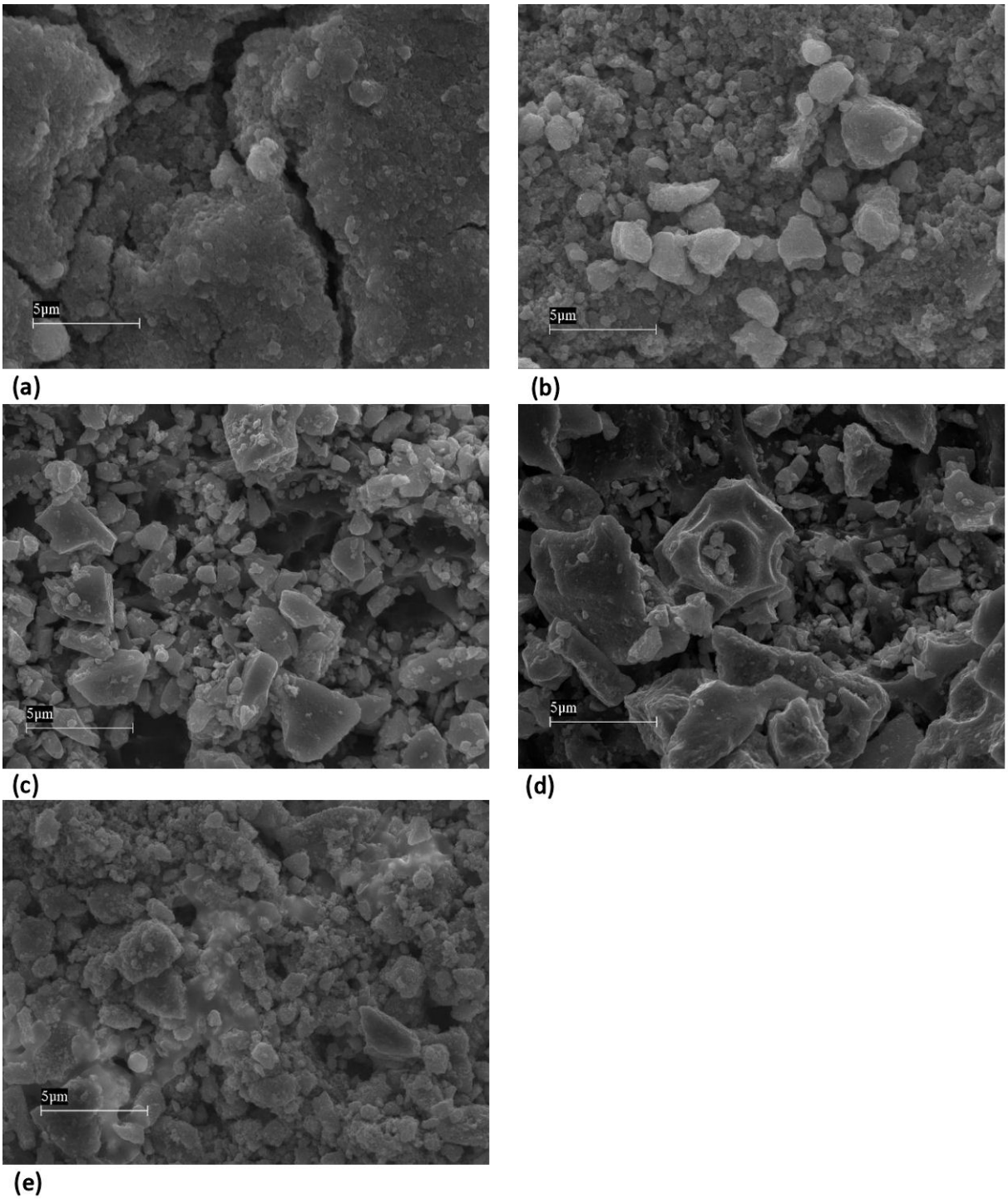

Figure 5.2 SEM micrographs (5000 ×) of RuO2+NiOx powders at different contents of RuO2. (a) 0; (b) 10; (c) 50; (d) 80; (e) 100 mol% RuO2.

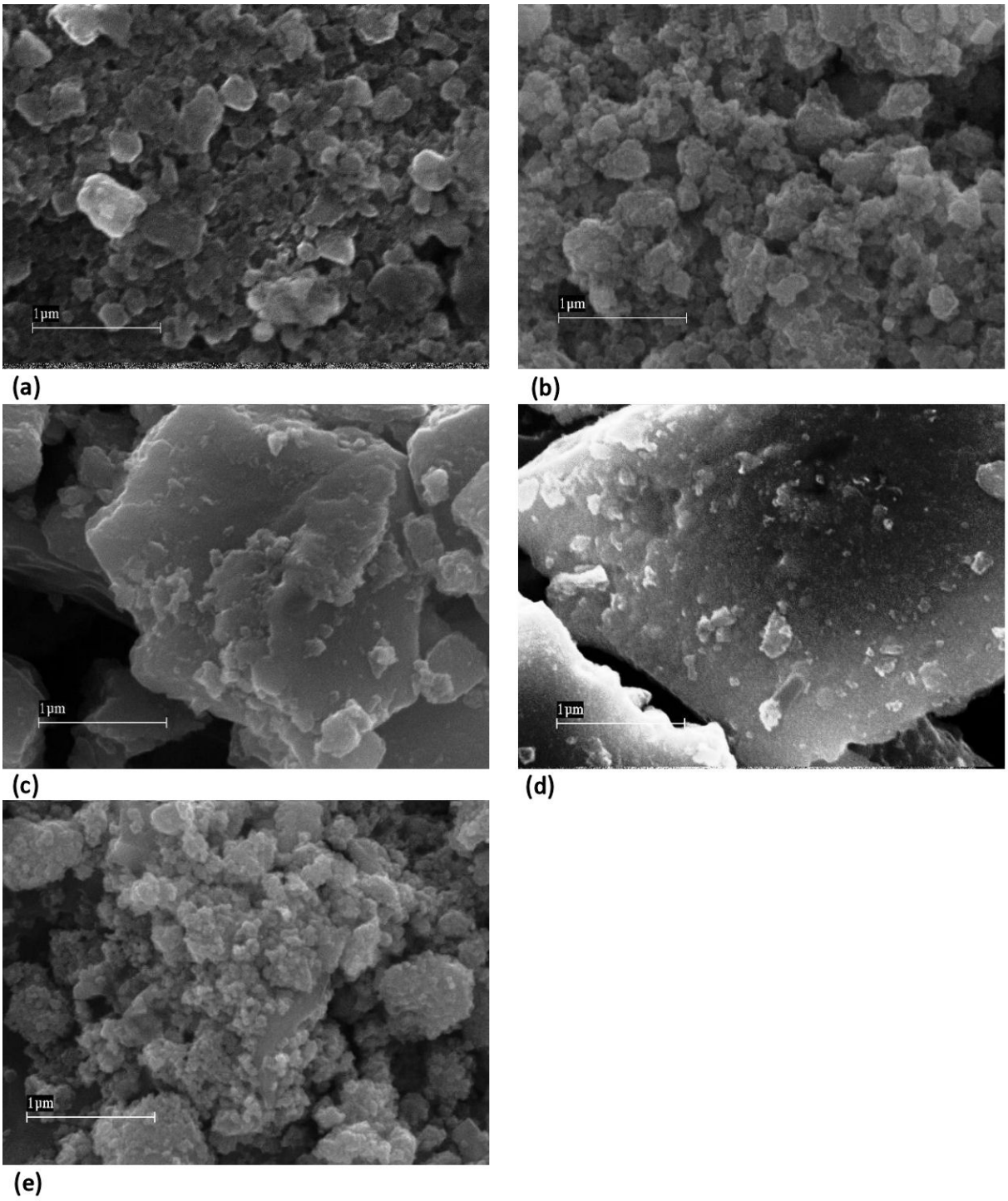

Figure 5.3 SEM micrographs (30000 ×) of RuO2+NiOx powders at different contents of RuO2. (a) 0; (b) 10; (c) 50; (d) 80; (e) 100 mol% RuO2.

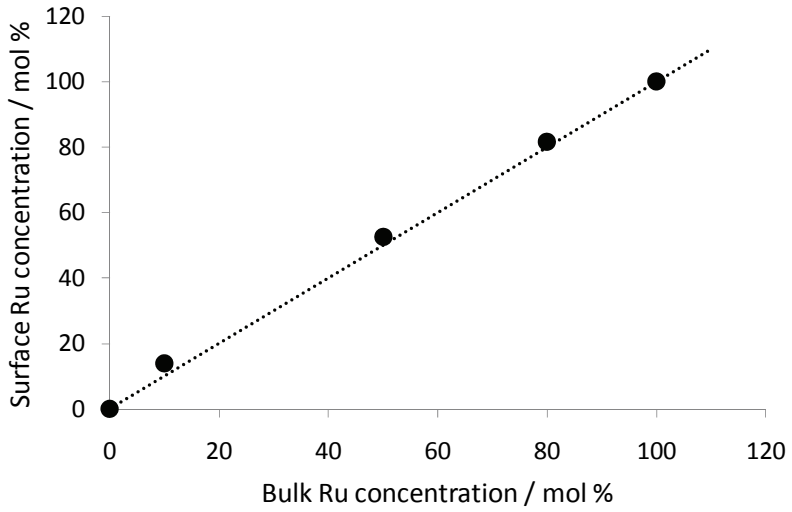

Figure 5.4 Surface Ru concentration from EDX vs. nominal Ru concentration.

5.3.2 Voltammetric curves and surface charge

Surface properties of fresh samples were investigated by cyclic voltammetry. In Figure 5.5, voltammetric curves on fresh electrodes are shown for some compositions.

On the negative end of the potential range, the curves widen as the RuO_2 content increases. It is interesting to note that the area of electrode at 40 mol% RuO_2 is much higher than others. This is not an experimental artifact, since it was reproducible for samples of same composition prepared in different times.

Electrodes with more than 30 mol% RuO_2 exhibit quite featureless curves typical of hydrous RuO_2. The distortion of the curves with respect to *x*-axis could be due to some resistance through the oxide film or at the interface between the deposited powders and the Ti support.

The voltammetric charge, *Q*, was determined by integration of the voltammetric curves in the potential range 0.1 to 1.1 V(SCE). In Figure 5.6 voltammetric density charge, *q**, is reported as a function of composition. *q** is obtained by dividing the charge, *Q,* by the geometric surface area of the samples (2 cm^2). The charge density for electrode at 40 mol% RuO_2 is more than 6 times the charge density at other compositions. Similar value was obtained only for electrode of pure RuO_2. Interpretation is difficult. The maximum for 40 mol% RuO_2 could be attributed to surface enrichment in RuO_2. However detailed XPS analysis would be clarifying.

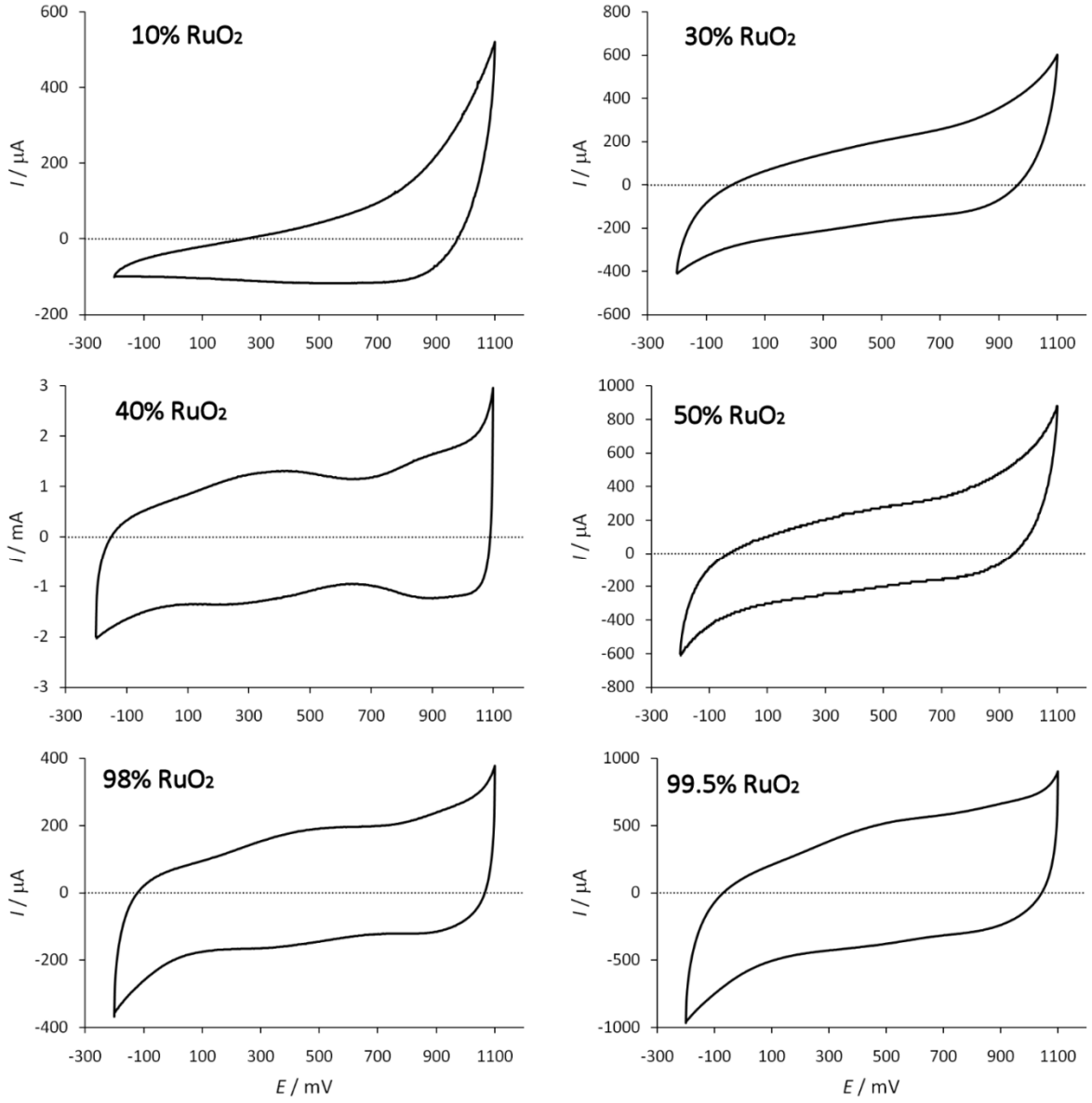

Figure 5.5 Cyclic voltammetric curves at 20 mV s-1 in 0.5 mol dm-3 HClO4 solution on (RuO2+NiOx) mixed oxide electrodes of different compositions.

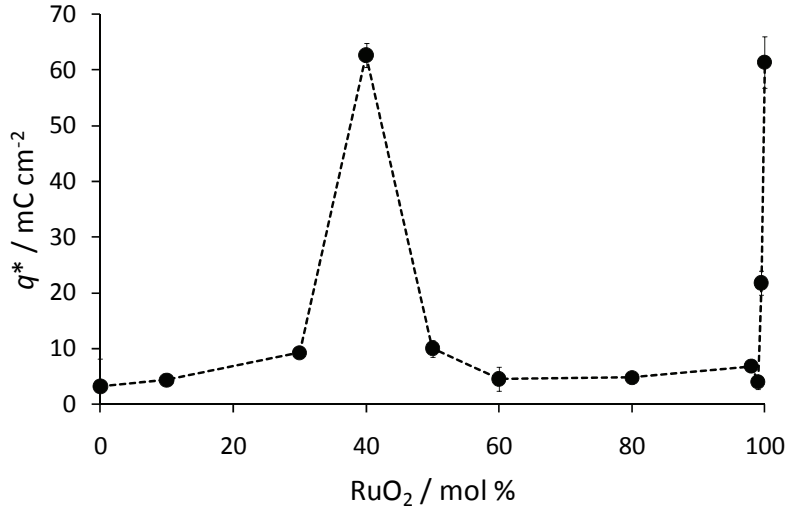

Figure 5.6 Charge density, q*, as a function of nominal composition.

5.3.3 Polarization curves

Figure 5.7 shows quasi-steady polarization curves for H_2 evolution from 0.5 $HClO_2$ mol dm^{-3} solution on mixed oxide electrodes of different compositions. Higher current densities were observed at lower overpotential as the RuO_2 content increases.

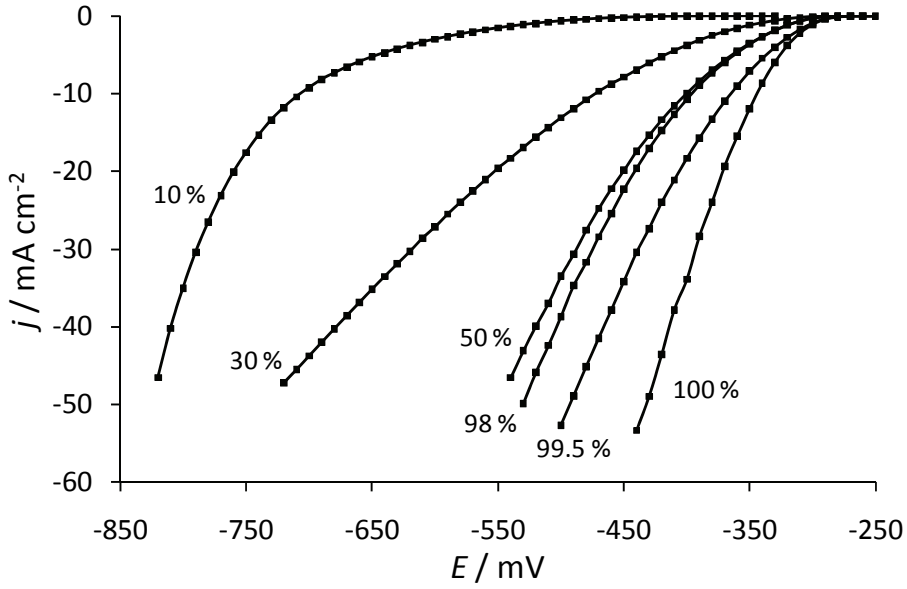

Figure 5.7 Polarization curves for H2 evolution from 0.5 mol dm-3 HClO4 solution on (RuO2+NiOx) oxide electrodes of different compositions (as indicated).

In order to obtain kinetic parameters, Tafel plots were obtained by plotting *E vs*. log *j* (Figure 5.8). Some hysteresis was observed between forward and backward polarization scan for all electrodes.

Deviations from Tafel lines were observed at high current densities. This behaviour can be attributed to uncompensated ohmic drops and/or change in Tafel slope and correction for ohmic drop is needed to allow for correct interpretation.

Tafel slope and resistance values obtained from the Tafel plots using two different methods [7] are reported in Table 3.1. Details for the two methods (*IR* compensation and derivative method) were already described in Chapter 3 and Chapter 4.

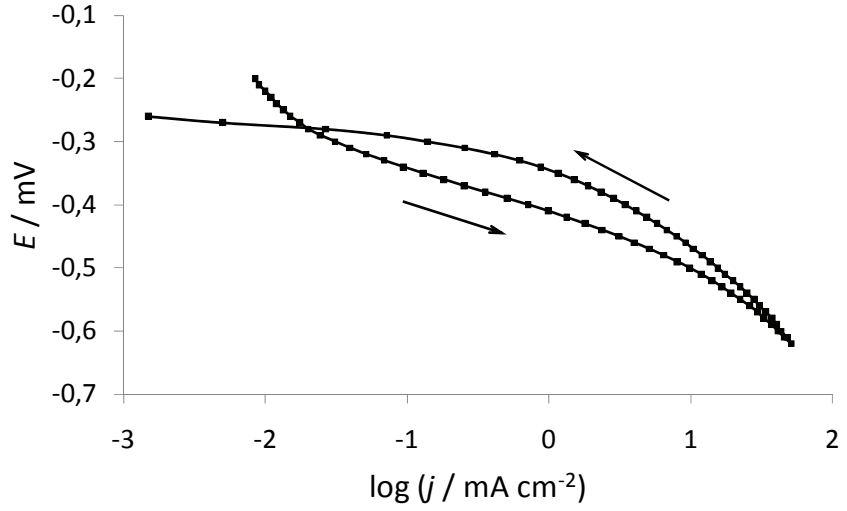

Figure 5.8 Typical E vs. logj plot. Arrows indicate the direction of potential variation.

RuO_2 / mol%	Forward polarization			Backward polarization		
	b / mV decade^{-1}		*R* / Ω	*b* / mV decade^{-1}		*R* / Ω
	low current	high current		low current	high current	
0	128		0.83	138		1.49
10	65	164	0.17	82	161	0.73
30	74	97	1.23	41	110	1.66
40	50	69	0.93	35	72	1.11
50	57	94	0.75	36	99	1.03
60	63	90	0.68	40	123	0.78
80	67	88	1.1	35	128	0.91
98	51	82	0.67	32	103	0.81
99	54	90	0.69	34	117	0.77
99.5	43	73	0.9	32	68	1.16
100	30		0.49	32		0.75

Table 5.1 Kinetic parameters for HER on RuO_2+NiO_x electrodes

The uncompensated ohmic resistance, *R*, can reveal barriers at the support/oxide interface. As shown in Figure 5.9, uncompensated ohmic resistances for RuO_2+NiO_x powders on Ti are generally lower in forward scan. *R* goes through a maximum for electrode at 30 mol% RuO_2, and then decreases for higher RuO_2 content. The lowest resistance values for

RuO_2 content less than 10 mol% can be due to the dissolution of NiO_x in acidic solutions, that results in thinner oxide layers and in the exposition of Ti substrate to the solution.

Resistances values are higher than values obtained on RuO_2+NiO_x electrode prepared by thermal decomposition (cf. Chapter 4). A possible explanation can be that the contact between the support and the catalyst powders is not enough to ensure good electronic conductivity.

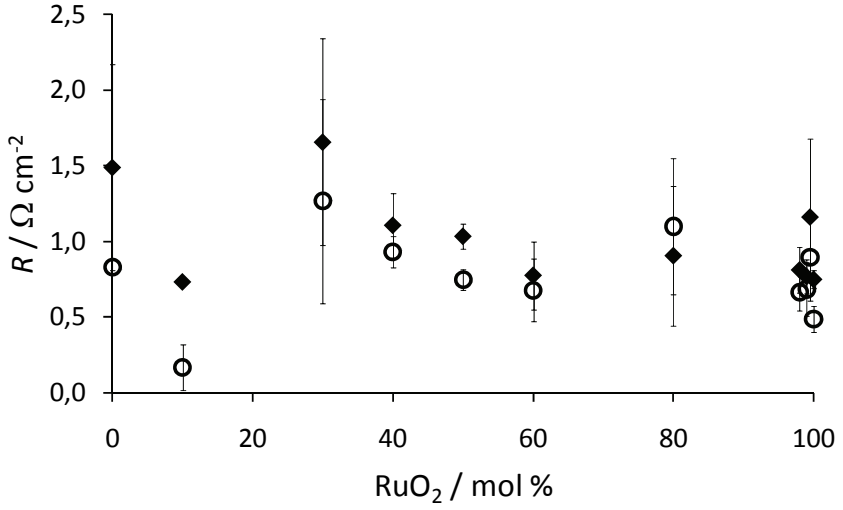

Figure 5.9 Uncompensated ohmic resistance in 0.5 mol dm-3 HClO4 solution as a function of composition. (○) Forward and (◆) backward potential scan.

5.3.4 Tafel slopes

Two Tafel slopes were observed for most electrodes both in the forward and in the backward polarization scans. Only one Tafel slope was observed for electrodes of pure RuO_2.

Tafel slopes for forward polarization are higher than for backward polarization. This trend points to a modification of the surface active sites as a consequence of prolonged H_2 evolution. Figure 5.10 shows that Tafel slope, *b*, is close to 120 mV for 0 mol% RuO_2. It decreases to about 80 mV for 10 mol% RuO_2, and then it further decreases to 40 mV at 30 mol% RuO_2. For higher compositions, *b* slightly decreases with RuO_2 content from about 40 mV down to 30 mV.

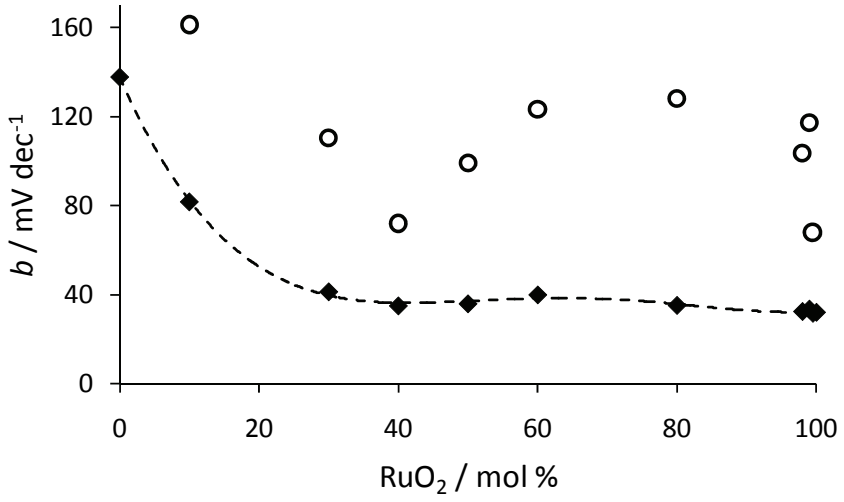

Figure 5.10 Tafel slope for H2 evolution from 0.5 mol dm-3 HClO4 solution as a function of composition. (◆) Low current and (○) high current density.

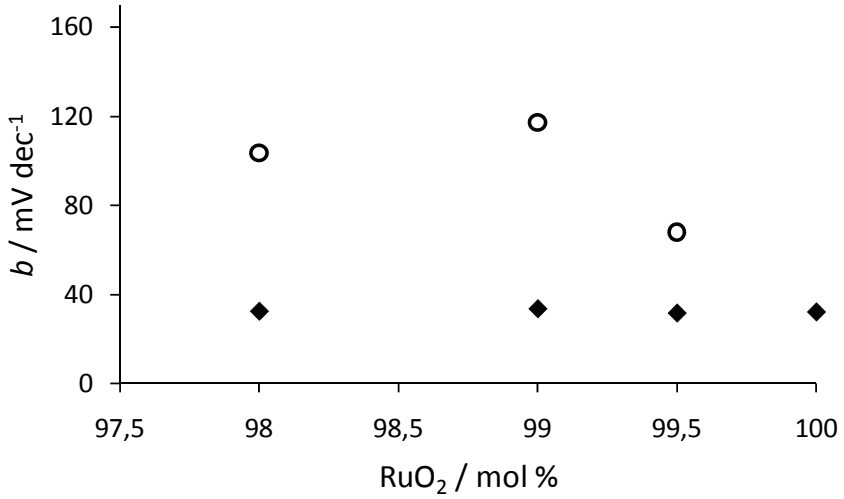

Figure 5.11 Tafel slope for H2 evolution from 0.5 mol dm-3 HClO4 solution for electrode between 98 an 100 mol% RuO2. (◆) Low current and (○) high current density.

Cathodic polarization curves were recorded twice for each electrode. The hysteresis between forward and backward scan was less evident in the second run. However, kinetic parameters are similar in the first and in the second run.

5.3.5 Reaction mechanism

On the basis of Tafel slopes, a reaction mechanism can be proposed. Since the Tafel slope varies from 120 for 0 mol% RuO_2 to about 40 for intermediate compositions and down to 30 mV for higher RuO_2 content, thus the mechanism is probably a classic one:

$$M + H^+ + e \rightarrow MH_{ads} \tag{4.5}$$

$$MH_{ads} + H^+ + e \rightarrow M + H_2 \tag{4.6}$$

$$MH_{ads} + MH_{ads} \rightarrow 2M + H_2 \quad (4.7)$$

In the case of 0 mol% RuO_2, the first discharge (4.5) is the rate determining step. Step (4.6) and (4.7) are alternative. The former prevails on electrode with RuO_2 content between 30 and 80 mol% and the latter prevails at higher RuO_2 content. Taking into account the theory of H_2 evolution (cf. Chapter 2) and if the coverage, θ, could be assumed close to zero, the rate determining step for a 120 mV Tafel slope would be the primary discharge (4.5). However, considering that 120 mV is the second Tafel slope (high current densities), a coverage close to 1 should be more appropriate. Thus, in this case, the determining step is predicted to be the electrochemical desorption (4.6).

5.3.6 Reaction order

Determination of reaction orders can help in the determination of the rate determining step. In Figure 5.13 the reaction order, determined as described in the Experimental section, is plotted as a function of the RuO_2 content.

The mechanism outlined above predicts an order of reaction with respect to H^+ equal to 2 in the case of electrochemical desorption as well as chemical recombination. This implies that the order of reaction should not vary either with compositions. As a matter of fact, reaction order is fractional and increases with increasing RuO_2 content. Fractional reaction orders are usually observed with oxide surfaces [8], because of their acid-base properties.

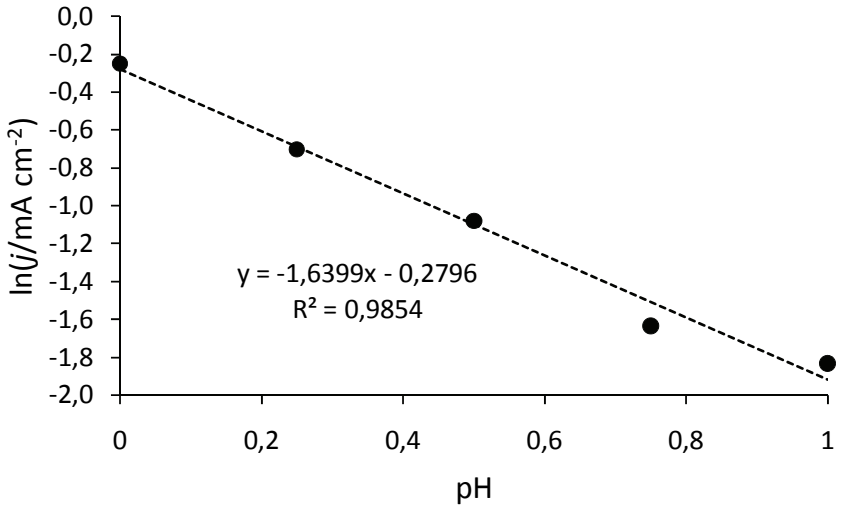

Figure 5.12 Typical example of ln *j vs.* pH plot. Interpolation slope is taken has the reaction order, β_{H+}.

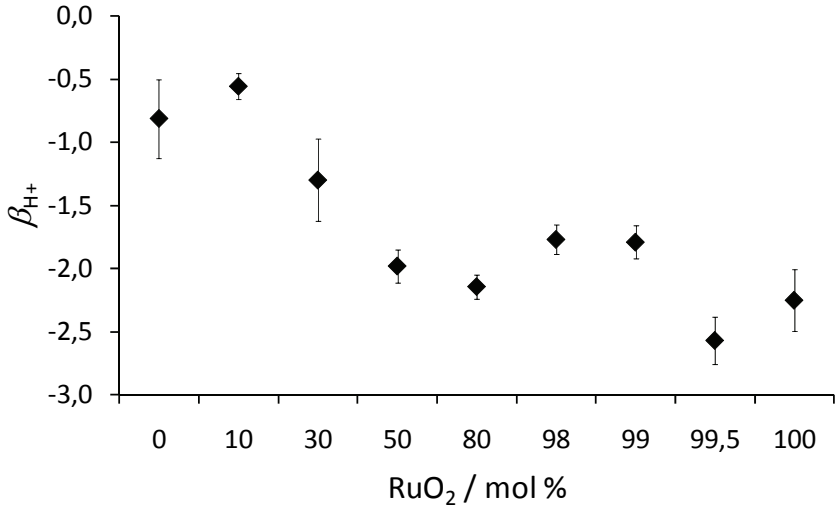

Figure 5.13 Order of reaction with respect to H^+ for H_2 evolution from 0.5 mol dm^{-3} $HClO_4$ + $NaClO_4$ solution as a function of composition.

5.3.7 Electrocatalytic activity

In Figure 5.14 the electrocatalytic properties are evaluated by plotting the current density at -300 mV(SCE) as a function of composition. The current density is a measure of the activity of the materials. Activity is about zero for electrode at 10 mol% RuO_2, then it increases and is almost constant for intermediate compositions. The highest activity is exhibited by electrodes at 99.5 and 100 mol% RuO_2.

Both geometric and electronic effects are included in this evaluation of activity. True electrocatalytic affect can be assessed if the observed current density is normalized to the unit of surface area. Surface area is estimated by means of the voltammetric charge, which is proportional to the surface concentration of active sites [6,9].

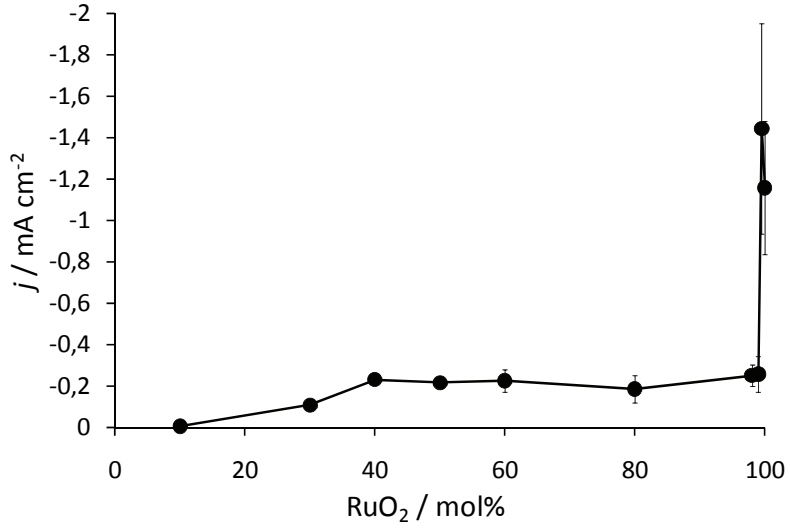

Figure 5.14 Observed current density, *j*, at *E* = -300 mV(SCE) as a function of composition.

The current density, *j*, normalized to unit surface area, *q**, is plotted as a function of composition (Figure 5.15). The normalized activity is low for electrodes with less than 60 mol% RuO_2, and then it starts to increase. The activity is highest for electrodes at 99-99.5 mol% RuO_2 and it is significantly lower for pure RuO_2. Thus, true electrocatalytic effects appear to be operating only for electrodes with RuO_2 content between 80 and 99.5 mol%.

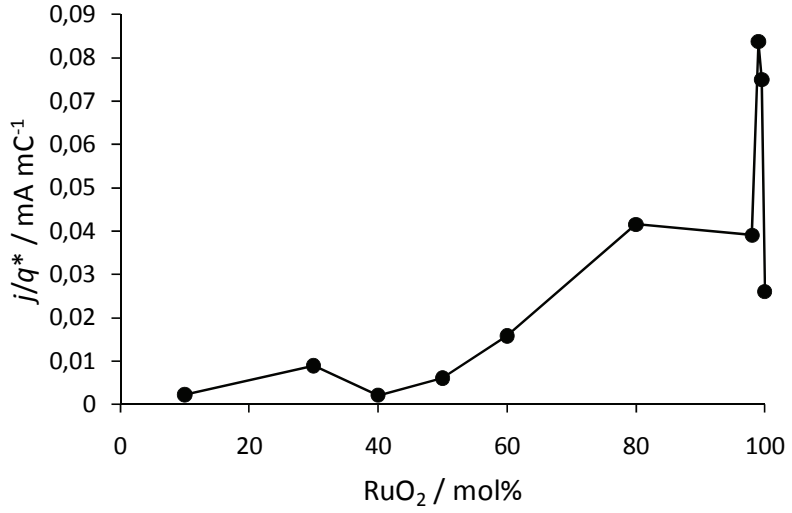

Figure 5.15 Normalized current density, *j*/*q, as a function of composition.**

In Figure 5.16, the overpotential at *I*=-70 mA is reported as a function of composition. The lower overpotentials were observed for electrodes at 40, 99.5 and 100 mol% RuO_2. As already discussed in the case of current density, electrode at 10 mol% RuO_2 is not suitable towards H_2 evolution reaction, because of negligible current and unfavorable overpotential.

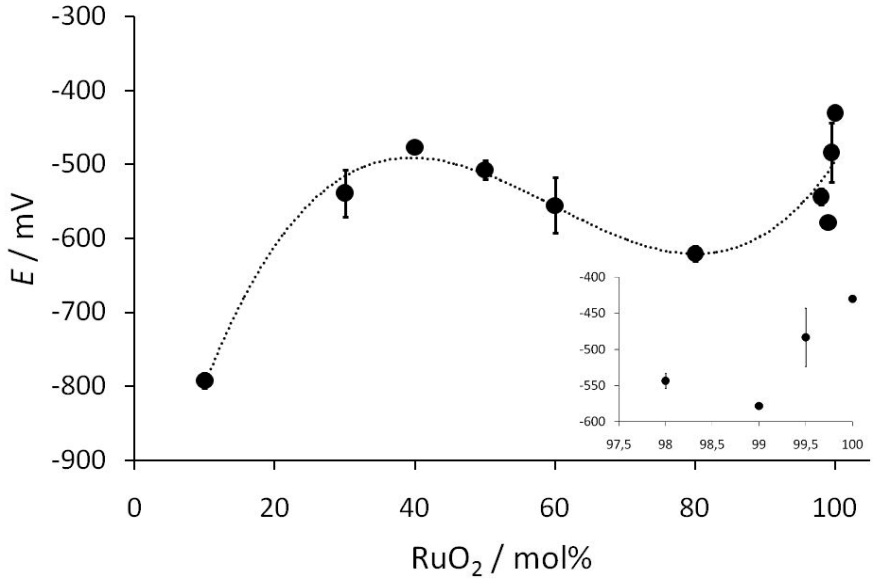

Figure 5.16 Overpotential for H_2 evolution at *I* = -70 mA from 0.5 mol dm^{-3} $HClO_4$ solution as a function of composition.

5.3.8 Stability

Figure 5.17 shows the evolution of voltammetric curves after cathodic polarization experiments. Some modifications are clearly visible in the shape of the curves.

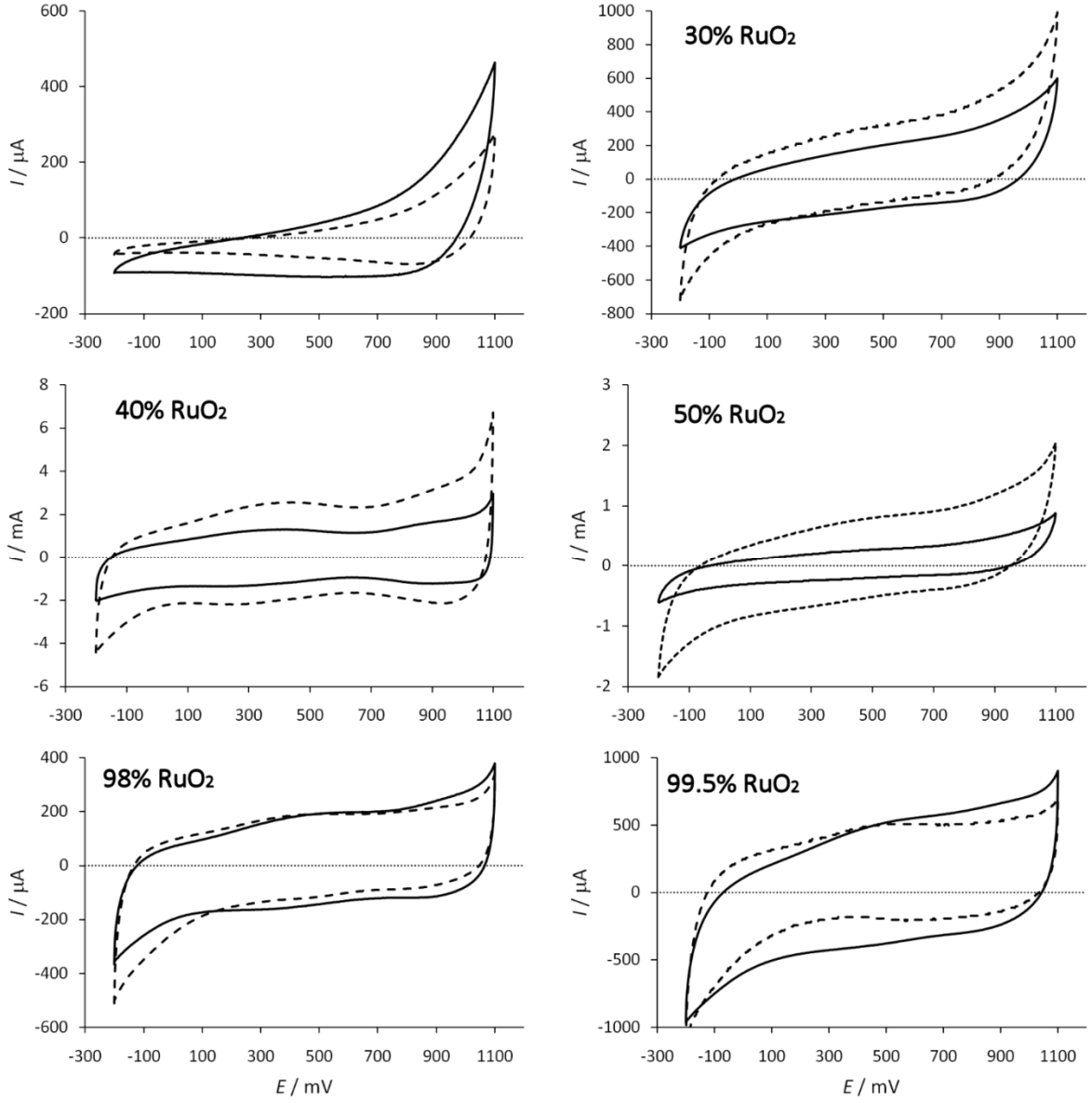

Figure 5.17 Cyclic voltammetric curves at 20 mV s-1 in 0.5 mol dm^{-3} $HClO_4$ solution on (RuO_2+NiO_x) mixed oxide electrodes of different compositions. (—) Fresh electrodes; (- - -) After first cathodic polarization run.

Comparison of voltammetric charge before and after the first polarization run is provided in Figure 5.18 and Figure 5.19. After the first cathodic polarization run, the charge greatly decrease for electrodes 0 and 10 mol% RuO_2, increases up to 3 times for 30-60 mol% RuO_2, is quite stable for 80 and 98 mol% RuO_2 and slightly decreases for 99-100 mol% RuO_2. The variation of voltammetric charge after polarization points to a great instability of

electrode with high NiO_x content. This instability adds to the considerations drawn about resistance, *R*, at high percentages of NiO_x.

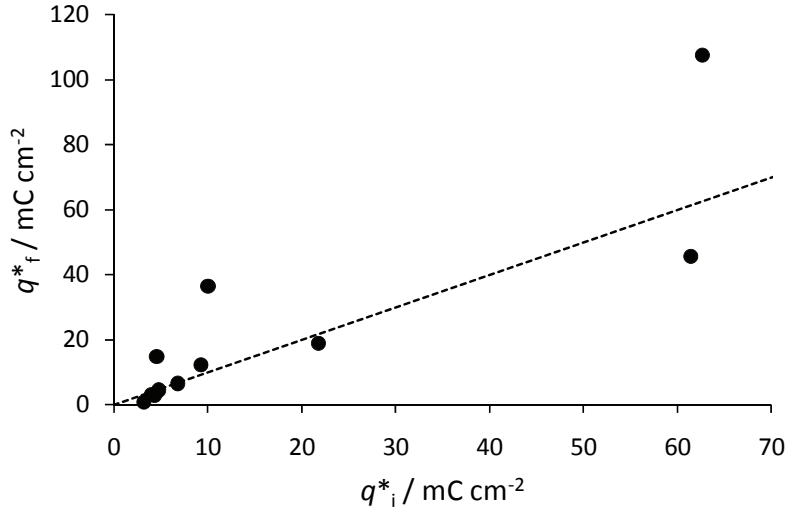

Figure 5.18 Voltammetric charge for fresh sample (q^*_i) plotted against voltammetric charge after the first cathodic polarization (q^*_f). (···) Straight line of unit slope.

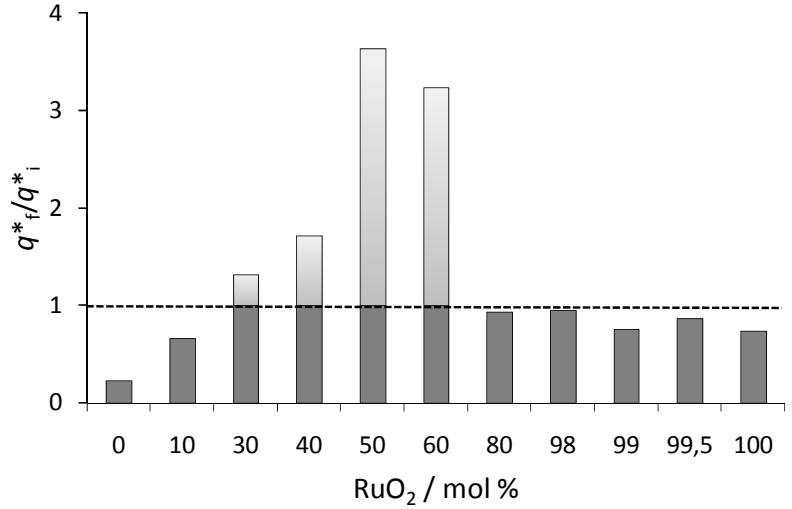

Figure 5.19 Ratio of voltammetric charge after (q^*_f) vs. before (q^*_i) H2 evolution as a function of composition.

If q^* after the first polarization curve is compared with q^* after the second polarization (Figure 5.20), electrode surfaces appear to be satisfactorily stable. Therefore, after an initial physical rearrangement H_2 evolution does not produce further modifications. This is a hint for surface stability.

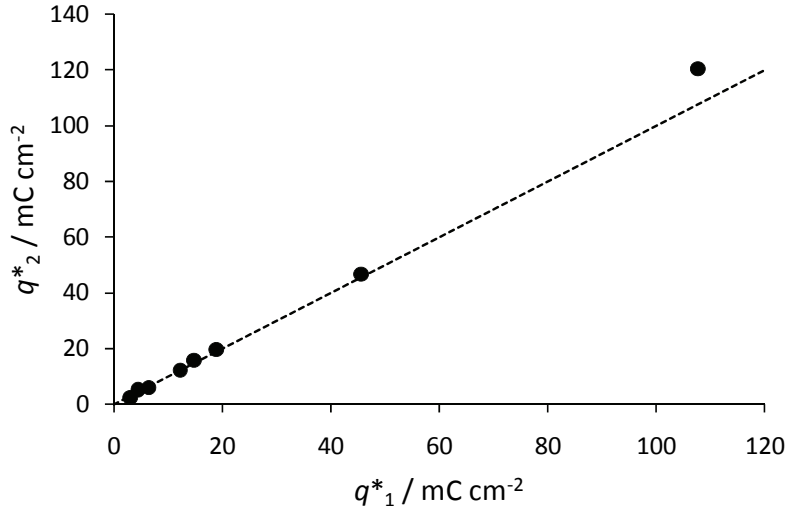

Figure 5.20 Voltammetric charge for sample after the second polarization (q^*_2) plotted against voltammetric charge after the first cathodic (q^*_1). (···) Straight line of unit slope.

5.4 Conclusions

- The addition of small amounts of NiO_x to RuO_2 distorts the crystalline lattice of RuO_2 and modifies its electrocatalytic properties.
- As expected, NiO_x is not stable in the acidic media used for electrochemical experiments.
- The process of H_2 evolution proceeds with low Tafel slope for RuO_2 content higher than 10 mol%. The Tafel slope decreases from about 40 to about 30 mV as the RuO_2 content increases.
- Electrodes need an activation pretreatment. However, after an initial rearrangement, electrode surfaces appear to be stable toward H_2 evolution reaction.
- Electrodes at 80-98 mol% RuO_2 exhibit better electrocatalytic performance than pure RuO_2.

5.5 References

[1] S. Trasatti, G. Lodi, in: S. Trasatti (Ed.), Electrodes of Conductive Metallic Oxides, Part A, Elsevier, Amsterdam, 1980, pp. 301-358.

[2] K. Macounova, M. Makarova, J. Jirkovsky, J. Franc, P. Krtil, Electrochimica Acta 53 (2008) 6126-6134.

[3] L.L. Hench, J.K. West, Chemical Reviews 90 (1990) 33-72.

[4] A. Vioux, Chemistry of Materials 9 (1997) 2292-2299.

[5] S. Music, S. Popovic, M. Maljkovic, K. Furic, A. Gajovic, Materials Letters 56 (2002) 806-811.

[6] S. Trasatti, Electrochimica Acta 36 (1991) 225-241.

[7] N. Krstajic, S. Trasatti, Journal of The Electrochemical Society 142 (1995) 2675.

[8] C. Angelinetta, M. Falciola, S. Trasatti, Journal of Electroanalytical Chemistry 205 (1986) 347-353.

[9] S. Trasatti, in: J. Lipkowski, P.N. Ross (Eds.), The Electrochemistry Of Novel Materials, VCH, New York, 1994.

Chapter 6. RuO_2 electrodes: laser and ion bombardment modifications

6.1 Introduction

Oxygen evolution reaction (OER) taking place on the surfaces of RuO_2, IrO_2, and other oxides is the object of continuous investigations due to its importance in electrolysis and energy conversion technologies. The results discussed in the present chapter were published in *The Journal of Chemical Science* [1].

The activity of RuO_2 has been attributed to both electronic and geometric effects. The latter are related to the high surface area as a consequence of the procedure of preparation of oxide materials. The former are attributed to the capacity of transition metals to exist in several valency states so that electron exchange with the environment is possible at several different redox potential levels [2]. Deeper investigations of the properties of RuO_2 layer electrodes have shown that electronic and geometric factors are interrelated as the size of the oxide particles decreases. More specifically, as the surface area increases the mechanism of electrode reactions changes. The reason of this behaviour is the formation of particularly active sites at the surface of smaller crystallites and defective regions of oxide particles [3].

Such sites can be also promoted on the surface of normal-sized crystallites by surface modification with specific treatments. Experiments of irradiaton with γ-rays were carried out several times in catalysis [4,5] and sometimes in electrochemistry [6]. Different behaviours in catalytic activity was reported depending on specific conditions.

Treatments with laser beams and ion implantation appear more decisive. In the former case the solid surface is subjected to intense heating. The effects of laser irradiation depend on the nature of the material as well as on the conditions of laser treatment [7,8]. In the case of ion implantation, the surface is subjected to mechanical damage, which can simulate the formation of very small particles [9].

In the specific case of RuO_2 electrodes experiments with γ-rays have not been conclusive to gain insight into the electrocatalytic properties [8]. On the other hand, preliminary experiments with laser and ion implantation were carried out long ago by Lodi and Trasatti [10], anticipating promising results that were not pursued further immediately.

Since then, there were very few attempts with RuO_2. Actually laser was used as a source of heat to obtain the oxide from the precursor more quickly than with a standard procedure of thermal decomposition [11], but never (to the best of our knowledge) to modify pre-formed RuO_2 electrodes.

In the case of ion implantation, there has been only one attempt thus far (to the best of our knowledge) to treat pre-formed RuO_2 electrodes [12]. The results reported cannot however be considered as conclusive for two main reasons. *(i)* Metallic ions were implanted with the creation of mechanical damages but implanted ions can become also active sites themselves; *(ii)* An accurate physical analysis of the fate of implanted ions was carried out, but the electrochemical analysis has been very qualitative. Any mechanistic discussion was provided neither attempt at the separation of electronic effects from geometric effects.

In the above context, more extensive investigations were carried starting from preliminary experiments. RuO_2 layers on Ti, obtained by thermal decomposition, were treated separately with a laser beam and ion implantation. Since the aim was to obtain surface defects only and to avoid implantation of foreign metal ions, RuO_2 was bombarded with krypton.

6.2 Experimental

6.2.1 Electrodes

RuO_2 thin layers were prepared by thermal decomposition of Ru nitrate onto a Ti support (platelets of 5×5 mm size). The support was previously etched in boiling oxalic acid for 1 hour. The precursor was dissolved in isopropanol and the solution brushed onto the Ti platelet. The solvent was evaporated at about 80 °C in air and the electrode calcinated in a pre-heated oven for 10 minutes at 400 °C. After cooling, the RuO_2 layer was gently scraped with filter paper to remove loose particles and cleaned up ultrasonically. This procedure was then repeated until an amount of about 1 mg cm^{-2} was attained.

Twelve samples were prepared and fresh electrodes were characterized by cyclic voltammetry before subjecting to the surface treatments. Six of these electrodes were then selected for further experiments. The choice was simply based on the closest similarity of physical and electrochemical features. Two electrodes were subjected to implantation, three to laser irradiation, while the sixth sample was used as such to constitute a reference standard.

6.2.2 Surface treatments

Surface treatments were carried out in the National Laboratories of the National Institute of Nuclear Physics (INFN) at Legnaro (Padua, Italy). The energy of laser radiation

was varied from 0.5, to 1.5, to 2.5 J cm^{-2} for the three electrodes used. Surface bombardment was operated with a beam of Krypton in a 200 KeV implantation apparatus. The dose of atom implantation was 10^{15} and 10^{16} cm^{-2}, respectively, for the two electrodes used. After the treatment, the samples of both kind were used as such for characterization by cyclic voltammetry.

6.2.3 Electrochemical experiments

All electrochemical experiments were performed in 0.5 mol dm^{-3} H_2SO_4 aqueous solutions at 25±0.1 °C in a water thermostat. Solutions were deareated by bubbling purified N_2 for not less than ½ hour before experiments.

All experiments were carried out using a Mod. 553 AMEL potentiostat/galvanostat equipped with a Mod. 667 AMEL electrometer for the measurement of electrode potentials, and a Mod. 863 AMEL X-Y recorder. The four-compartments electrochemical cell contained two Pt counterelectrodes separated from the central compartment of the working electrode by glass frits. The compartment of the reference electrode was connected to the surface of the working electrode via a Luggin capillary. Electrode potentials were read and are reported against a hydrogen electrode in the same solution (RHE).

Voltammetric curves were recorded at 20 mV s^{-1} in the potential range between 0.4 and 1.4 V (RHE). Voltammetric charges were obtained by graphical integration of the voltammetric curves.

Quasi-stationary potentiostatic curves were recorded between 1.30 and 1.60 V (RHE) by moving the potential by 20 mV steps and reading the current after 2 min at each potential (forward scan). At 1.60 V the direction of potential scan was reversed and experiments continued until the current became cathodic (backward scan).

The reaction order with respect to H^+ for the anodic O_2 evolution was determined by recording polarization curves at different concentrations of H_2SO_4 (0.05, 0.1, 0.2, 0.3, 0.4, 0.5 mol dm^{-3}). The ionic strength was kept constant by addition of Na_2SO_4. The order of reaction was derived from plots of log *j* (current density) at 1.46V (RHE) *vs.* pH. The value of potential was selected so as to lie on the linear section of the polarization curves.

6.3 Results

6.3.1 Voltammetric curves

Voltammetric curves were recorded for fresh samples, for samples after surface treatments, for samples after O_2 evolution polarization curves, and for samples after determination of the reaction order with respect to H^+.

In Figure 6.1 and Figure 6.2 typical voltammetric curves of RuO_2 electrodes [13] are shown. Both surface treatments enhance the current without changing the shape of the curves substantially. This suggests that the nature of surface redox transitions is not affected by the surface treatments. Nevertheless, in the case of atom implantation (Figure 6.2), the enhancement observable at E higher than 1.2 V indicates higher electrocatalytic activity for anodic reactions. This is much less evident in the case of laser treatment (Figure 6.1).

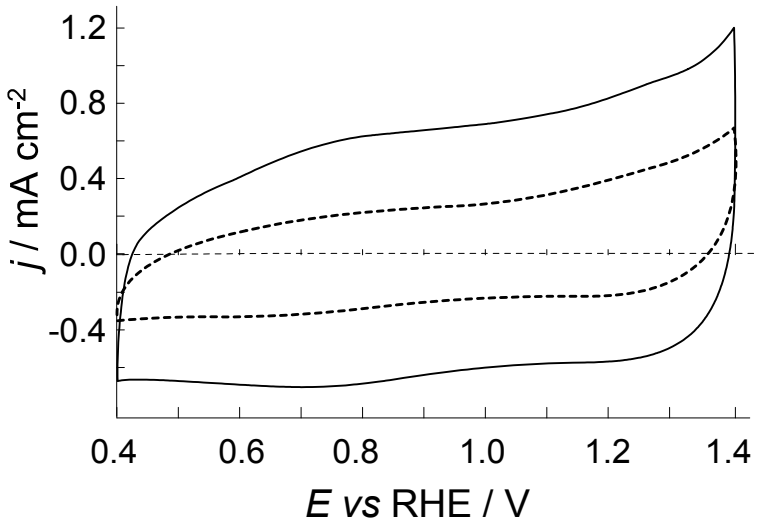

Figure 6.1 Representative cyclic voltammetric curves of RuO_2 electrodes in 0.5 mol dm^{-3} H_2SO_4 aqueous solution. Same sample: before (- - -) and after laser irradiation (—).

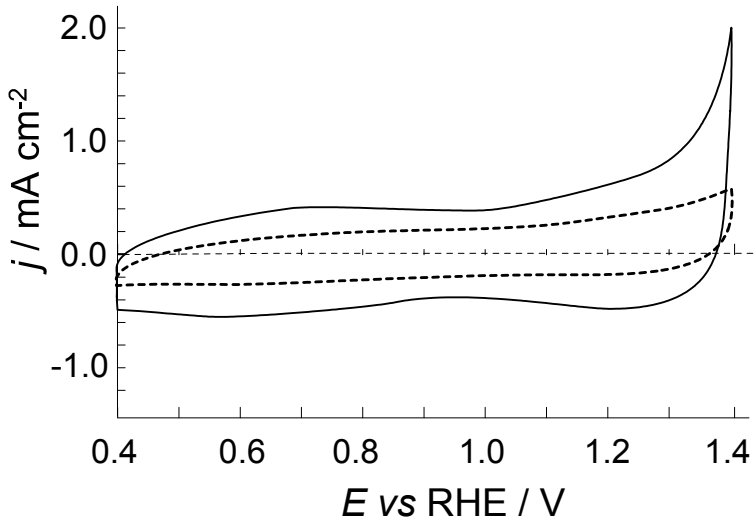

Figure 6.2 Representative cyclic voltammetric curves of RuO_2 electrodes in 0.5 mol dm^{-3} H_2SO_4 aqueous solution. Same sample: before (- - -) and after Kr bombardment (—).

6.3.2 Voltammetric charge

Integration of the voltammetric curves gives the surface charge spent in redox transitions. For RuO_2, the voltammetric charge, q^*, is a measure of the number of proton exchanged between the solution and the oxide surface, on the basis of the following equation [2]:

$$\mathrm{RuO}_x(\mathrm{OH})_y + \delta\mathrm{H}^+ + \delta e \rightarrow \mathrm{RuO}_{x-\delta}(\mathrm{OH})_{y+\delta} \tag{6.1}$$

Equation (6.1) shows that the voltammetric charge, q^*, measures the amount of protons exchanged between the oxide surface and the aqueous solution. Thus, q^*, is proportional to the surface concentration of active sites, i.e. to the actual active surface area.

Since different fresh electrodes were used for different doses of surface treatments, the most convenient way to monitor the effect of treatments on surface charge is to normalize the variation of q^* after the treatment with respect to the fresh surface. Figure 6.3 shows the variation of $(\Delta q^*/q_b^*)\times 100$ as a function of laser treatment. The subscript "b" stands for "blank". The surface charge is seen to increase dramatically with the intensity of the treatment, levelling off at higher intensity. Quantitatively the surface charge increases by more than two times.

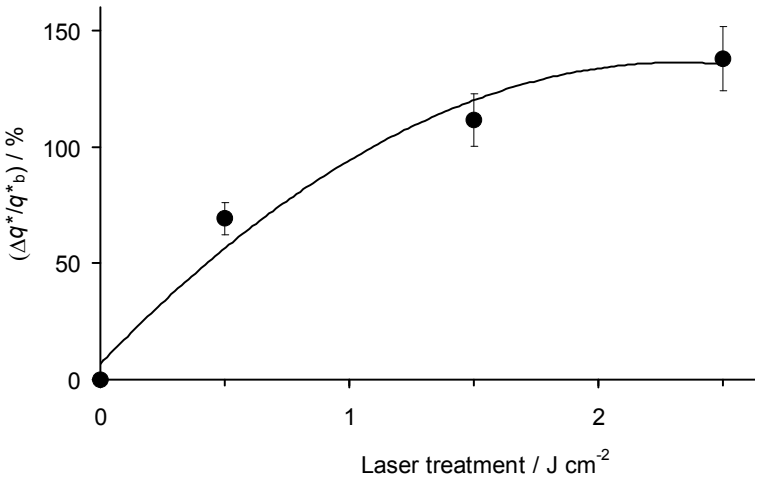

Figure 6.3 Increment of voltammetric charge relative to the pristine surface state as a consequence of laser irradiation.

The surface charge is seen to increase also in the case of atom bombardment. Quantitative data are not reported in a graph for two reasons: *i)* The number of samples is small, and *ii)* the increase is not monotonic, exhibiting a maximum for the lower dose. At any rate, the highest value of Δq^* is comparable for the two surface treatment procedures.

Increase in q^* can be originated by a higher concentration of surface active sites. Nevertheless, laser treatment and atom bombardment are not expected to produce similar physical and mechanical effects on an oxide surface. A laser beam produces a local intense heating whose effect on a crystalline solid should be amorphization. The latter, however, should result in decrease of surface charge as in the case of melting of a rough solid surface. It is also possible to consider that oxides produced by thermal decomposition are poorly crystalline and a heating pulse could induce crystallization. The high intensity of the beam much probably causes a violent thermal shock with formation of surface micro-cracks [8]. As a consequence, the number of surface sites accessible to the solution increases.

The interpretation of the data obtained with atom implantation is more straightforward. The surface bombardment has a strong mechanical effect with breakage of micro-crystallites and formation of nanosized surface defects [12]. Though the final effect is a sizeable increase in surface charge as in the case of laser irradiation, however the nature of the surface sites created by the two surface treatments turns out to be different.

6.3.3 Polarization curves

In Figure 6.4, typical quasi-stationary current-potential curves for O_2 evolution on fresh *vs.* atom-implanted electrodes are reported. The experimental data have not been

corrected for ohmic drop effects. Nevertheless, a linear portion of the curves (Tafel region) can easily be identified. The current at constant potential is enhanced as an effect of atom bombardment. The Tafel slope changes with surface treatment. This behaviour clearly suggests that the increased activity is not attributable to surface area effects (geometric factors) only. Since the Tafel slope is an intensive quantity, it depends on the reaction mechanism only and not on geometric factors.

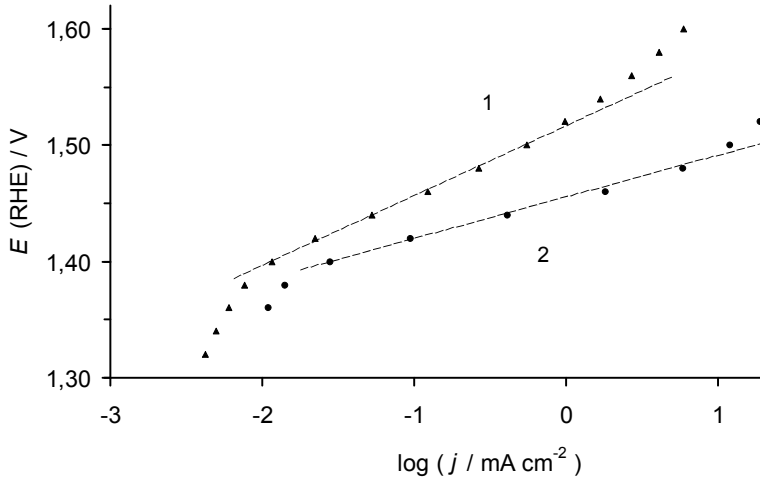

Figure 6.4 Current-potential potentiostatic curves for O_2 evolution on RuO_2 electrodes in 0.5 mol dm^{-3} H_2SO_4 aqueous solution. (1) Fresh electrode before surface treatment; (2) After Kr bombardment with a dose of 10^{16} cm^{-2}

6.3.4 Tafel slopes

The effect of laser irradiation on the Tafel slope for O_2 evolution is shown in Figure 6.5. For the fresh electrode the Tafel slope is around 60 mV, decreasing with laser treatment. The decrease of the Tafel slope levels off at higher laser intensity, clearly showing parallelism with the behaviour of the surface charge in Figure 6.3. This suggests that the origin of the variation of q^* is the same as for the change in b, although geometric factors are involved in the former case, and electronic factors in the latter.

A quite similar picture of b vs. surface treatment is observed with atom bombardment, as shown in Figure 6.6. There are however two notable differences: *(i)* The decrease in b is monotonic, differently from q^*, and *(ii)* the Tafel slope decreases more appreciably than in the case of laser treatment. This indicates that for atom implantation electronic effects prevail over geometric effects.

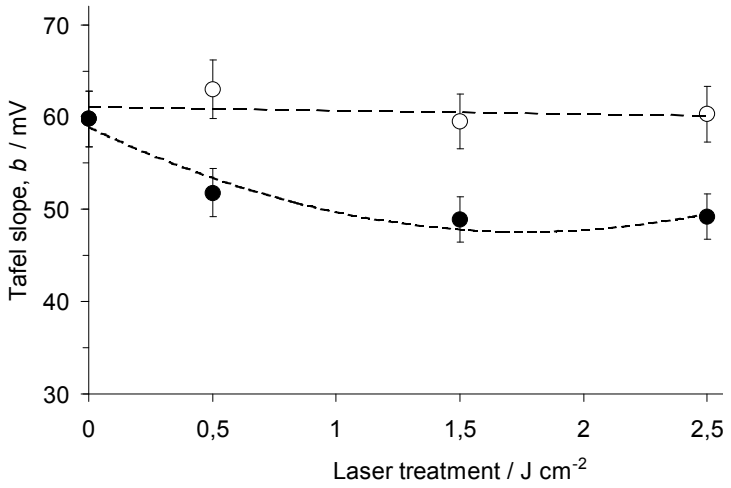

Figure 6.5 Tafel slope for O_2 evolution on RuO_2 electrodes as a function of laser irradiation. (○) Before treatment; (●) After treatment.

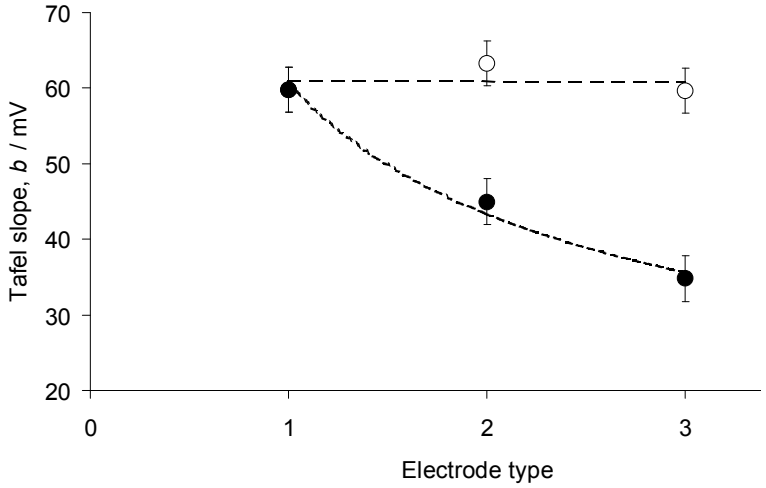

Figure 6.6 Tafel slope for O_2 evolution on RuO_2 electrodes as a function of Kr bombardment. (1) Untreated (blank) sample. Kr dose: (2) 10^{15} cm^{-2}; (3) 10^{16} cm^{-2}. (○) Before treatment; (●) After treatment.

6.3.5 Reaction order

Figure 6.7 shows a typical plot of log *j vs.* pH to obtain the reaction order with respect to H^+ (β_{H^+}). The experimental points are well aligned with correlation coefficients around 0.99. This indicates that eventual variations of reaction order by more than 0.1 are real. Since both Tafel slope and reaction order depend on the reaction mechanism, a correlation is expected between the two quantities. This is confirmed by the plot in Figure 6.8, showing *b vs.* β_{H^+}. While *b* varies from 60 mV to less than 40mV, the reaction order changes from *ca.* 1 to *ca.* 1.7.

Fractional reaction orders are not chemically significant since they include double layer effects [14]. In the case of oxide electrodes, as pH is changed to determine the reaction rate as a function of pH, the surface charge is modified because of the specific mechanism of surface charging. The latter is the origin of double layer effects. These aspects have been exhaustively discussed by Trasatti [15,16]. Therefore, the picture in Figure 6.8 is in line with the known behaviour of oxide surfaces and the plot possesses full significance.

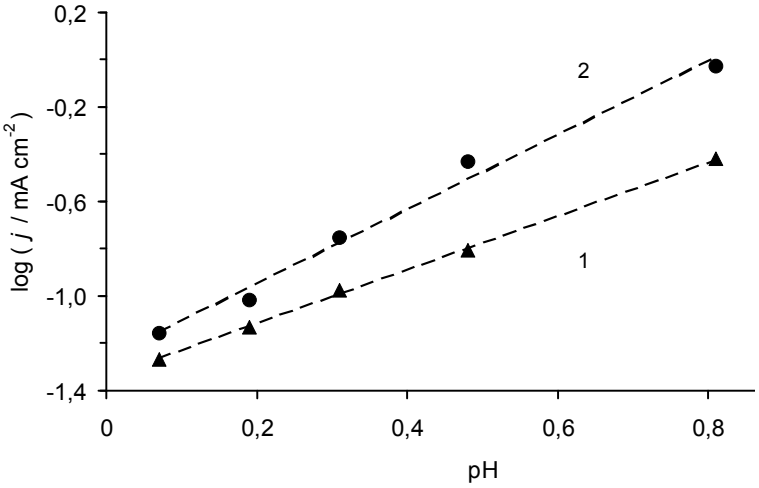

Figure 6.7 Typical plots of log *j* (at 1.46V) vs. pH for the determination of the reaction order of O_2 evolution. Surface treatment: (1) laser irradiation, 0.5 J cm^{-2}; (2) Kr bombardment, 10^{16} cm^{-2}.

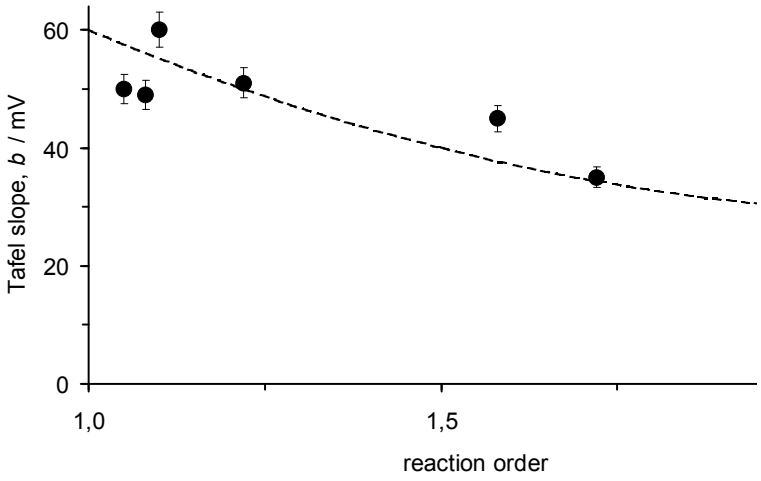

Figure 6.8 Graphical correlation between Tafel slope and reaction order for O_2 evolution.

6.4 Discussion

6.4.1 Reaction mechanism

The Tafel slope for blank RuO_2 (*ca.* 60 mV) is in agreement with previous work [17].

The Tafel slope for O_2 evolution has been found to vary from 30 mV for nanocrystalline surfaces up to 60 mV for the (110) face of single crystals [3,18]. The 60 mV of this work indicates that blank fresh electrodes possess rather smooth surfaces with a small number of surface defects. Surface treatments increase the number of surface defects that offer more active surface sites. As a consequence the Tafel slope decreases and the apparent current density increases.

For O_2 evolution on oxide electrodes, a generalized mechanism proposed by Trasatti has already been discussed in Chapter 2 [19]:

$$\text{–S-OH} + H_2O \rightarrow \text{–S-OH(OH)*} + H^+ + e \tag{6.2}$$

where –S-OH is a surface active site, and OH* is an unstable intermediate readily converted into a more suitable species (spillover):

$$\text{–S-OH(OH)*} \rightarrow \text{–S-OH(OH)} \tag{6.3}$$

The surface complex is then further oxidized:

$$\text{–S-OH(OH)} \rightarrow \text{–S-OH(O)} + H^+ + e \tag{6.4}$$

or, alternatively, two adjacent surface complexes recombine:

$$\text{–S-OH(OH)} + \text{–S-OH(OH)} \rightarrow 2 - \text{S-OH(O)} + H_2O \tag{6.5}$$

Finally, the surface species formed in (6.4) or (6.5) decomposes releasing gaseous O_2:

$$\text{–S-OH(O)} + \text{–S-OH(O)} \rightarrow 2 - \text{S-OH} + O_2 \tag{6.6}$$

According to the data in Figure 6.8, step (6.3) prevails as a rate determining step on blank RuO_2, step (6.4) on laser treated RuO_2, and step (6.5) on atom implanted RuO_2. The variable that changes with surface treatments is in the end the heat of adsorption of oxygenated intermediates on the electrode surface [20]. The heat of adsorption depends in turn on the nature of the surface active site. The experimental picture points to an increment of the electrode-intermediate bond strength as surface defects change from the blank electrode to laser and finally to implantation treatment. In other words, surface treatments promote real electrocatalytic effects, and atom implantation is more effective than laser irradiation.

6.4.2 Electrocatalytic activity

Unquestionable evidence of real electrocatalysis (electronic effects) can be obtained by eliminating geometric effects related to variations in surface area. This can be achieved either *i)* by resorting to intensive quantities or *ii)* by allowing for surface area effects in extensive quantities.

Scrutiny of experimental data based on approach *i)* above has been performed in the

previous sections. In this section analysis will be made of the apparent current density (the apparent reaction rate) that by its nature is an extensive quantity, *i.e.*, it depends straightforwardly on the extension of the surface area.

Figure 6.9 shows a plot of the apparent reaction rate (at 1.46 V) as a function of the nature of the electrode, a non-quantitative variable. It is evident that the reaction rate increases with laser irradiation and more with atom implantation. However, the increment does not vary appreciably with laser treatment, whereas rises sharply with implantation.

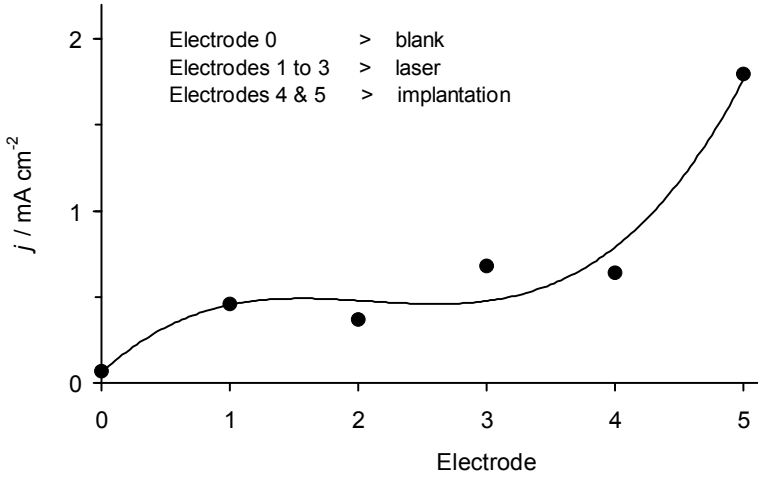

Figure 6.9 Current density for O_2 evolution vs. the kind of surface treatment. (○) Blank; (1, 2, 3) laser irradiation, increasing dose; (4, 5) Kr bombardment, increasing dose.

The data in Figure 6.9 encompass both electronic and geometric effects and cannot be used to conclude about electrocatalytic effects. Nevertheless, the activity of electrocatalysts is mostly discussed in the literature on the very basis of raw reaction rate data.

Oxide electrodes offer the possibility of allowing for surface area effects on the basis of the voltammetric charge, q^* [21]. Figure 6.10 shows a plot of the relative increment in reaction rate at 1.46 V against the relative increment in surface charge. If only surface area effects were operating, doubling of q^* would result in doubling of j. Therefore, pure surface area effects would produce experimental points lying on a straight line (of unit slope in case relative increments are plotted - the dashed line in Figure 6.10). On the contrary, all electrodes after surface treatments give points lying away from the straight line, more specifically above, i.e. the reaction rate increases more than expected on the basis of geometric effects only.

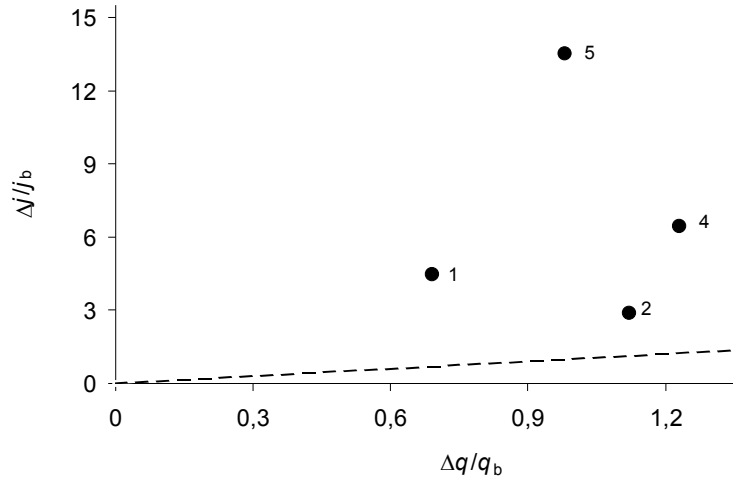

Figure 6.10 Relative increment of current density for O_2 evolution at 1.46 V vs. the relative increment of voltammetric charge. Subscript "b" stands for "blank". (1) Blank electrode; (1, 2, 3) Laser irradiation, increasing dose; (4, 5) Kr bombardment, increasing dose.

The data in Figure 6.10 points to true electrocatalytic effects for all electrodes, but while these are moderate and substantially constant for laser irradiation, they are stronger and dependent on the dose of implanted species for atom implantation. This confirms once more that atom implantation gives rise to more active surface sites than laser irradiation.

6.5 Conclusions

- Both laser irradiation and atom bombardment enhance the apparent electrochemical activity of RuO_2 electrodes.
- Geometric effects can be assessed on the basis of the voltammetric charge, assumed to be proportional to the surface concentration of active sites. Electronic effects can be assessed on the basis of the Tafel slope for O_2 evolution (an intensive quantity), as well as of correlations between current density and voltammetric charge. The latter depends only on geometric factors, the former on both geometric and electronic factors.
- Scrutiny of the experimental data reveals that most of the apparent activity enhancement is related to electronic factors. Geometric factors lead to double the activity at most.
- Both surface treatments enhance the true electrocatalytic activity, but the enhancement is definitely higher for atom bombardment.
- Atom bombardment is presumed to stimulate the exposition of particularly active sites as a consequence of the fracture of RuO_2 crystallites.

– Laser irradiation is thought to cause rapid crystallization leading to some disorder in the crystallites accompanied by cracking due to violent heating.

6.6 References

[1] E. Guerrini, A. Colombo, S. Trasatti, Journal of Chemical Sciences 121 (2009) 639-646.

[2] S. Trasatti, in: A. Wieckowski (Ed.), Interfacial Electrochemistry: Theory, Practice and Applications., Marcel Dekker, New York, 1999, pp. 769-792.

[3] E. Guerrini, S. Trasatti, Russian Journal of Electrochemistry 42 (2006) 1017-1025.

[4] G.A. El-Shobaky, S.A. Ismail, S.A. El-Molla, Journal of Radioanalytical and Nuclear Chemistry 260 (2004) 627-636.

[5] V. Mucka, E. Baburek, Radiation Physics and Chemistry 53 (1998) 483-489.

[6] I. Rousar, V. Cezner, R. Mraz, V. Srb, S. Zitek, B. Stverak, Electrochimica Acta 23 (1978) 763-765.

[7] F.A. Chudnovskii, A.L. Pergament, D.A. Schaefer, G.B. Stefanovich, Journal of Solid State Chemistry 118 (1995) 417-418.

[8] A.K. Upadhyay, H.M. Urbassek, Journal Of Physics D: Applied Physics 38 (2005) 2933-2941.

[9] H. Jin, X. Zhou, L. Zhang, Journal of Rare Earths 25 (2007) 63 - 67.

[10] G. Lodi, S. Trasatti, Unpublished Results.

[11] R.L. Pelegrino, C. Vicentin, A.R.D. Andrade, R. Bertazzoli, Electrochemistry Communications 4 (2002) 139-142.

[12] A. Tsujiko, K. Kajiyama, M. Kanaya, K. Murakoshi, Y. Nakato, Bulletin of the Chemical Society Of Japan 76 (2003) 1285-1290.

[13] S. Trasatti, G. Buzzanca, Journal of Electroanalytical Chemistry 29 (1971) A1-A5.

[14] S. Ardizzone, A. Carugati, G. Lodi, S. Trasatti, Journal of The Electrochemical Society 129 (1982) 1689-1693.

[15] A. Carugati, G. Lodi, S. Trasatti, Materials Chemistry 6 (1981) 255- 266.

[16] C. Angelinetta, M. Falciola, S. Trasatti, Journal of Electroanalytical Chemistry 205 (1986) 347-353.

[17] P. Castelli, S. Trasatti, F.H. Pollak, W.E. O'Grady, Journal of Electroanalytical Chemistry 210 (1986) 189-194.

[18] S. Trasatti, in: J. Lipkowski, P.N. Ross (Eds.), The Electrochemistry of Novel Materials, VCH, New York, 1994.

[19] S. Trasatti, in: H. Wendt (Ed.), Electrochemical Hydrogen Technologies, Elsevier, Amsterdam, 1990, p. 104.

[20] S. Trasatti, Journal of Electroanalytical Chemistry 111 (1980) 125-131.

[21] S. Trasatti, Electrochimica Acta 29 (1984) 1503-1512.

Chapter 7. Nanoparticles of transition metal oxides: a novel synthesis

7.1 Introduction

Oxides prepared by thermal decomposition show a micro-porous structure, with nanocrystallites separated by grain boundaries. A main goal in electrocatalysis is to maximize the surface area available for reactions. A way to achieve this goal is to reduce the particle size down to nanometer dimensions, thus enhancing the area/volume ratio and promoting the formation of new particularly active surface sites. As previously said in Chapter 6, synthetic routes in non-aqueous media provide a promising approach to produce metal oxide nanoparticles.

Metal nanoparticles – and nanoparticles in general – gained much attention in the last decade. Usually materials with nanometric dimensions (typically 1 to 100 nm) are defined as nanostructured. Strictly speaking, nanoparticles must show unique chemical [1,2], physical [3-5] or electronic properties [6], different from those of bulk materials.

Research in this field is worldwide supported by governmental funding. A lot of work is currently being performed on synthesis, characterization and improvement of properties. Main goals are: i) control of size, shape and composition, ii) prevent decomposition and agglomeration by stabilization of the products.

The determination of the electrochemical properties of supported oxide nanoparticles is of great interest in both fundamental and applied research. In fact they can exhibit different and sometimes novel properties compared with bulk materials. This consideration is the basis of recent researches on the electrochemical properties of nanoparticles of IrO_2 and RuO_2 [7-11]. If size- and shape-controlled syntheses are desired, as in the case of nanoparticles, sol-gel routes are more promising then thermal decomposition. Sol-gel routes have thus been applied to produce nanostructured oxides for electrocatalysis. However many crystal structures are not accessible *via* such a method.

In contrast to the traditional high temperature of conventional thermal decomposition to metal oxides, the use of aqueous sol–gel chemistry allows to achieve higher compositional homogeneity and to influence the particle morphology during the chemical transformation of

the molecular precursor to the final oxidic network [12]. However, it turned out that a specific synthesis route, which worked well for the bulk oxide, cannot directly be adapted to its corresponding nanoparticles oxide. The reason lies in the fact that aqueous sol–gel chemistry typically leads to amorphous precipitates that are transformed into the desired crystalline material by applying a calcination step. This temperature treatment to induce crystallization is not a viable option for size- and shape-controlled nanoparticle synthesis, because the crystal growth cannot be controlled. Furthermore, aqueous sol-gel chemistry is rather complex. An aqueous sol-gel process [13] consists in the conversion of a metal organic precursor solution into an inorganic solid *via* polymerization reactions induced by water. Smaller particles are usually obtained. The main disadvantage is the control of the reaction rate. This is too fast for most transition metal oxide precursors, thus causing the loss of morphological and structural control over the final oxide material.

Nowadays attention is paid to innovative synthetic paths. Reduction in the number of steps and lower temperatures are desired. Since control of size and shape is greatly desired, non-aqueous processes seem more promising. These methods were applied in the last few years to synthesize several metal oxides. Nevertheless, looking at the literature, transition metal oxides applied to electrocatalytic water splitting (e.g., IrO_2 and RuO_2) have not yet been synthesized by these methods.

Non-aqueous sol-gel processes in organic solvents are a promising alternative [14,15]. They can overcome some of the limitations of the aqueous methods. Organic solvents act at the same time as solvents and as oxygen suppliers for the formation of the oxide. Furthermore, reaction rates are slower because of the moderate reactivity of oxygen-carbon bond. This allows better control of the reaction conditions. Solvent-directed processes just involve the reaction of metal oxide precursors with a common organic solvent and usually take place at lower temperatures (50–250°C). In most cases an organic polar solvent, like benzyl alcohol, works at the same time as solvent and as oxygen supplier for the formation of the oxidic compound. This method was deeply investigated by Niederberger for the synthesis of TiO_2 nanoparticles [14].

The main function of the organic species is to act as oxygen source for the oxide formation; however they are actively involved during all stages of particle growth and crystallization, strongly influencing the composition, size, shape, and surface properties of the nanocrystals. Another important advantage of non-aqueous sol–gel processes in comparison to aqueous systems is the accessibility of ternary, multi, and doped metal oxide nanoparticles [16]. The different reactivity of metal oxide precursors towards a specific solvent complicates

the synthesis of oxides containing two or more metals. In organic solvents it is easier to match the reactivity of the metal oxide precursors and of the dopants in comparison to aqueous systems.

Microwave irradiation applied to the synthesis of organic compounds works as heating tool, shortening reaction times [17]. Advantages are precise control of the temperature, fast thermal ramping, direct energy transfer, which discloses possible applications to inorganic chemistry and nanoparticle synthesis. Actually, since crystal size is highly dependent on reaction time and temperature, careful variation of the experimental conditions allows easier and versatile control of morphology, cristallinity and crystal phase of products.

The microwave processing of nanoparticles results in rapid heating of the reaction mixtures. As a consequence, the precipitation of particles tends to be rapid and nearly simultaneous. This leads to very small particle sizes and narrow size distributions within the products. The method offers the additional benefit of requiring very short reaction times [18].

Through the combination of non-aqueous processes with microwave irradiation, several metal oxide nanoparticles can be prepared with good yields in a reasonably short time range (30 sec. to 20 min.). The reduction of reaction time is considerable if compared to heating in oil bath or in autoclave (typical of sol-gel processes). By reaction of the corresponding metal alkoxides, acetates or acetylacetonates with benzyl alcohol, highly crystalline CoO, ZnO, Fe_3O_4, MnO, Mn_3O_4, and $BaTiO_3$ nanoparticles were obtained [19].

In the last part of this thesis the above non-aqueous approach was applied to produce nanoparticles of transition metal oxides for application in electrocatalytic water splitting. The feasibility of the method was firstly assessed for RuO_2. Following results come from preliminary experiments and represent an overview of the capabilities of this synthetic method.

7.2 RuO_2 nanoparticles

7.2.1 Synthesis

In non-aqueous processes the oxygen required for the formation of M-O-M bonds is not provided by any added water. Therefore, it must either come from the precursor or be provided by the organic medium. In fact, often these two cases cannot be clearly distinguished, and the mechanisms for this oxygen transfer are manifold. However, the key point is the formation of the oxygen bridges, which through further condensation reactions grow into larger 3D networks and thus build up the metal oxide nanostructures. A slow and

controlled progression of the condensation thereby ensures high crystallinity. Modulation of particle size can be achieved by different times of reaction.

The reactions between metal halides and alcohols are among the most utilized methods for the non-aqueous synthesis of metal oxide nanoparticles, because the large availability of metal halides and the low toxicity of alcohols, like benzyl alcohol. The oxygen of the alcohol is easily coordinated to the metal center of the precursor. The main expected mechanism is an alkyl halide elimination leading to metal hydroxyl species (equation (7.1)).

$$\equiv \text{M-X} + \text{R-OH} \rightarrow \text{M-OH} + \text{RX} \qquad (7.1)$$

In a typical synthesis, ~3 mmol of $RuCl_3$ were dissolved in 30 mL of benzyl alcohol under vigorous stirring at room temperature. The reaction was performed in an open vessel heated by an oil bath. The mixture was heated at 175 °C for 24 hours. After cooling, the resulting suspension was centrifuged and the precipitate was washed several times with ethanol and then dried at 60 °C in air. The resulting powder was finally milled in a agate mortar. The reaction was also performed in a closed vessel equipped with a reflux condenser. This experimental set-up allows more reproducible heating condition.

To avoid the effect of nucleation at the walls in the heated mixture, it was decided to perform the reaction under microwave irradiation. ~3 mmol of $RuCl_3$ were dissolved in 30 mL of benzyl alcohol under vigorous stirring at room temperature. The mixing of the precursor with the solvent was directly performed in the 45ml Teflon cups of the acid digestion bombs. The mixture was irradiated in a MLS 1200 Milestone microwave at 400W. Temperature of the mixture just after irradiation was about 150 °C. The resulting suspension was added with ethylic ether to help the separation from mother liquor and then centrifuged. Excess organic impurities were removed by repeated washing steps in 10 mL ethanol and subsequently dried in air at 60°C. The final material was then ground into a fine powder. Different times of irradiation were employed: 1, 3, 5, 15 min.

7.2.2 Characterization

In Figure 7.1 an example of the morphology of RuO_2 nanoparticles is shown. From SEM images, it is clearly visible that agglomeration occurs upon centrifugation. Subsequent SEM images showed that agglomerates are loosely attached and suspension in sonication brakes nanoparticles apart.

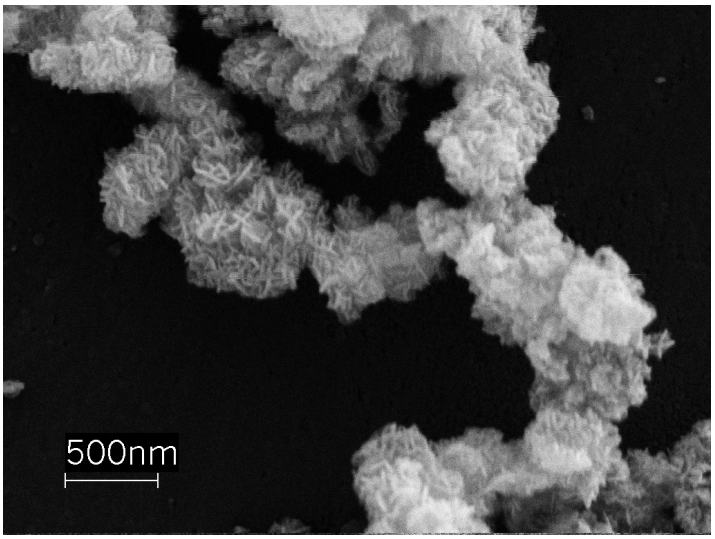

Figure 7.1 SEM image of RuO_2 nanoparticles obtained by the reaction of $RuCl_3$ with benzyl alcohol after 15 min of irradiation.

For the evaluation of the electrocatalytic activity of the nanosized materials, RuO_2 nanoparticles were suspended in 1:1 i-PrOH/H_2O mixture and deposited on Titanium platelets by air brushing or micropipette, up to a loading of 2 mg cm^{-2}. The resulting cyclic voltammetry showed the typical features of polycrystalline RuO_2 (Figure 7.2).

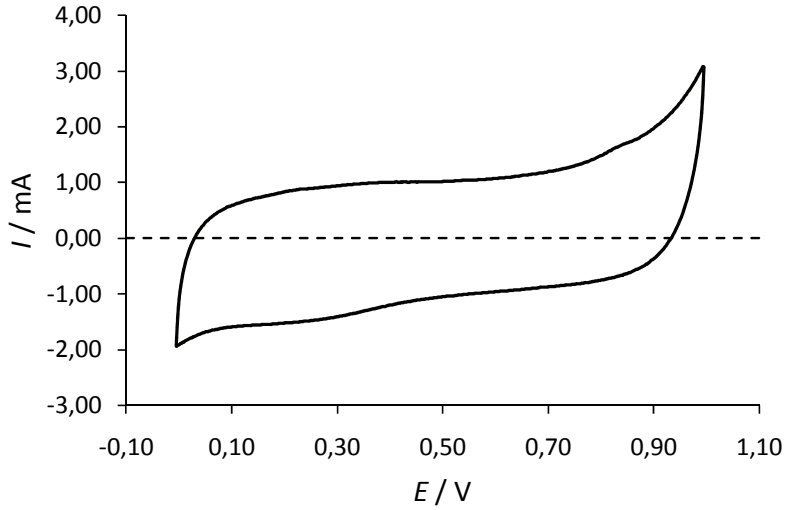

Figure 7.2 Typical voltammetric curves recorded on RuO_2 nanoparticles deposited on Ti.

Preliminary polarization experiments were performed in 0.5 mol dm^{-3} $HClO_4$. Tafel slope values close to 80 mV were obtained for nanoparticles obtained after 5 min irradiation. 40 mV Tafel slope were observed for nanoparticles obtained after 3 min irradiation.

7.3 Nanoparticles of other transition metal oxides

In some cases (e.g. RuO2 and $CuO_x(OH)_y$), precipitate formed immediately and resulting nanoparticles exhibited homogeneous sizes and shapes.

For other compounds, like $Co(OH)_xCl_y$, IrO_x, Fe_2O_3, the nucleation process continuously occurs during irradiation. Nucleation centers formed in the early step of the reaction can become bigger as the reaction proceeds, in the mean time others nucleation centers originated. Resulting particles exhibit non homogeneous sizes.

SEM images were acquired for all samples and showed that the morphology of nanoparticles varies as different precursors (nitrate, chloride) of the same cation are used. SEM micrographs of some samples are reported in the following. In the case of Cu oxide (Figure 7.6) and Co oxide from nitrate (Figure 7.4), SEM images shows rods and flakes together with smaller particles. This suggests that, after first nucleation, the growth of the particles occurs in preferential directions.

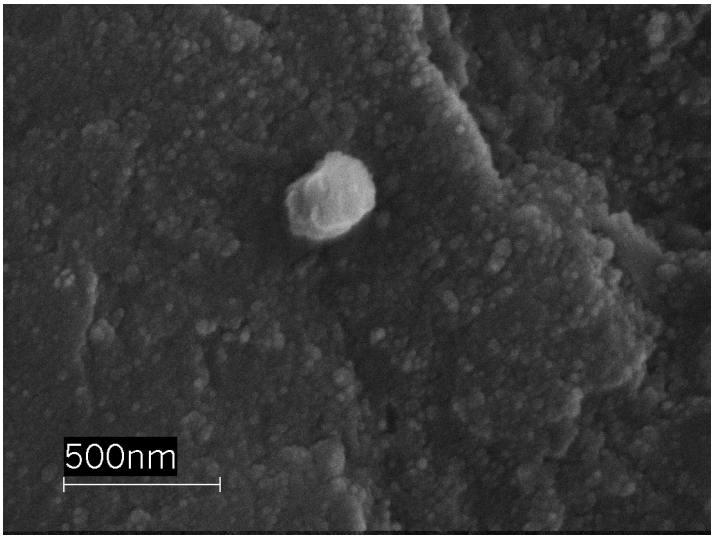

Figure 7.3 $CoO_x(OH)_y$ from $CoCl_2$

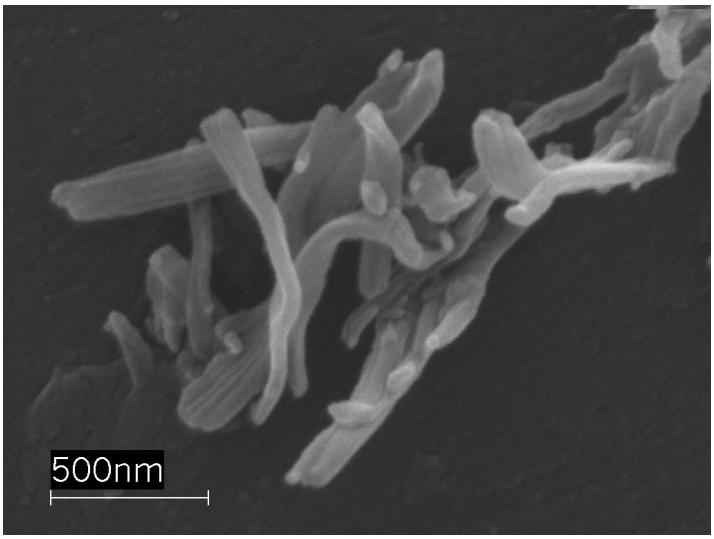

Figure 7.4 CoO_x da $Co(NO_3)_2$

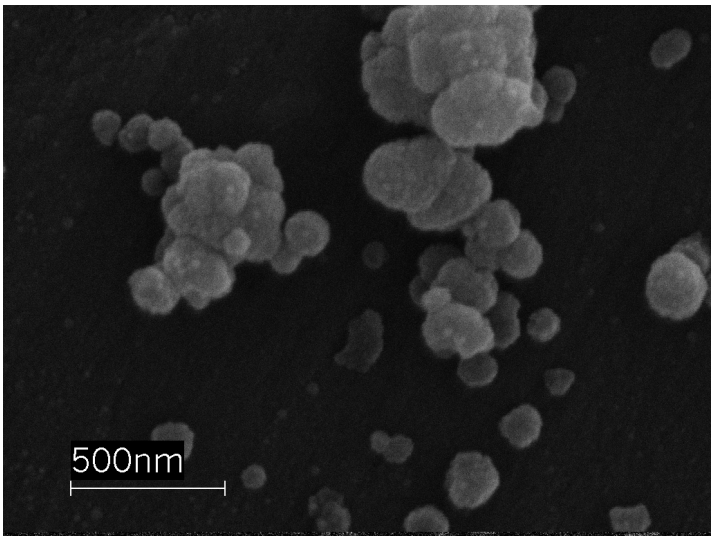

Figure 7.5 Fe_2O_3

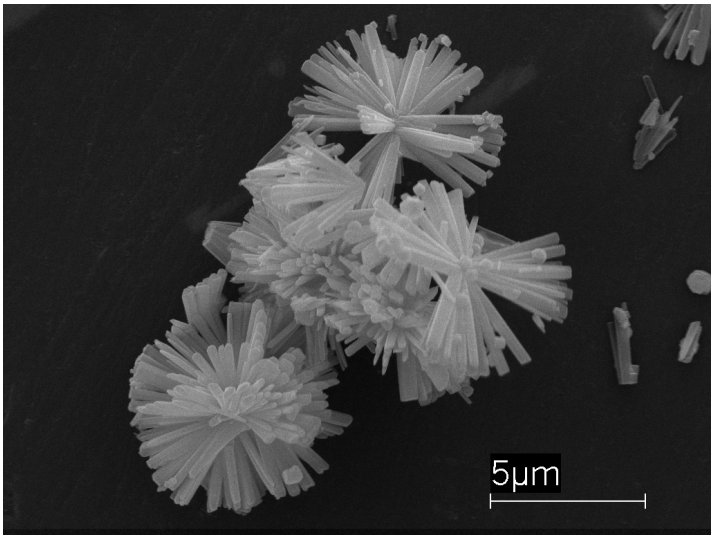

Figure 7.6 CuO_x da $Cu(NO_3)_2$

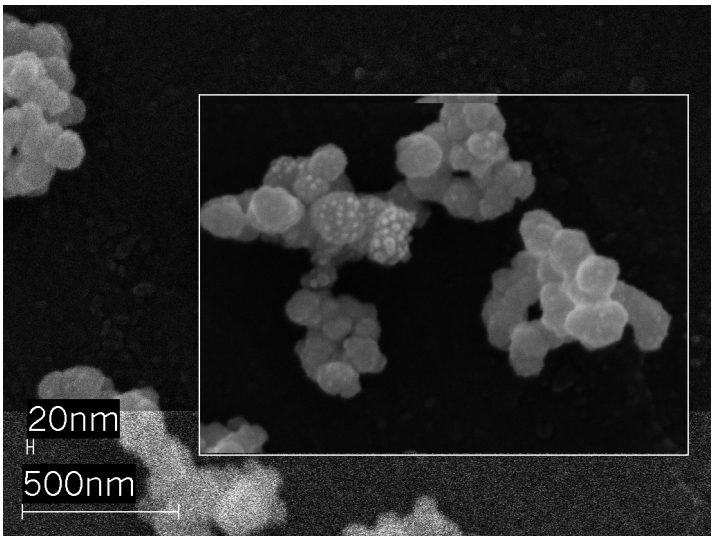

Figure 7.7 PtO_x da H_2PtCl_6

7.4 Conclusions

- The feasibility of the non-aqueous method was firstly assessed for RuO_2 nanoparticles. $RuCl_3$ was the precursor and benzyl alcohol was used as solvent and reactant. Various experimental setups and conditions were evaluated. The synthesis of RuO_2 nanoparticles was performed both in open and close vessels with good yields. The reaction was complete in 24 hours.
- The synthesis was also performed with microwave irradiation. This enabled the reaction to be completed in less than 5 minutes. Preliminary electrochemical experiments (cyclic voltammetry, cathodic polarization) were performed on these electrodes. Cyclic voltammetry showed the typical features of polycrystalline RuO_2.
- Powders of RuO_2, IrO_2, Rh_2O_3, Re_2O_3, Co_3O_4, $CuO_x(OH)_y$, PtO_x were also produced. In some cases, separation of the product from the reaction mixture was a challenging task, especially for IrO_2. SEM images showed that the morphology of nanoparticles varies as different precursors (nitrate, chloride) of the same cation are used.

7.5 References

[1] L.N. Lewis, Chemical Reviews 93 (1993) 2693.

[2] V. Kesavan, P.S. Sivanand, S. Chandrasekaran, Y. Koltypin, A. Gedankin, Angew. Chem. Int. Ed. 38 (1999) 3521.

[3] P. Mulvaney, Langmuir 12 (1996) 788.

[4] M.M. Alvarez, J.T. Khoury, T.G. Schaaff, M.N. Shafigullin, I. Vezmar, R.L. Whetten, J. Phys. Chem. B 101 (1997) 3706.

[5] A.P. Alivisatos, J. Phys. Chem. 100 (1996) 13223.

[6] R.F. Khairutdinov, Colloid Journal 59 (1997) 535.

[7] S. Duron, R. Rivera-Noriega, P. Nkeng, G. Poillerat, O. Solorza-Feria, Journal of Electroanalytical Chemistry 566 (2004) 281.

[8] M.-C. Tsai, T.-K. Yeh, C.-H. Tsai, Electrochemistry Communications 8 (2006) 1445.

[9] K. Biswas, C.N.R. Rao, Journal of Nanoscience and Nanotechnology 7 (2007) 1969-1974.

[10] I. Birss, H. Andreas, I. Serebrennikova, H. Elzanowska, Electrochem. and Solid State Letters 2 (1999) 326.

[11] A. Marshall, R.G. Haverkamp, Electrochimica Acta 55 (2010) 1978-1984.

[12] B.L. Cushing, V.L. Kolesnichenko, C.J. O'Connor, Chemical Reviews 104 (2004) 3893-946.

[13] J. Livage, M. Henry, C. Sanchez, Prog. Solid State Chem. 18 (1988) 259-341.

[14] M. Niederberger, G. Garnweitner, Chem. Eur. J. 12 (2006) 7282-302.

[15] M. Niederberger, Accounts of Chemical Research 40 (2007) 793-800.

[16] N. Pinna, M. Niederberger, Angewandte Chemie (International Ed. In English) 47 (2008) 5292-304.

[17] H. Wang, J.-Z. Xu, J.-J. Zhu, H.-Y. Chen, J. Cryst. Growth 244 (2002) 88-94.

[18] L.L. Hench, J.K. West, Chemical Reviews 90 (1990) 33-72.

[19] I. Bilecka, I. Djerdj, M. Niederberger, Chem. Comm. (2008) 886-888.

Chapter 8. Final remarks

A main target in electrocatalysis is to explain the different activity of materials and to correlate physico-chemical properties with electrochemical performance. In order to characterize the electrode materials, electrochemical investigations have to be supported by accurate physico-chemical characterization of the surface.

In this thesis, various electrocatalytic materials were prepared and evaluated towards H_2 evolution and O_2 evolution reaction. Studies on RuO_2 modified by laser irradiation and ion bombardment resulted in a publication on an International Journal. Results on Ir and Co mixed oxides and Ru and Ni mixed oxides were presented in International meetings. Two new synthetic routes for the synthesis of nanostructured transition metal oxides were implemented.

Some relevant issues in designing and producing electrodes suitable for HER and OER have been investigated and highlighted. In particular, were analyzed: i) preparation and production of the catalyst; ii) catalyst morphology; iii) intrinsic activity of catalysts.

The results showed that the nature of the electrodic material strongly influences the process efficiency. Various aspects of electrochemical behaviour must be investigated in order to characterize and understand the electrochemical processes. Active surface area, specific activity, electronic resistance and particle/layer structure are all important properties which need to be optimized to achieve high efficiency and performance. Moreover, in the search for electrode materials for industrial applications, a compromise between electrocatalytic activity, long-term stability and cost must be achieved.

Materials prepared by thermal decomposition of suitable precursors directly on a substrate exhibit a micro-porous morphology, constituted by agglomerates of smaller particles with nanometric dimensions. This structure results in an extended surface area, characterized by a great number of lattice defects, which are sought to be the active sites where electrochemical reactions preferentially occur. The fresh oxide films are anhydrous but the outer layers undergo hydration at the early stage of the reaction.

Ir and Co mixed oxide exhibit better electrocatalytic performance than pure IrO_2. Mixing IrO_2 with less active Co_3O_4 modifies the properties of IrO_2. The surface area is greatly increased and the electrode material appears to be stabilized.

The synthesis of nanoparticles allows for an enhanced area/volume ratio. In this respect, Ru and Ni mixed oxides were synthesized by a non-aqueuos sol-gel method and by thermal decomposition. Results towards the reaction of H_2 evolution suggest that electrochemical behaviour is affected by the method of preparation and by the substrate. As a rule, the wetting of RuO_2 both in alkaline and acidic media is the origin of the increase in surface area. In acidic environment, the dissolution of NiO_x modifies the surface and new active sites become exposed to the solution. Furthermore, materials are activated after an initial cathodic polarization and the mechanism of H_2 evolution is modified.

As concern materials for O_2 evolution reaction, RuO_2 surfaces were modified by physical treatment. The effect of laser irradiation and atom bombardment is to increase the surface area and the apparent activity. The enhancement is higher for atom bombardment, which is presumed to stimulate the exposition of particularly active sites as a consequence of the fracture of RuO_2 crystallites.

In the last part of this thesis a novel non-aqueous synthesis was applied to produce nanoparticles of transition metal oxides for application in electrocatalytic water splitting. The feasibility of the method was firstly assessed for RuO_2. Powders of RuO_2, IrO_2, Rh_2O_3, Re_2O_3, Co_3O_4, $CuO_x(OH)_y$ were produced. Nevertheless the synthesis of transition metal oxides applied to electrocatalytic water splitting (e.g., IrO_2 and RuO_2) is missing in the literature. The microwave processing of nanoparticles results in rapid heating of the reaction mixtures. As a consequence, the precipitation of particles tends to be rapid and nearly simultaneous. This leads to very small particle sizes and narrow size distributions within the products. The method offers the additional benefit of requiring very short reaction times.

Particular properties of metal nanoparticles and their large surface area suggested the application in electrocatalysis and electroanalysis.

LIST OF SYMBOLS

b	Tafel slope	mV dec^{-1}
E	Electrode potential	V
E_{rev}	Reversible potential	V
F	Faraday's constant	C mol^{-1}
I	Current intensity	A
j	Current density	A cm^{-2}
j_0	Exchange current density	A cm^{-2}
n	Electron number	
Q	Voltammetric charge	C
q^*	Voltammetric charge density	C cm^{-2}
R	Resistance	Ω
R	Gas constant	J mol^{-1} K^{-1}

β_i	Reaction order
η	Overpotential
λ	Wavelength
θ	Fractional coverage of adsorbed species
α	Transfer coefficient

ABBREVIATIONS

CV	Cyclic voltammetry
DSA©	Dimensionally Stable Anodes
EDX	Energy dipersive X-ray analysis
HER	Hydrogen evolution reaction
OCP	Open circuit potential
OER	Oxygen evolution reaction
PEM	Proton exchange membrane
pzc	Point of zero charge
rds	Rate determining step
RHE	Reference hydrogen electrode
SCE	Saturated calomel electrode
SEM	Scanning electron microscope
TGA	Thermal gravimetric analysis
XRD	X-ray diffraction
XPS	X-ray photoelectronic spectroscopy